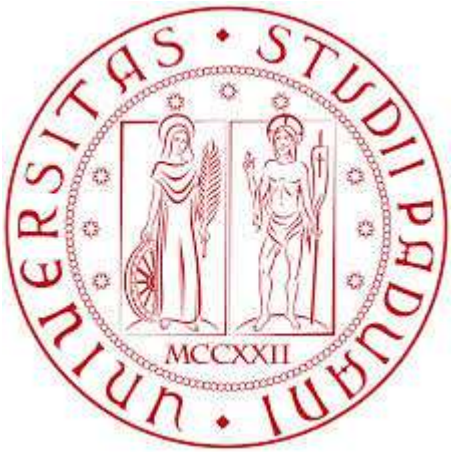

UNIVERSITA' DEGLI STUDI DI PADOVA

DIPARTIMENTO DI INGEGNERIA INDUSTRIALE

CORSO DI LAUREA IN INGEGNERIA DEI MATERIALI

Tesi di laurea

LATE FATIGUE DAMAGE DEVELOPMENT IN A 3D WOVEN E-GLASS/EPOXY COMPOSITE

Laureando : Luca Baiocchi

Relatore: Chiar.mo Prof. Marino Quaresimin

Correlatore: Prof. Stephen Louis Ogin

Anno Accademico 2012-2013

ACKNOWLEDGMENTS

Firstly I would like to thank my head supervisors Marino Quaresimin and Steve Ogin: their effort gave me the opportunity to be involved in this project and spend a wonderful time at the University of Surrey as an exchange student.

In particular way I would like to thank Steve Ogin for his kindness, his encouragement, his patience, his scientific support and for the enthusiasm that he injected into me every time we met.

I want to thank my colleague Tobias Capell for his constant help. Toby helped me from the very first to the last day of my experience. With his patience he taught me a lot things about how to approach to this experimental work. We spent a lot of nice time together, not only in the lab but also travelling around England by motorbike and by train.

Furthermore I would like to thank Pete Haynes and Chris Burt for the technical support and for all the funny stories they told me.

I would like to thank all my friends that I met at the University of Surrey, specially friends of the “Surrey summer village” and my Italian companions Luca Zanette and Elena Barbera.

I would like to thank my girlfriend Giulia for her constant support and love even if we have been distant for six months.

Last but not least I would to thank my parents Luciano and Maria Grazia for their love and support throughout my whole life. Without out them I could not get to where I am now, in the position of writing my own Master dissertation.

CONTENT

1.Abstract

In this work, the development of damage leading to the fatigue failure of a non-crimp 3D orthogonal woven composite has been investigated. A transparent composite was fabricated using a non-crimp single ply 3D orthogonal reinforcement (provided by 3TEX Inc, USA) and a matrix of Shell Epikote 828 epoxy resin. The 3D fabric consisted of two layers of warp tows and three layers of weft tows, interlaced with z-tows. Specimens were fatigue tested and damage development was monitored using mechanical test data (hysteresis loops of stress/strain) *in situ*, visual observations of damage, sectioning/optical microscopy and X-ray micro computed tomography (X-ray μCT).

The specimens tested had dimensions 200 mm in length, 2.2 mm thick and 8 mm in width; the width was sufficient to encompass at least one complete unit cell of the fabric, and a long gauge length extensometer was used to monitor the mechanical property changes. Damage development has been followed during fatigue tests by measuring the stiffness reduction with cycle number, and also the area within the stress/strain hysteresis loops. In order to investigate the development of damage, some samples were taken to failure, while for other specimens the tests were interrupted prior to failure.

This work will focus on damage within the later stages of the fatigue life of a specimen, but it is worthwhile indicating the various stages in the lifetime of a specimen in order to provide the context. In general, the results suggest that damage develops in four stages. The first stage, where the stiffness of the specimens reduces rapidly and there is a

relatively large hysteresis loop area, is believed to be related to the development of matrix cracking damage within the specimens, and possibly some delamination and fibre fracture. In the second stage, a very low rate of stiffness reduction and narrow hysteresis loops are probably related to the extension of the matrix cracking and the development of other damage, but at a much reduced rate. The third stage is characterized by a significant increase in the rate of stiffness reduction of the specimen and an increase in the hysteresis loop area. The fourth stage, which is quite short, sees a very rapid stiffness reduction, accompanied by a very rapid increase in hysteresis loop area, culminating in specimen fracture.

The results within this work relate to the final two stages. Of particular interest is the development of tow fractures in specific locations within the complex fibre architecture, identified by a combination of X-ray μCT and sectioning/optical microscopy. A hypothesis relating to the development of this damage will be provided within the paper, supported by experimental evidence. The paper will also present evidence of various types of damage development in the 3D composites (macro and micro-delamination, extensive warp/weft delaminations, tow fractures) and will relate these results to previous work by a number of authors (e.g. Bogdanovich and Mohamed, 2009; Carvelli et al, 2010; Lomov et al, 2009**;** Mouritz, 2008).

2. Literature review

2.1. Introduction

This chapter presents the background for the current work. It is divided into two parts. In the first part, a general introduction is given to textile composite materials, including 2D and 3D reinforcement. In the second part, the focus is on the behavior of 3D composite materials which have been the topic of this work.

2.2. Introduction to textile composites materials

Textile composites are composite materials which are reinforced with continuous fibers: these fibers are interlaced in order to form yarns then weaved with the purpose to create a continuous woven cloth. Usually the matrix is polymeric and many types of fibers may be used: fibers can vary from carbon to glass to metal but usually glass and carbon fibers are the most commonly used in structural applications. Fabrics are characterized in terms of weave, areal density and thickness under specific pressure conditions. The tows are characterized by a unit called tex, which represents weight (in grams) per a unit length of 1 km. [1],[2].

Most of the woven cloths consist of tows that are woven in two in-plane perpendicular directions (x and y directions in the Cartesian system), termed as warp and weft directions. Furthermore the number of warp and weft tows per areal unit is termed as ends and picks, respectively. Depending on the textile structure (termed also as weave style), ends or picks could be more than the other one, leading to a cloth with a non-uniform distribution of fibres and consequently to a composite that behaves more like a unidirectional composite

with greater longitudinal strength compared with the transverse strength. In the case of the same number of picks and ends the composite is expected to have the same mechanical properties in both longitudinal and transverse direction. Some cloths could also be made of tows of different materials (e.g. glass and aramid fibers) and such a cloth is termed as hybrid cloth and the composite as hybrid composite. [2],[3],[4]

As mentioned above the cloth could be woven in various textile structures leading to composites with various properties and volume fractions, depending on the selected textile structure. The most commonly used 2D structures are plain weave, twill weave, satin weave, 3-D weaves include layer-to-layer interlock, angle interlock and orthogonal; these are discussed in more detail in section 2.3. [1],[4]

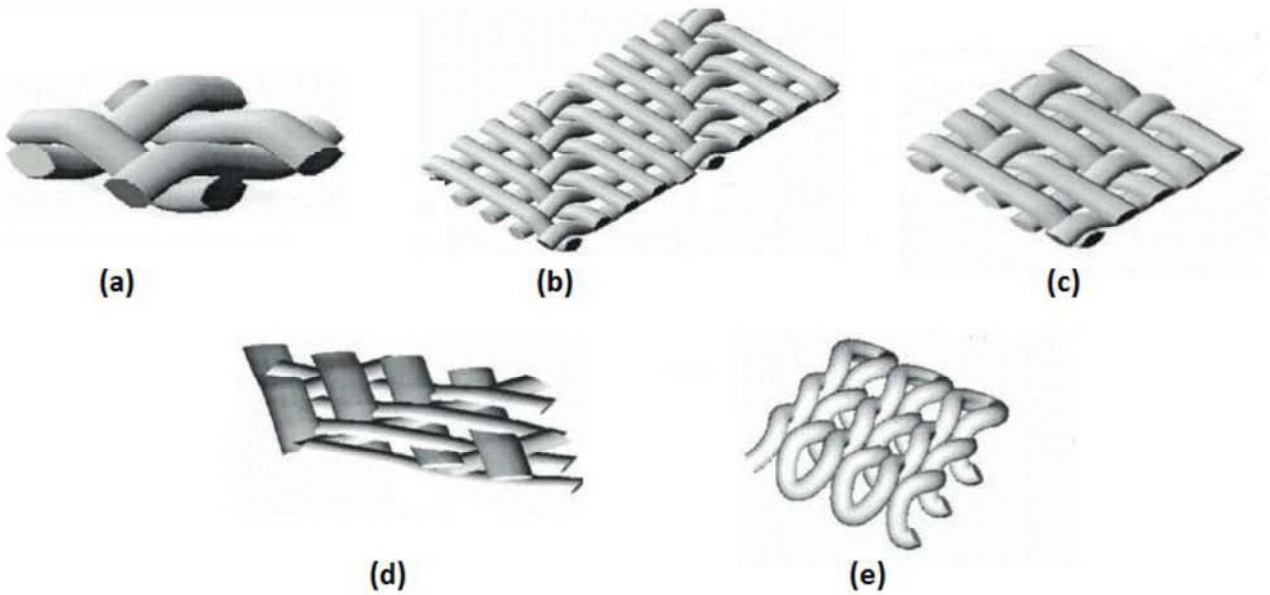

Fig. 2.1: Schematics of various textile structures. (a) plain weave, (b) twill weave, (c) knitted weave (c) braided weave, (d) and (e) 2-D braied weave. [1]

The composites used within this work are glass-reinforced epoxy resin, so it is appropriate here to introduce glass fibers and epoxy resins.

Glass fibers are extruded from a hot melt of glass in fine fibers of diameter of 3 to 20 μm, though the diameter is typically 15 μm for the fiber-reinforced composites. Their good wettability in epoxy matrices and their good mechanical properties alongside their low-cost properties have made them one of the most common reinforcing phases for composites with polymeric matrices. Nevertheless they have significantly poor abrasion resistance. This problem is dealt by the matrix since when the fibers are impregnated by the matrix they are no longer exposed to the environment, but they are surrounded by the matrix that protects them. The mechanical properties of glass fibers at room temperature in terms of Young's modulus, ultimate tensile strength, tensile strain to failure, specific modulus and specific strength are given in table 2.1.

Material	Tensile Modulus (GPa)	Tensile Strength (MPa)	Tensile strain to failure (%)	Specific Modulus (E/ρ)	Specific Strength (σ/ρ)
E-glass	72	345	4,80 %	29	1,36
S-glass	87	430	5	35	1,73

Table 2.1: Mechanical properties of glass fibers

Epoxy matrices are widely used in fibrous and textile composites. Their popularity is a result of their good mechanical properties and relative low cost. Epoxy matrices are thermoset polymers that have low viscosity in room temperatures when there are uncured, that make them easy to process during the manufacture of the composite. Such

matrices are mainly used in glass fibre and carbon fibre reinforced composites due to their good wettabilty and fibre impregnation when they are combined with such fibres. [5],[6],[7]

Such matrices are considered to have good mechanical properties and retain their structural integrity under relative high temperatures and moist environments. Nevertheless, their lack of molecular movement is responsible for their brittle behaviour. The mechanical properties in terms of Young's modulus, ultimate tensile strength, tensile strain to failure and compressive strength of the epoxy matrices in room temperatures are given in table 2.2.[5],[6]

Material	Tensile modulus(GPa)	Tensile Strenght (MPa)	Tensile strain to failure	Compressive Strenght (MPa)
Epoxy	2-6	35-130	1-8,5 %	100-200

Table 2.2 Mechanical properties of epoxy resin

2.3. 3D reinforced composites

2.3.1. Introduction

In the following sections, 3D reinforcements for composites are introduced before focusing on the structure and properties of 3D orthogonal weave composites, which have been used in this study.

2.3.2. Approaches for 3D reinforcement of composite materials

The main problem associated with the 2-D woven reinforced composites in terms of structural integrity during loading is delamination. In composite material manufacturing layers of fibers or clothes are added with a precise sequence one on top of each other with the purpose to obtain applicable in-plane mechanical properties as strength and stiffness. This layup leads to a combination of laminae which is called laminate composite. Delamination is the damage situation where the laminae (the layers of fibres or cloth) are peel apart as a result of tensile loading stresses and shear stresses: delamination is the result of interlaminar cracks that are propagating easily through the weak layers of matrix which form the interface between two laminae. For these reasons low through-thickness strength and fracture toughness are frequently connected with poor delamination resistance and impact damage tolerance.

A through-thickness reinforcing phase in the z direction could hold the laminae together leading to enhanced delamination resistance of the composite material. [2],[7],[8] The concept of the 3-D reinforcement is not very recent and efforts have been introduced since the first delaminations were observed. Several methods have been developed to increase the delamination toughness that include well-established methods such as rubber toughening of the matrix and fibre adhesion treatment as well as contemporary methods such as nanoparticle toughening of the matrix and carbon nanotube treatment of the fibres.

Another important method is the reinforcement of the composite in the through-thickness direction using fibrous yarns, rods or pins, which collectively is called z-reinforcement. The

most common techniques are stitching, z-pinning and 3D-weaving. The first attempts were recorded in the early 1980's [2] with the stitching procedure. During the stitching process , pre-pregs are stitched together with reinforcing fibers using a needle. By stitching, the delamination resistance has improved but on the other hand it affects negatively the in-plane properties as the tensile strength and the Young's modulus of the stitched composite are reduced. The reduction of the in-plane mechanical properties is the result of the stitching process since a sharp and relatively large diameter needle is piercing the pre-preg or cloth and introduces defects and distortions in the original texture and damage or even fibre fracture of the in-plane fibres. [2],[11],[12]. Non-crimp fabrics are not stitched together with a reinforcing yarn, however through-thickness stitching with reinforcing fibres is also used.

Another method to improve the through-thickness strength is the z-pinning: this technique uses a rod or fibers which is introduced in the z-direction of the material during the curing of the matrix. At this step of the process the viscosity of the matrix is low and that allows to introduce the z-reinforcement without bringing stresses or defects. Nevertheless, the structure of the in-plane fibres or cloth is still distorted and it leads to a decrease of the in-plane tensile mechanical properties. [2],[14].

Although there have been efforts to reduce the distortion by employing an ultrasonic vibrated needle head, microscopic studies have shown that the pins are still distorting the original fiber architecture and are responsible for fiber breakage and create resin rich areas in the tips of the z-pins. This observation could explain the reduced in-plane mechanical properties in comparison with the expected properties. Nevertheless it has to be noticed that z-pinning enhance the delamination resistance of a composite. Although stitching and z-pinning are different methods they do share the distortion of the fiber structure during their introduction leading to the abovementioned results.

3D weaving produces 3-D textile structures containing tows that are woven together in all of the three dimensions. The tows in the third dimension (z-direction) are holding the tows of the other two in-plane dimensions together. These extra tows in the z-direction that are termed as z-yarns or z-tows enable us to weave thick cloths, with the z-tows holding together layers of warp and weft tows.

3-D woven fabrics therefore contain fiber along the z direction and can be used to form thick cloths. There are three main categories of 3-D weaves: the 3-D layer-to-layer, angle interlock and the 3-D orthogonal non-crimp weave.

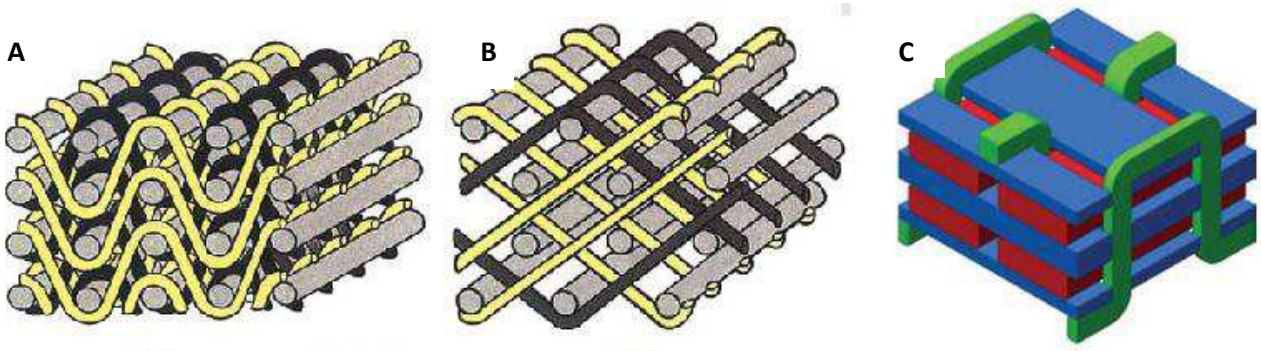

Fig. 2.2: Schematics of (A) 3-D layer-to-layer interlock, (B) 3-D angle interlock and (C) 3-D orthogonal non-crimp weaves. [9]

The different colours of figures (a) and (b) represent the three different weaving directions. The simultaneous weaving of all tows does not introduce deformations of the fiber architecture as was observed in the z-pinning and stitching, and therefore one could avoid the degradation in the mechanical in-plane properties. [9],[16]

A schematic of a 3-D orthogonal non-crimp weave is illustrated in figure 2.2 (C), where the warp tows are illustrated as the red tows, the weft as the blue tows and the z-tows as the green tows. Therefore, each color represents a different weaving direction.

In the following section, the structure and properties of 3D orthogonally woven composites is discussed, since these composites have been used in this work.

2.3.3. Structure and properties of 3D woven composites

There has been much research done about the mechanical properties of a composite reinforced with 3D woven reinforcement. The main goal of much research has been a direct comparison of the 3-D woven composites with conventional 2-D woven composites.

Brandt et al. (1996) have studied the mechanical performance of composites reinforced with equivalent 2-D plain weaves, 3-D orthogonal weaves and 3-D angle interlock weaves. The cloths were weaved with carbon fibers and were impregnated in epoxy matrix. Their study involved tensile, compressive and drop-weight impact tests. The equivalency of the cloths used was based on the number of the layers of the 2-D in-plane weaves that each composite consisted. The results of this study are given in table 2.3

	2-D Weave		3-D Weave Interlock		3-D Orthogonal	
	Warp	**Weft**	**Warp**	**Weft**	**Warp**	**Weft**
Tensile Strength (MPa)	615	620	410	416	541	494
Tensile Modulus (GPa)	65	58	48	51	44	59
Compr. Strength (MPa)	506	506	285	373	574	501
Energy Absorption (J)	30		46		81	

Table 2.3 : Comparison of mechanical properties of different textile composites

As we can observe from table 2.1, 3-D orthogonal woven composites seem to have lower tensile strength and elastic modulus compared with the 2-D woven, but higher tensile strength and elastic modulus compared with the 2-D interlock woven composites.

These results are in agreement with the results of experimental work of Lomov et al. (2009) for the in-plane tensile properties of 3-D orthogonal woven composites. They studied glass fibre 3-D woven epoxy reinforced composites and equivalent 2-D plain woven composites. Their results are given in table 2.2, where we can observe the values of the Young's modulus, the ultimate tensile strength, Poisson's ratio and strain to failure.

Properties	2D-24	3D-96		3D-78	
	Warp	Warp	Weft	Warp	Weft
E(GPa)	26,0 ± 1,5	24,3 ± 1,2	25,1 ± 23	23,0 ± 2,5	24,4 ± 1,6
Strength(MPa)	413 ± 4	429 ± 34	486 ± 5	423 ± 29	427 ± 8
Ultimate Strain %	2,38 ± 0,02	2,74 ± 0,29	3,33 ± 0,27	2,96 ± 0,51	3,14 ± 0,44

Table 2.4 : Mechanical properties of 2D and 3D woven fabrics

It could also be observed in this case that the 2-D woven composites have greater tensile mechanical properties, as the values of ultimate tensile strength and Young's modulus are higher than the 3-D woven composites. Nevertheless, 3-D woven composites seem to have higher strain to failure limits under in-plane loading.

Rudov, Clark and Mouritz (2007) investigated the tensile fatigue properties of a specific type of orthogonal woven composite that contained different volume content of through-thickness reinforcing fibers. Using a computer controlled Jacquard loom they interlocked the fabric with 68 tex, 204 tex or 408 tex yarns as a z-reinforcement so the 3D woven composites contained z-binders content of either 0.3, 0.5 or 1.1 % by volume.

They also examined the microstructure of the materials prior to fatigue testing using optical and scanning electron microscopy. They characterized the structure of the fabric they created and they detected defects as Z-binder waviness and fractures of z-binders. Some of the distinguishing features of 3D woven composites were as follows:

1) The z-binders yarns did not exactly follow the square-shaped orthogonal profile shown in the schematic above figure 2.2.C. During weaving it is necessary to apply a slight tensile load on the z-binder yarns to ensure they are taut when woven into the fabric. The load caused the z-binders to follow a sinusoidal shaped orthogonal

profile (see figure 2.3). This change to the z-binder profile often occurs in 3D woven composites with an orthogonal structure and it's difficult to avoid because z-binders must remain taut during weaving.

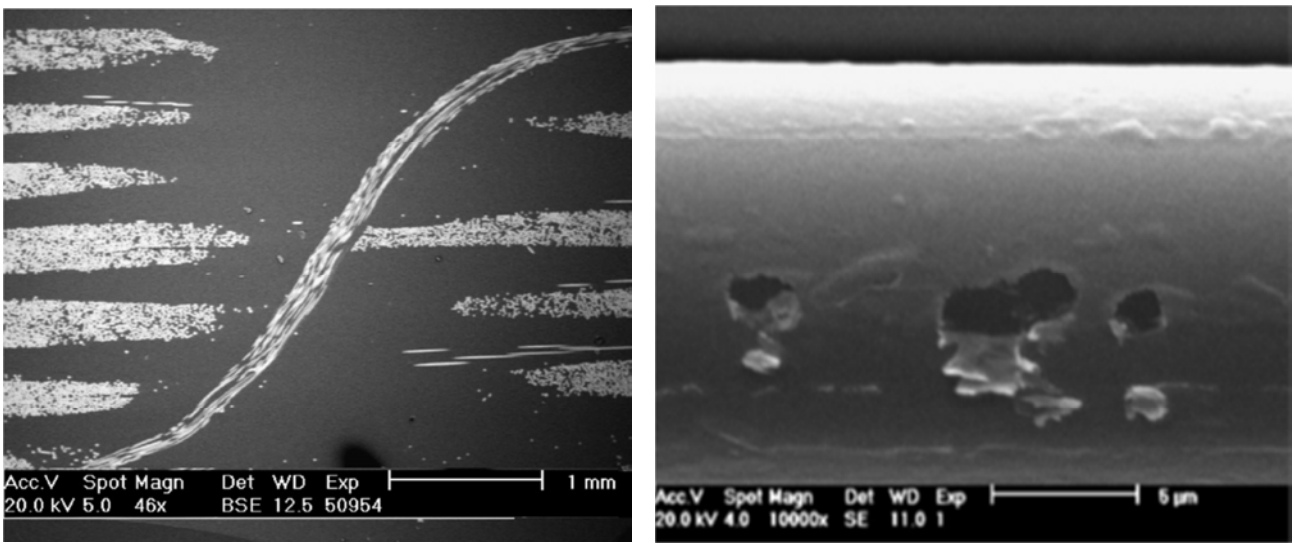

Fig.2.3: Sinusoidal shaped profile of a z-yarn (A); Abrasion after weaving on the z-binders (B)[15]

2) The z-binders suffer considerable fibre damage when woven into the fabric. Mouritz et al. examined the damage to z-binders during the weaving of the 3D fibreglass fabrics used in the composite specimens. They measured a small reduction to the Young's modulus (5%) and a large drop to the tensile strength (50%) of the z-binders due to the weaving process. The loss in strength is attributed to the formation of defects on the surface of the glass fibres that make-up the z-binders. Micro-cracks also develop from abrasion of the z-binders as they rub and slide against the loom machinery during weaving. Fig. 2.3 B shows abrasion marks on a glass fibre caused by weaving. Mouritz et al. found that a small percentage (5%) of fibres within the z-

binder yarns break when woven into the fabric, and a much larger percentage contain cracks which are sufficiently large to reduce the tensile strength.

3) Fibre crimp occurs where the z-binders pass over the weft yarns at the surfaces. The z-binders press the weft yarns into the fabric which then causes local crimping of the warp yarns. Crimping to the warp and weft yarns cannot be avoided because a tension load must be applied to the z-binders during weaving to ensure they are taut within the fabric.
4) Polymer-rich regions were formed along each row of the z-binders in the warp direction. The warp yarns are pushed sideways during the weaving process to make space for the z-binders, and this forms a gap between neighbouring yarns which is then filled with polymer during resin infusion. This results in the formation of a polymer- rich channel along each z-binder row in the warp direction.
5) Voids were found in the polymer-rich regions in the 3D woven composites, particularly need the z-binders. The average porosity content was about 1% by volume, but most of the voids are located in the polymer matrix near the z-binders. The porosity occurs because the resin permeability of the 3D woven fabric is highly anisotropic, with different flow rates in the warp, weft and through-thickness directions.

The fatigue properties were investigated and fatigue life (S–N) curves for the woven composites are shown in fig 2.4. It was possible to observe general trends in fatigue behaviour between the different materials containing different volume fraction of z-yarns. The data shows that the fatigue life decreases with increasing z-binder content.

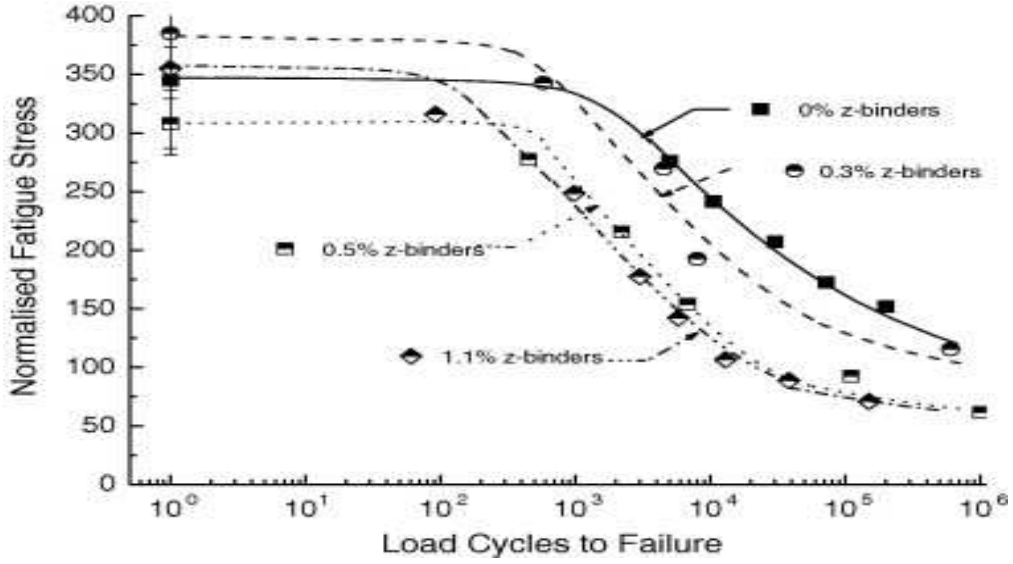

Fig. 2.4 : S-N curve for different z-binders content [15]

In their study, mouritz et al also examined the residual fatigue strength measuring it after 10^6 load cycles. In fig 2.5 is shown that the residual fatigue strength decreases with the percentage content of z-binders. It means that increasing the content of z-reinforcement affects the performance of the specific type of the 3D woven composite material they tested.

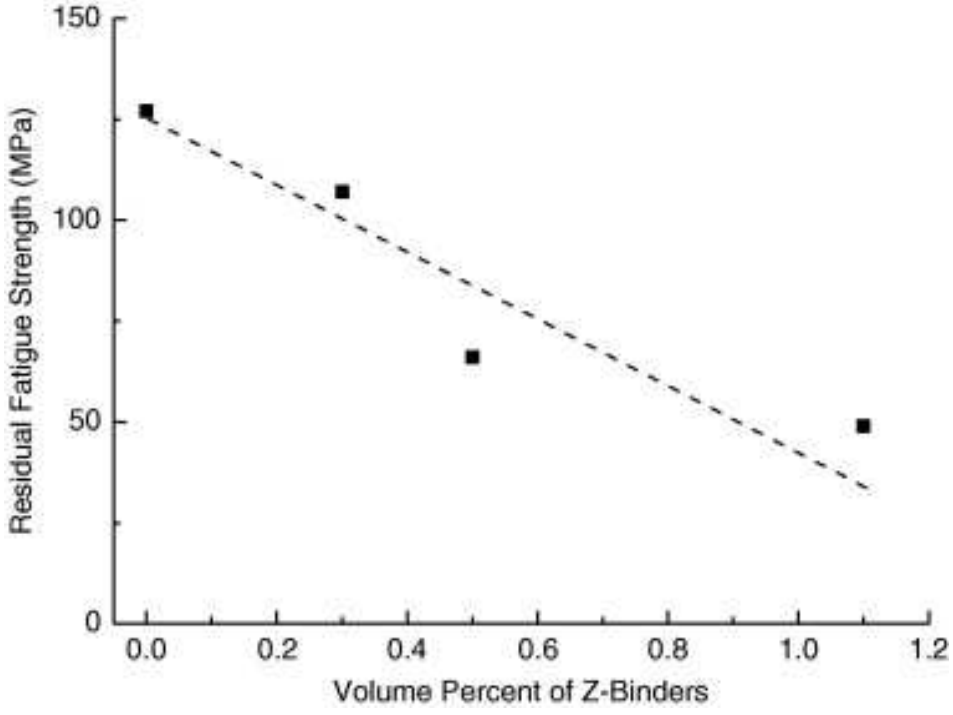

Fig. 2.5 : Residual fatigue strength after 10^6 load cycles [15]

The reduction to the fatigue properties of the 3D woven composites is attributed to pre-existing defects and damage caused by the z-binders.

Carvelli et al. (2010) investigated the fatigue behavior of a single-ply non-crimp 3D orthogonal weave E-glass composite and compared the performance with an equivalent composite laminate reinforced with four plies of standard plain weave fabric. They tested the two laminates at different stress levels comparing the fatigue performances for every stress level. Their experimental study showed that the fatigue performance of a plain weave composite was significantly worse than the performance of the 3D composite tested in weft direction for all the studied stress levels with the 3D composite having significantly longer fatigue life for all the applied stress levels. The 3D composite tested in the warp direction had a slightly longer fatigue life than the plain weave composite for the low-cycle fatigue stress range (≥ 350 MPa), but a significantly longer life for the high-cycle fatigue stress range (≤ 150 MPa).

Carvelli et al. suggested a hypothesis to explain the difference in performance of the 3D composite between weft and warp loading direction. Under warp directional loading the difference could be attributed to the structure of 3D woven preform: when the load is applied in warp direction (which is the same direction of the z-tows) both the warp and the z-tows are loaded in tension. In this conditions there is a stress concentration induced by the z-tows in its crossover area with the weft due to different mechanical properties between the weft tow and the z-yarn that loops over it: the difference of orientation between weft tow and z-yarn induces different Young's modulus which create different strains in the 0° and 90° direction. Another hypothesis suggests that under tensile loading

in warp direction the reduction of the sample width takes place due to Poison's effect and the result is a respective reduction of the distance between adjacent Z and warp yarns. These yarns could get in a contact and, due to both of them are exposed to cyclic tensile stress, their mutual friction effect may become sufficient to significantly reduce the overall fatigue life of the sample.

Kakaratsios (2010) performed an analysis of the architecture of the cloth "3-D 78" and an axis convention that follows the Cartesian convention was set, a convention that described the direction of warp, weft and z-tows. The convention set is the same used in this experimental procedure. The warp tows are illustrated as red, the weft tows as blue and the z-tows as green. Kakaratsios used the letters aa', bb' and cc' along with the arrows to represent the sectioning planes. He measured the dimension of the warp, weft and z-tow discovering some differences in values of the thickness of the yarns.

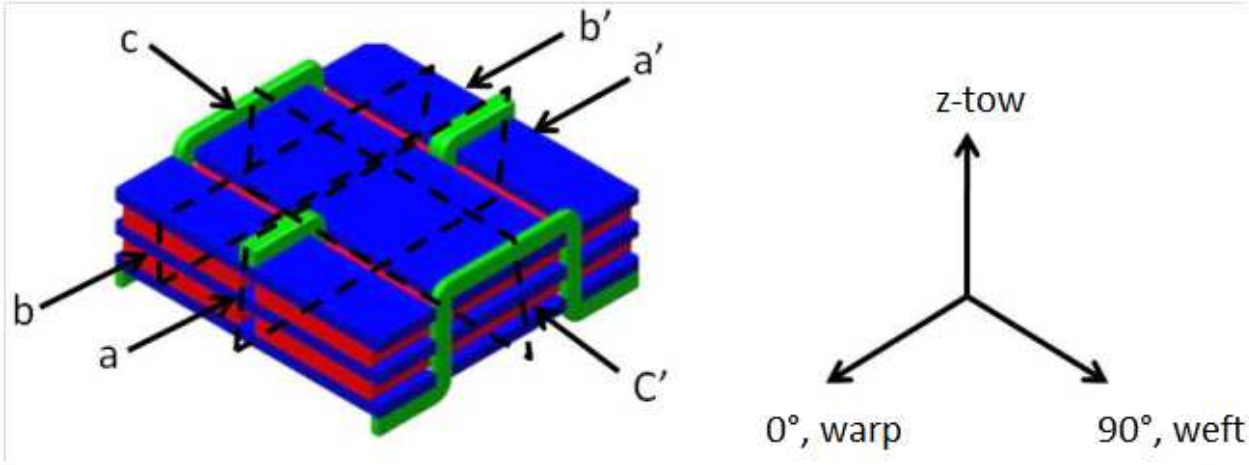

Fig. 2.6 : Axis convention and cross section planes of the 3-D specimens.[16]

The following figures are illustrating the aa' cross section plane view of figure 2.6. In figure 2.7 a panoramic view of the specimen could be observed and the fibre architecture in it.

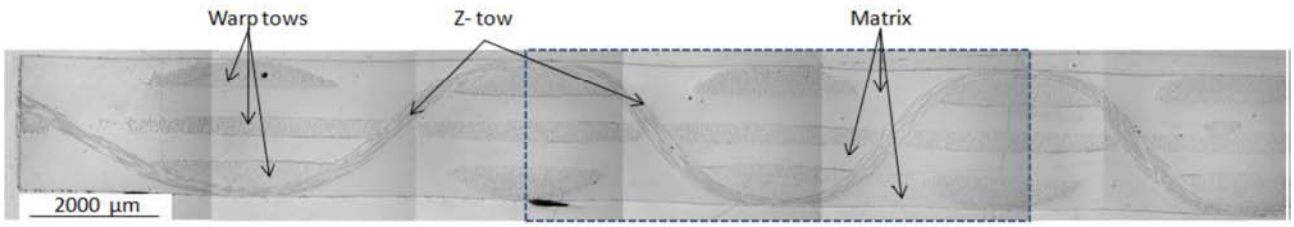

Fig. 2.7: Microscopic panoramic picture of the aa' cross section [16]

We can distinguish the weft tows and the z-tows that interlace them (note that Kakaratsios had mislabeled the weft tows as "warp tows"). It was observed that the actual architecture is not orthogonal, as in schematics of figure 2.6, but had an architecture closer to the interlock weave as illustrated in figure 2.1. It was close but it cannot be characterized as interlock because it had warp and weft tows interlaced by the z-tow that is characteristic of the 3-D orthogonal weave. The reason for the curvature (the wavy pattern of the z-tow) has been explained by Mouritz et al above.

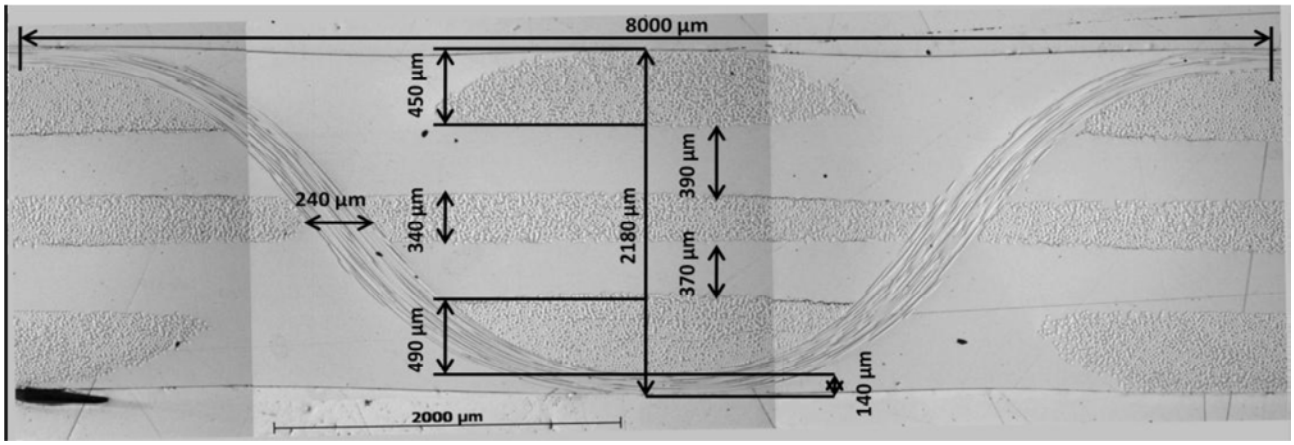

Fig. 2.7 : Magnification of figure 2.6 that illustrates the unit cell of the 3-D weave along with the thickness values of the warp and z- tows. [16]

Figure 2.7 shows a magnified view of the area in figure 2.6 that is enclosed by the blue dashed rectangular marking. Kakaratzios observed in this plane that there are many resin-

rich areas in-between the warp layers, in the areas that are not occupied by the z-tow. The measured peak to peak distance of the z-tow was approximately 8 mm.

Figures 2.9 and 2.10 show the bb' cross section plane of figure 2.6. In figure 2.9 the warp and the weft tows along with the matrix could be observed. In this plane of view the warp tows were visible while in the aa' plane view they weren't. It was observed that the resin rich areas are less than in the case of the aa' plane view.

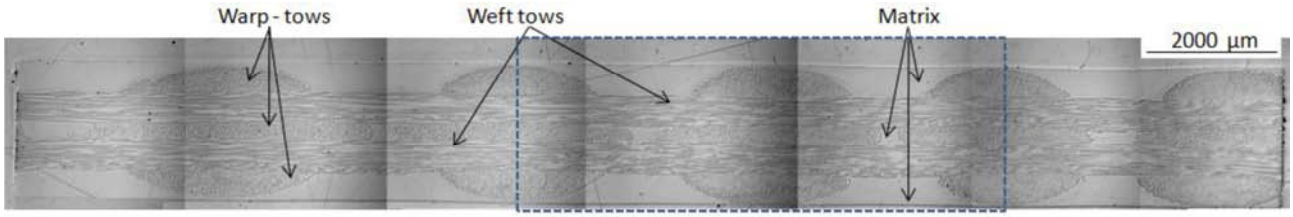

Fig.2.9: Microscopic panoramic picture of the bb' cross section [16]

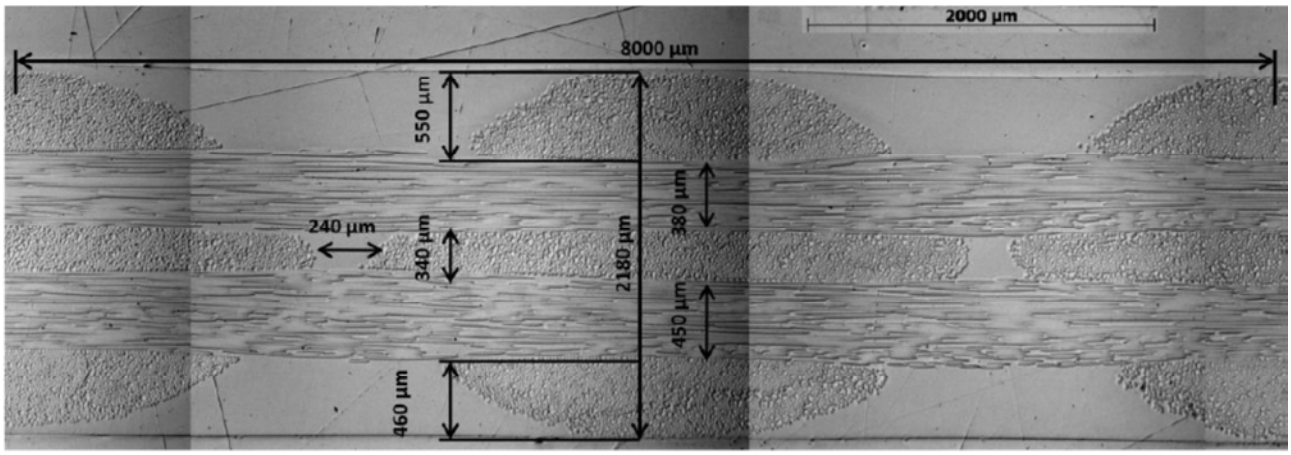

Fig. 2.10: Magnification of figure 4.5 that illustrates the unit cell of the 3-D weave along with the thickness values of the warp and z- tows. [16]

Figures 2.11 and 2.12 show the cc' cross section plane view of the schematic in figure 2.6, along the weft tows direction. In this plane of view the warp tows were visible. Also in this plane of view, the resin areas are smaller compared with the two abovementioned planes

of view. It was though observed that between the layers of the warp tows there were resin rich areas termed as *pockets*. The z-tows can also be seen in this view.

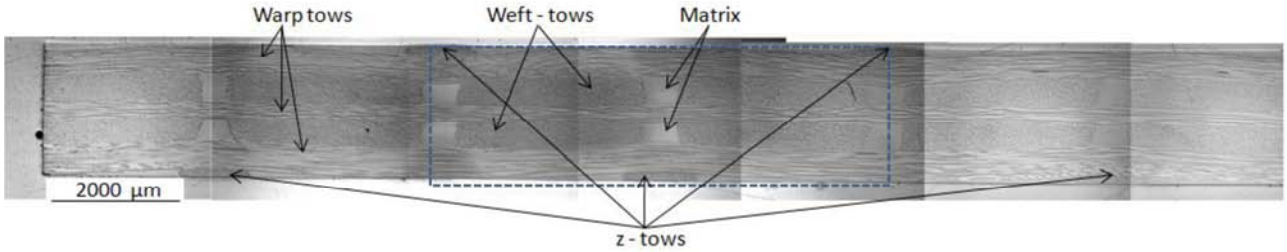

Fig. 2.11: Microscopic panoramic picture of the bb' cross section [16]

In figure 2.12 the unit cell of the 3-D orthogonal weave is illustrated in the aa' cross section plane view. This figure is the magnified area of figure 2.11 that is enclosed by the blue dashed rectangular marking.

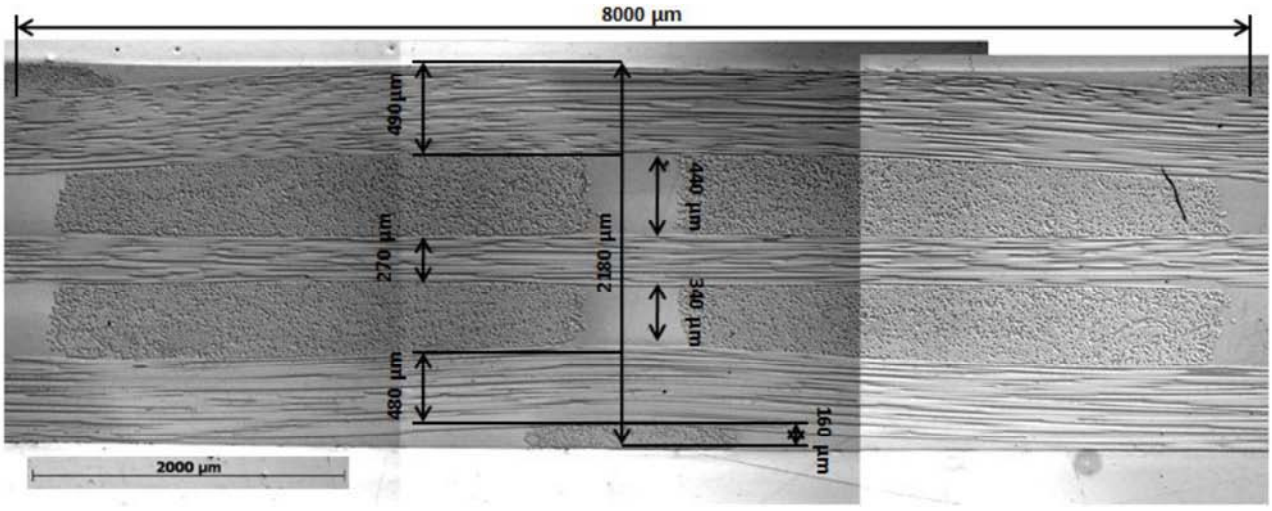

Fig.2.12: Magnification of figure 4.6 that illustrates the unit cell of the 3-D weave along with the thickness values of the warp, weft and z- tows. [16]

3. Experimental methods

3.1. Introduction

In this chapter is presented the experimental method used for the manufacture of the specimens, the test methods and the damage evaluation methods. The first section gives a brief description of the material used for the manufacturing process of the specimens, starting from the assembling of material constituents stage up to the final cutting of the glass/epoxy specimens and preparation for the fatigue tests.

3.2. Materials and specimen preparation

The 3-D fabric preform used was a 3WEAVE® woven cloth with an areal density of 2640 g·mm^{-2} (78 oz·yd-2), labeled as "3-D 78". The resin used was a Shell Epikote 828 (Bisphenol-A) epoxy resin with a Shell epicure nadic methyl anhydride (MNA) curing agent and Ancamine K61B accelerator. The structure of the 3-D orthogonal non-crimp weave consisted of three layers of weft tows interlaced by z-tows, and two layers of warp tows. All of the tows were formed from PPG Hybon 2022 E-glass fibres. The fabric was manufactured by 3TEX.

3.2.1. Specimen manufacture

3.2.1.1. Introduction

One goal of the specimen manufacture was to obtain a transparent laminate in order to observe the damage development during a fatigue loading. The first attempt of manufacturing the material was made with the VARTM technique, but it produced a poor

surface finish and transparency; it was then decided to move from the VARTM technique to a mild vacuum assisted resin impregnation method that guaranteed a good transparency and surface finishing. The preparation of the resin is the same for both manufacturing techniques. The resin was a three-part compound of epoxy, hardener and curing agent with a weight ratio of 100:60:3

3.2.1.2. The VARTM manufacturing method

For the VARTM method (Vacuum Assisted Resin Transfer Molding method), draws resin into a mold cavity. In addition, the VARTM mold is usually an open mold and the fiber preform is sealed between the open mold and a vacuum bag. The resin used was a Shell Epikote 828 (Bisphenol-A) epoxy resin with a Shell epicure nadic methyl anhydride (MNA) curing agent and Ancamine K61B accelerator The amount of resin required for the impregnation was 210 grams, so according with the weight ration of 100:60:3 the composition of the resin was:

	Bisphenol-A	MNA	Ancamine K61B
Weight (gr)	128	77	4

Table 3.1: Resin component weights for VARTM process

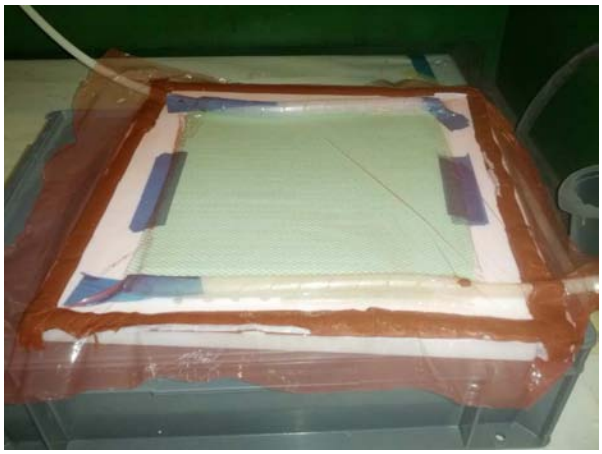

Fig. 3.1: VARTM laminating process lay-up

The VARTM process involved several steps. The first step is the preparation of the mold: a fabric perform (cut to dimension 150 mm x 150 mm) is positioned onto a mold, then the fabric was covered with a top release fabric (so called peel ply). A peel sheet ply (cut to dimensions of 150mm x 150 mm) allows for easy removal of the composite laminate after fabrication from the vacuum bag. This is a porous release material which facilitates the resin flow through and leaves an impression on the part suitable for secondary bonding without further surface preparation. The distribution medium is mesh laid on top of the top release fabric. This helps to maintain an even distribution of resin on the top of the fabric and also facilitates the flow of resin through the thickness of the laminate.

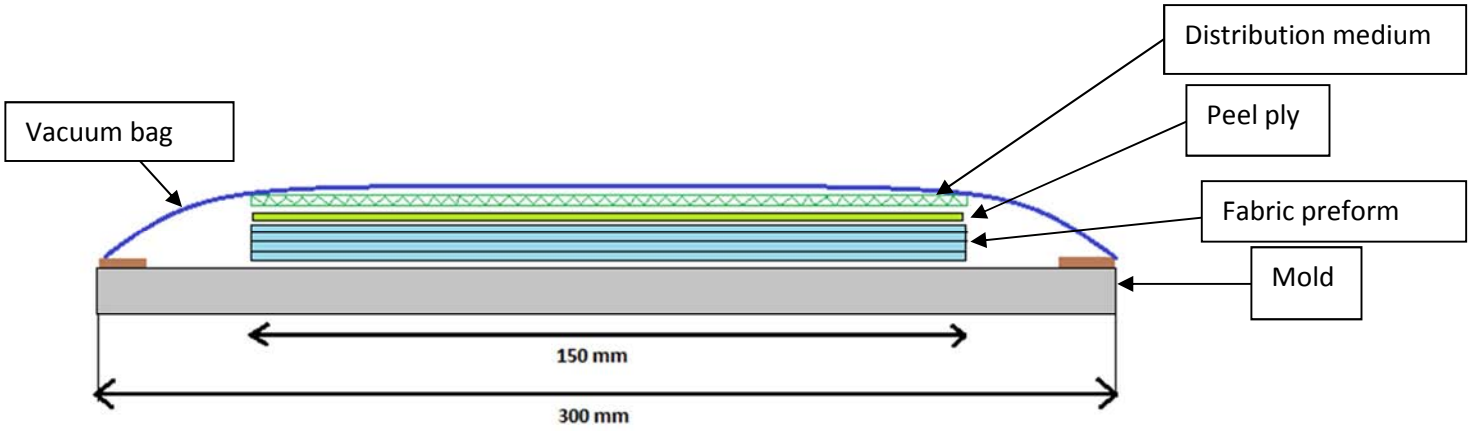

Fig. 3.2: Schematic of the VARTM process

The purpose of the VARTM process was to obtain a transparent laminate, and inm attempting to do this, a number of variations were tried, including changed from a steel then to an PTFE then to an aluminum plate. For every mold used there was an issue with the impregnation as well as with the surface finishing of the laminate. Using the steel plate, the metal oxide handed over from the metal to the resin even if the plate was covered with wax. A PTFE plate prevented the sticking between the surface of the mold and the fabric but its roughness created issues with bubbles trapped in the interface between fabric and mold. On the other hand the top peel ply is porous and when pulled away it created a surface on the laminate that was coarse and unrefined. For this reason a smooth and transparent laminate was not obtainable with this technique and it was decided to move from the VARTM to another manufacturing approach. Laminates manufactured with the VARTM technique were used in some mechanical tests of the material under fatigue load: every laminate has been cut into specimens of dimensions 150

mm x 25 mm and aluminum end-tabs applied onto the. Fig 3.3 shows an example of the surface obtained with VARTM technique.

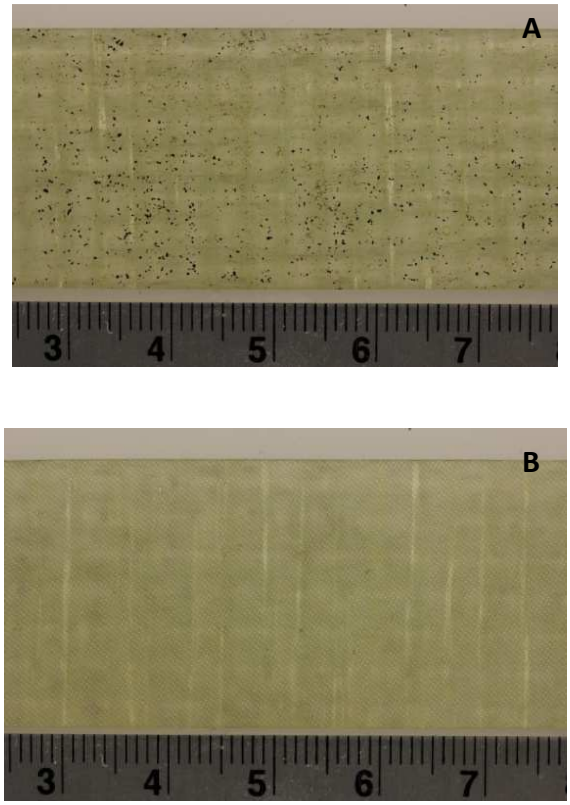

Fig. 3.3: surface finishing of specimen manufactured with VARTM technique (A), (B).

3.2.1.3. The mild-vacuum assisted resin impregnation

The first step was the preparation of the resin: in order to manufacture a laminate with dimensions 320mm x 320 mm the amount of resin has been calculated in 376 gr. Considering the weight ratio of 100:60:3 the exact quantity has been calculated in order to impregnate entirely the fabric.

	Bisphenol-A	MNA	Ancamine K81B
Weight (gr)	230	139	7

Table 3.2: Resin component weights for mild-vacuum assister resin impregnation

The mixture has been stirred in tri-pour for about 10 minute until it was homogeneous without any visual evidence of unmixed components. Afterwards the resin has been degassed in a vacuum oven at a pressure of -1 bar: the degassing time depends on the condition of the resin and the way that it was stirred. If the resin used was stored for a long period the level of cristallinity inside of it increases with time, so the degassing process can last for a time that changes from 30 minutes to 1-2 hours. Nevertheless is possible to check by eye if bubbles are still coming up to the surface during the degassing.

While the resin was degassed, the preparation of the fabric for the wetting was taking place. The second step of the preparation is marking and cutting a 310 mm x 310 mm orthogonal piece of the woven fabric but an important role in the manufacture of this laminate is the presence of a custom-made frame build specifically for this particular laminate. The frame was obtained from four pieces of wood screwed together. The dimensions of the frame are shown in figure 3.4 and it has been introduced to avoid resin spillage during all the wetting and curing process inside the oven.

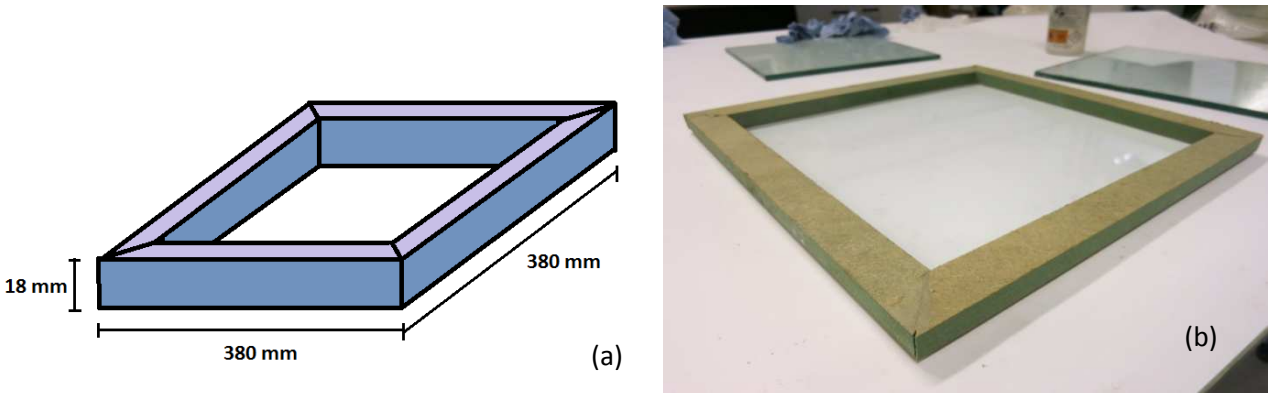

Fig. 3.4 (a): Frame schematic and dimensions; Fig. 3.4 (b) wooden frame used in this work

On one side of the frame has been applied a vacuum bag sealant tape all around the internal edge of the frame (fig 3.5). Once the tape properly attached, the all frame was positioned and pressed in the center of one the release film. This release film also the bottom release film.

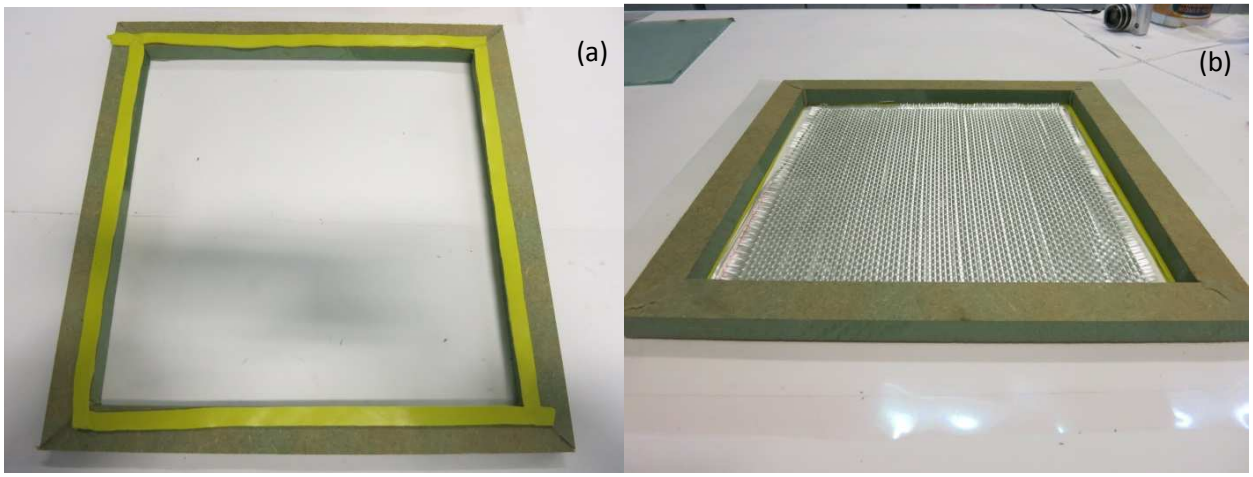

Fig. 3.5 (a): sealant tape positioned around the edges of the frame; Fig 3.5 (b) :cloth placed inside the frame

Then the cloth was placed inside the frame, paying attention of the alignment of the fabric by visual inspection.

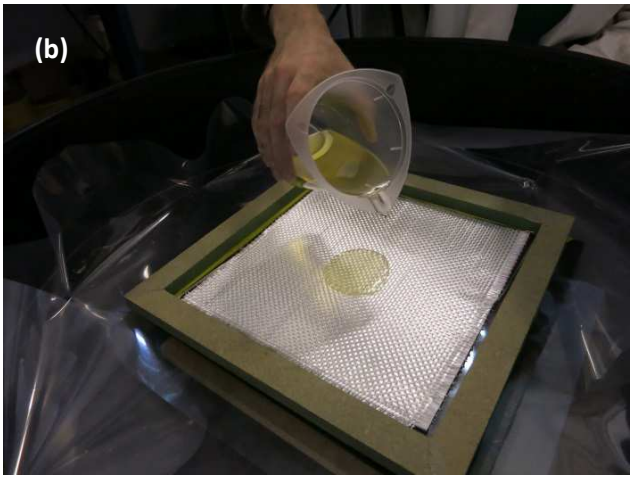

Fig. 3.6a: Glass plate covered with wax; *Fig 3.6b: Pouring of the resin inside on the cloth*

The following step is the preparation of the vacuum chamber and both of the glass plates. Before introducing the frame (with the fabric) inside the vacuum chamber, a pre-heated (140 °C) steel plate has been positioned on the bottom of the chamber in order to create a temperature difference with the purpose of improve the wetting. A glass plate (fig. 3.6a) was positioned on top of the pre-heated steel plate: this glass plate was covered covered with a layer of wax in order to prevent the adhesion of the glass to the silicon coated release film (which is the bottom of the frame).
Once the frame was positioned on top of the glass plate, the resin has been poured manually taking care of the homogeneous distribution all over the fabric (fig. 3.6b) . The chamber (fig. 3.7a) was sealed and the cloth with the resin was vacuumed at -1 bar for 2 hours. Such a long time is required because of the particular architecture of the fabric: in 2D composites air has preferential directions to escape from the fabric while in 3D woven cloth there is not a preferential way for the air to exit.

Once the vacuum process finished, the fabric with the whole frame has been pulled out from the chamber and placed on a desk for the last part of the laminating process.

At the end of the wetting process the aspect of the cloth is shown in fig 3.7b.

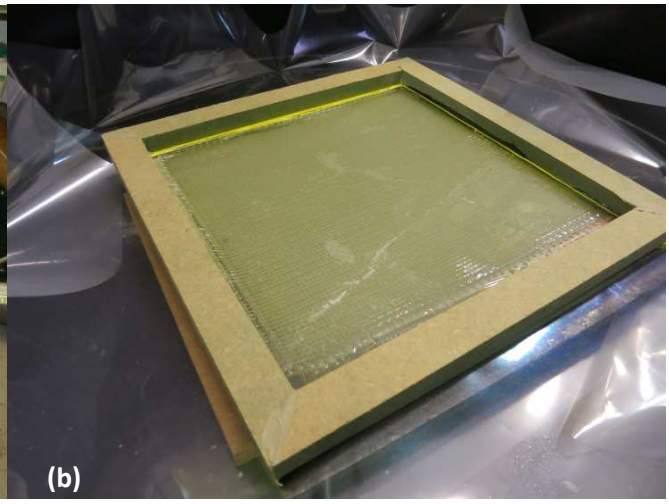

Fig. 3.7a: Vacuum chamber;

Fig. 3.7b: cloth aspect after wetting process

Afterwards the second of the two pieces of silicon coated release film was placed on top of the wetted cloth. This procedure introduced some large air inclusion (air bubbles) in the interface of the wetted cloth and the top release film. The air inclusions were pushed out of the cloth with the help of a small flat piece of plastic. The pressure induced by hand was steadily increasing until all the air inclusions and excess resin were pushed out of the laminate. (fig. 3.8)

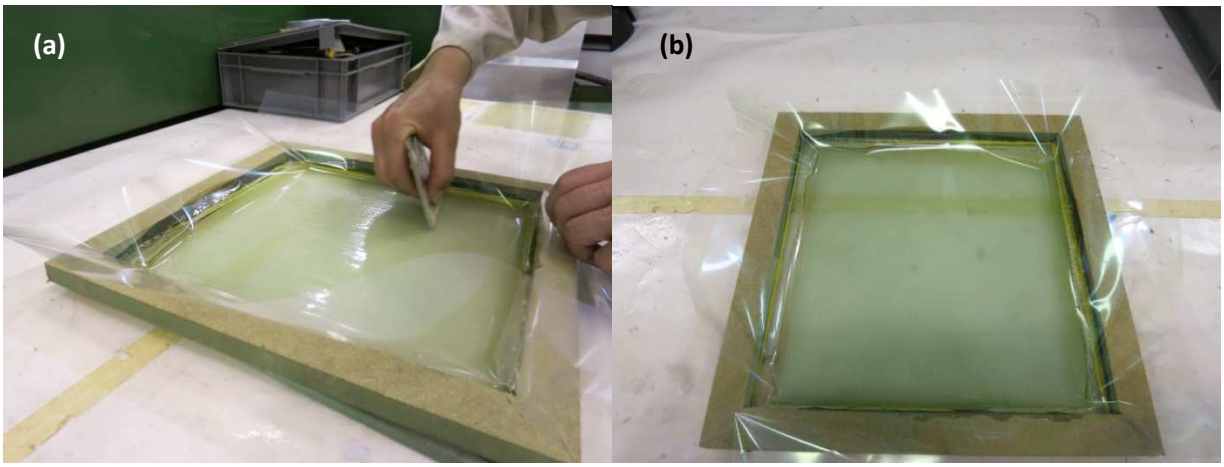

Fig. 3.8a: the by-hand removal of the bubbles ; Fig. 3.8bRelease film placed on top of the wetted cloth

After removing all air inclusions, the second glass plate covered with a layer of wax was positioned on top of release film taking care of not creating surface abrasions or defects over the surface of the release film. The glass applied is shown in fig 3.9a.

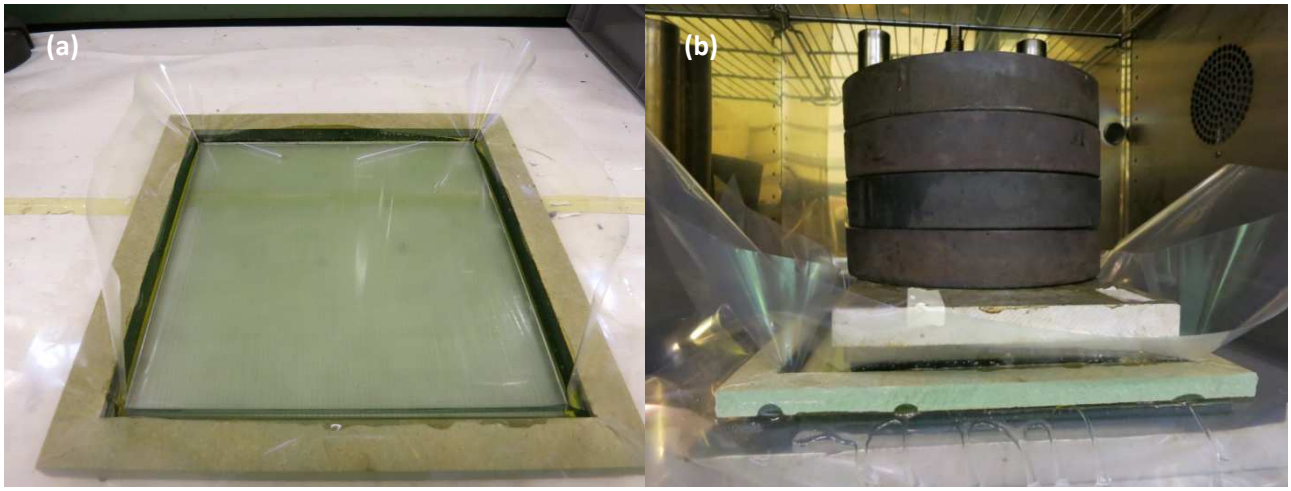

Fig. 3.9a: Glass plate positioned on top of the release film; Fig 3.9b: Rig mounted inside the laboratory oven

The laminate was placed inside a special rig designed to apply isostatically the pressure of 72 kg which, normalized by the area of plate, was about 7,80 KPa that was placed on the

rig. The rig has been mounted on the inside of a laboratory oven. The laminated was heated for the resin to cure.

The curing cycle of the resin, as shown in fig (…), consisted of three separate steps :

1. Heating to a temperature of 100 °C with a rate of 2,5 °C *min^{-1}
2. Holding the temperature of 100 °C for 3 hours
3. Cooling down to room temperature was with a rate of 2,5 °C*min^{-1}

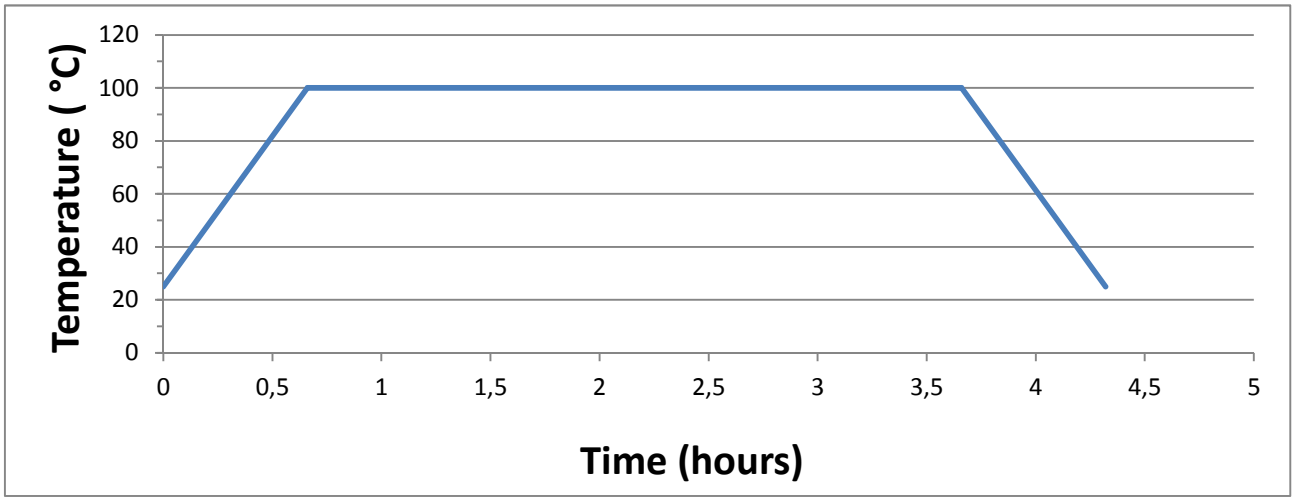

Fig. 3.10: Curing cycle of the resin

3.2.2. Volume fraction measurements.

In order to measure the fiber volume fraction, small specimens (20 mm x 20 mm) were cut out from different area of the laminate. The fiber volume fraction has been obtained using a burn-off test with a high temperature oven. Specimens fitted into small porcelain crucibles which were inserted into the oven and heated at 600 °C for 3 hours and cooled overnight. The volume fraction was calculated by measuring the masses of the empty

crucibles, crucibles with the specimen before the test and after the test. Doing this, it has been possible to calculate the mass of the fibers and the weight of the resin. The formula for the fiber volume fraction is:

$$V_f = \frac{m_f \cdot \rho_m}{(m_f \cdot \rho_m) + (m_m \cdot \rho_f)}$$

where V_f is the fibers volume fraction, m_f and m_m the mass of the fibers and the matrix accordingly and ρ_f and ρ_m the density of the fibers and matrix accordingly. For our measurements the density of the fibers and matrix was 2560 $Kg \cdot m^{-3}$ and 1210 $Kg \cdot m^{-3}$, respectively.

3.2.3. Specimens dimensions and end-tabbing.

Laminates obtained with both techniques (VARTM and mild-vacuum assisted resin impregnation) have been cut into several specimens suitable for the type of tests planned. The laminate obtained was 300 mm x 300 mm and it was cut in specimen of dimension 200 mm x 25 mm (fig 3.11). From a single laminate it was possible to cut out 10 specimens. The cutting direction of the specimens was along the warp direction, so both warp tow and z-tows were parallel to the longest side of the specimen.

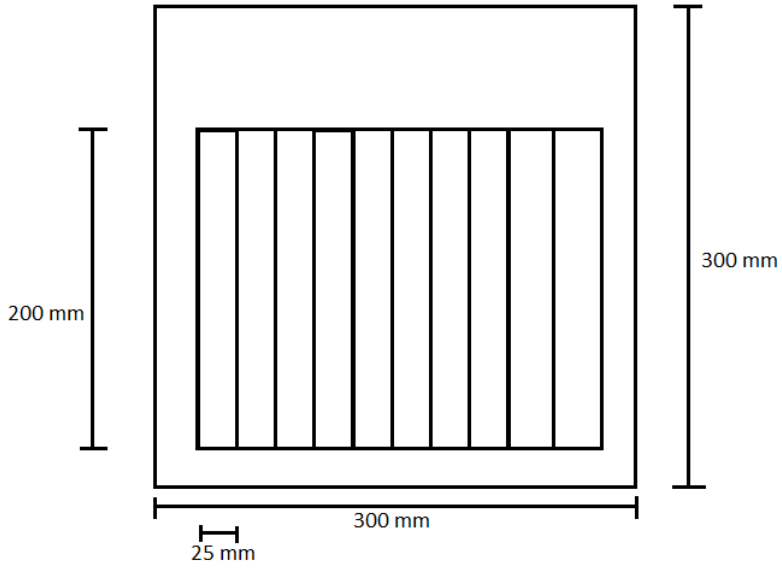

Fig. 3.11 : Schematic of the specimens cut by the laminate

The aim of this project was to investigate the damage development of this composite material during its fatigue life. For this reason X-ray micro computed tomography has been used to observe the internal damage. The micro-CT technique needs specimens with smaller dimensions than 200 mm x 25 mm x 2,2 mm because the optimal image resolution is achievable only if the thickness and the width of the sample are close to each other. An optimal ratio between width and thickness guarantee the same penetration on the X-rays in both directions for a better image quality. For this reason, thinner samples of dimension 200 mm x 8 mm x 2,2 mm were also cut. (fig 3.12)

Fig. 3.12: Specimens of dimension 200 mm x 8mm end-tabbed

3.2.4. Quasi-static and fatigue testing.

The quasi-static tensile tests were conducted on an Instron 6025, 5500R series servohydraulic testing system with a 100 KN Dynacell load cell. The specimens were rectangular with dimensions of 200 x 8 mm x 2,2 mm. The thickness was measured before every test, taking three measurements per specimen. The width was also measured in order to calculate the exact cross section. The gauge length (L_0) was 120 mm, and the grips were covered with end tabs for enhanced friction. A schematic of a tensile specimen is illustrated in figure (…)

Fatigue tests were conducted on two Instron series 8800 servo-hydraulic machines, the first machine was equipped with a 100 kN Dynacell load cell, the second one was equipped with a 20 KN Dynacell load cell. The specimens were of the same dimension used for the

quasi-static tests. All specimens were end-tabbed. The software for the test monitoring and data acquisition was Instron's Bluehill v2 software. The data acquisition was set initially to retrieve 1 point of the stress-strain loop describing the fatigue cycle every 0,01 seconds, but going forward with the experiments the acquisition rate has been changed to record a point every 0,002 seconds in order to obtain a higher number of points describing the entire loop. With a higher number of point a better description of the loop was achieved and in consequence of this also a better measurement of the area within the hysteresis loop. The frequency of load application was set to 5 Hz for all the experiments, so every hysteresis loop was described by 100 points. All tests have been performed with a sinusoidal waveform and a R ratio of 0,1.

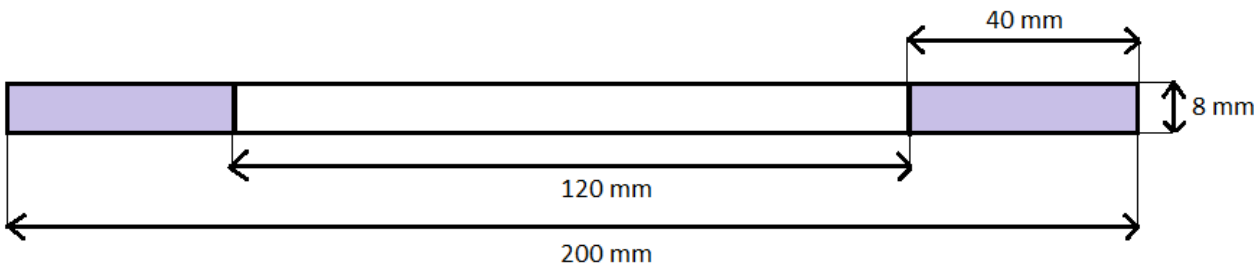

Fig. 3.13 : Sample schematic and dimensions

The S-N curve for the 3D composite studied in this work was found for specimens manufactured with VARTM technique of dimension 150mm x 25 mm and for specimens manufactured with mild-vacuum assisted resin impregnation of dimensions 200 mm x 8 mm.

Using the S-N curve, it was decided to focus for the study on damage accumulation in fatigue on a maximum stress of 175 MPa because the fatigue life was long enough (approximately 50000 ÷ 90000 cycles) to investigate different regimes of damage. The loading direction was along the 0° direction, i.e. the direction of the warp and z-tows.

In order to characterize the stiffness reduction during fatigue, an Instron extensometer was used to record the strain so that hysteresis loops of load against strain could be recorded. Extensometer was attached to the specimen using knife edges and elastic bands. Initially the gauge length of the extensometer was 12,5 mm but it has been changed to a maximum of 96 mm. A long length of 96 mm was important because it permitted to analyze the behavior of the material over the majority of the gauge length of the specimen.

As indicated above, every specimen has been tested with R=0,1 (ratio of minimum to maximum applied stress). An example of a loading waveform is shown in figure 3.14.

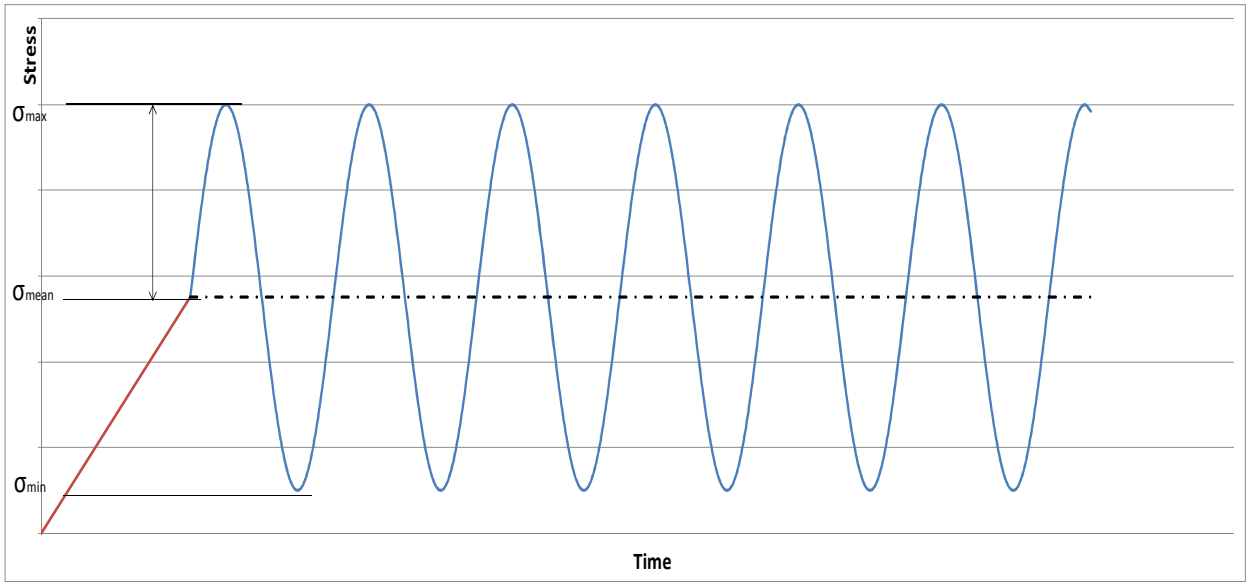

Fig. 3.14 Schematic of the loading application in fatigue testing

The parameters introduced for every test were the mean load and the amplitude of the cycle: the software was programmed to reach the mean load with a ramp of 5 seconds and only after that the cyclic loading was applied between the maximum and the minimum stress. Mean load and amplitude are defined as:

$$\sigma_{mean} = \frac{\sigma_{max} + \sigma_{min}}{2}$$

$$Amplitude = \sigma_{max} - \sigma_{mean}$$

$$R = \frac{\sigma_{min}}{\sigma_{max}}$$

In fatigue, unless the cycling is entirely within the linear-elastic regime, every cycle experienced by a material can is characterized by a loss of energy related to the damage within the material's structure. When a material behaves elastically, the work done on straining is stored as energy in it, and this is released on unloading. However, when the load or strain is large enough, some of this elastic energy gets convert into surface energy when there is the creation of new surfaces as cracks, fractures, delaminations and every other type of damage which changes the structure of the material.

In general, the strain energy density (ρ_e) in a material can be calculated by finding the area under its stress - strain graph; it is the energy stored per unit volume (how many Joules are stored in $1m^3$ of the material).

$$U = \int_{\varepsilon_0}^{\varepsilon_1} \sigma \, d\varepsilon$$

Similarly, the area under the unloading curve is the energy released by the material. In the elastic range, these areas are equal and no net energy is absorbed. If the material is loaded into a range where the energy absorbed exceeds the energy released, the difference is dissipated. In this project, the energy dissipated in every fatigue cycle has been monitored, since this is related to damage events within the material (e.g. energy absorbed through the creation of new fracture surfaces or energy absorbed through friction at mating fracture surfaces). To monitor the hysteresis loops, a numerical method has been used to calculate the area included inside the hysteresis loop.

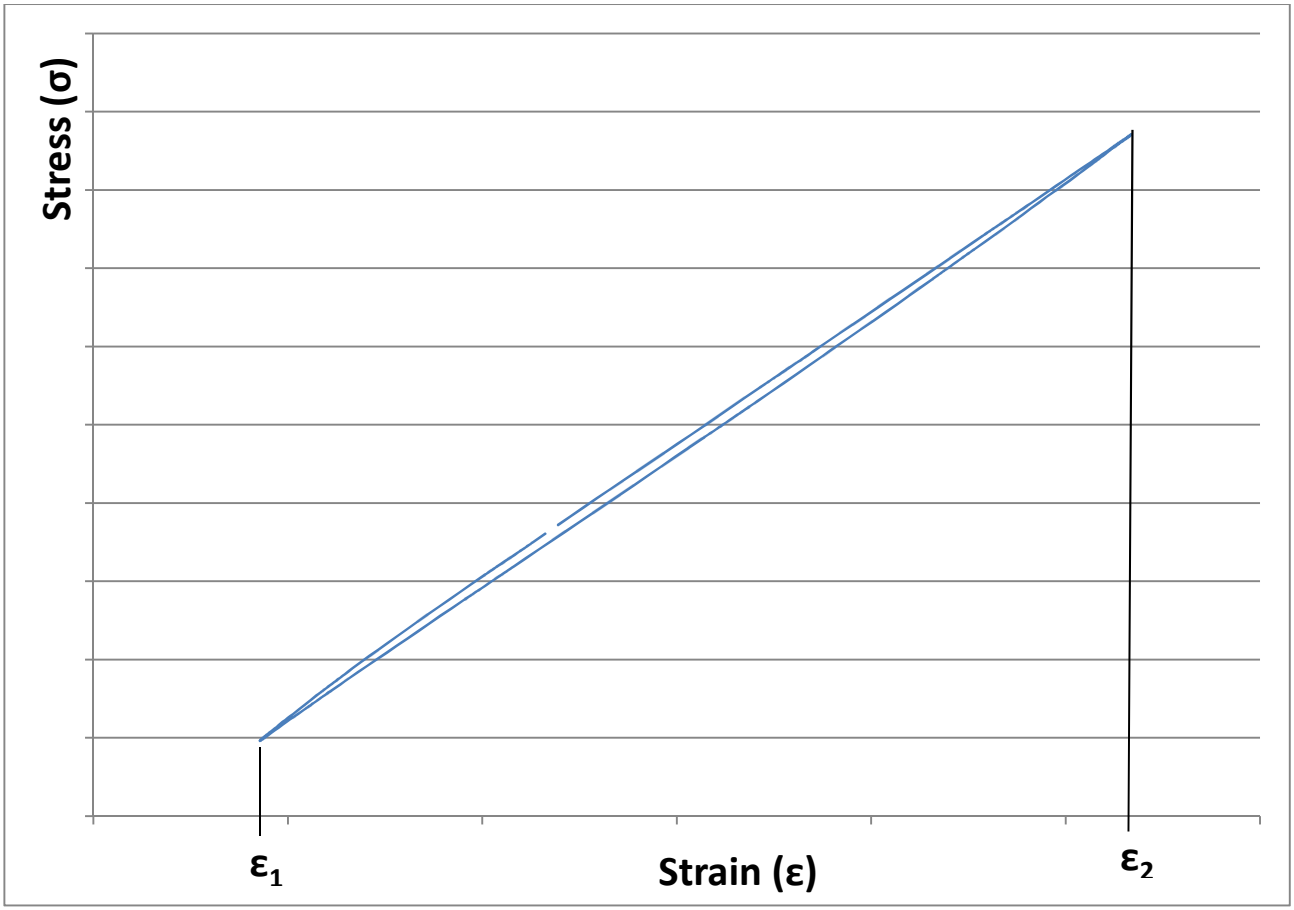

Fig. 3.15 : Example of hysteresis loop in fatigue loading

An example of a hysteresis loop recorded in these tests is shown in figure [WHAT?]. The area within the loop was calculated with the “trapezoid rule”. It is a method for approximating a definite integral using a linear approximation of the function. This rule divides the area under the curve into n trapezoids from x=*a* to x=*b*, so the interval of integration is divided into n sub-intervals of equal width. The width Δx of each sub interval is given by

$$\Delta x = \frac{b-a}{n}$$

The difference between the area under the σ-ϵ curve that describes the application of the load and the area under the unloading curve is the energy that got lost during that specific cycle. The integral $\int_a^b f(x)dx$ is estimated by adding areas of all the trapezoids, where the area of a single trapezoid is calculated as

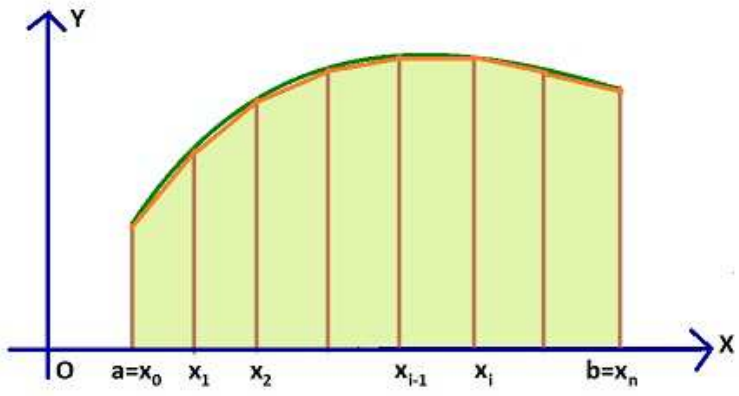

$$\int_a^b f(x)dx = (b-a)\left[\frac{f(a)-f(b)}{2}\right]$$

A measure of the current stiffness of the material was also obtained from the hysteresis loop by calculating the current Young's modulus using the minimum and maximum values of stress and strain of the loop's peaks.

After testing, some specimens were investigated for damage using either optical microscopy or X-ray micro computed tomography, or a combination of both techniques. The techniques used are described in the following two sections.

3.2.5. Optical microscopy.

The specimens after sectioning with a saw equipped with a SiC cut-off wheel. The cutting speed was set to 0,075 mm/s in order to avoid the introduction of damage inside the samples. Samples were mounted in epoxy cylinders of diameter of 25 mm using Strueurs epofix kit. After mounting, the specimens were ground and polished following the schedule of tables 3.3 and 3.4, accordingly. Both grinding and polishing were conducted on a Strueurs Pedemax-2 in groups of three specimens.

GRINDING				
Step	1	2	3	4
Grinding media	SiC	SiC	SiC	SiC
Grain size	600	1200	2400	4000
Lubricant	Water	Water	Water	Water
Pressure (N)	90	90	90	90
Speed (Rpm)	300	150	150	150
Time (s)	Until flat	30	30	30

Table 3.3: Grinding steps sequence

POLISHING			
Step	1	2	3
Polishing cloth	DP-DUR	DP-DUR	DP-DUR
Polishing media	Diamond suspension	Diamond suspension	Diamond suspension
Grain size	6 µm	3 µm	1 µm
Lubricant	Struers blue lubricant		
Pressure (N)	90	90	90
Speed (Rpm)	150	150	150
Time (s)	300	300	240

Table 3.4: Polishing steps sequence

After grinding and polishing the surfaces, the samples were cleaned from any possible contaminations, using water and methanol. Afterwards the samples were ready for microscopy that was conducted on a Zeiss axiophot transmitting light microscope and the images were captured and scaled using Zeiss's axiovision software.

3.2.6. Micro computed tomography.

3.2.6.1. Introduction

X-ray micro-CT has become an important tool for investigating all kinds of materials. The technique uses X-ray transmission images of a sample to create a 3D representation of the specimen. The technique is based on the transmission of X-rays through an object. The law of Lambert-Beer states that the intensity, *I*, of a beam passing through an object is given by:

$$I = I_0 e^{-\mu t}$$

Where I_0 is the intensity of the incident light and μ denotes the attenuation coefficient.

After taking a series of X-ray transmission images of the sample from different angles, a computer algorithm combines these slices and can build a full 3D model of the sample. Since the energies of the photons are too low to excite the sample, the technique is completely non-destructive. This makes X-ray CT an excellent candidate for research on samples that are either very rare or expensive, or when the sample may not be altered or damaged during the course of the research.

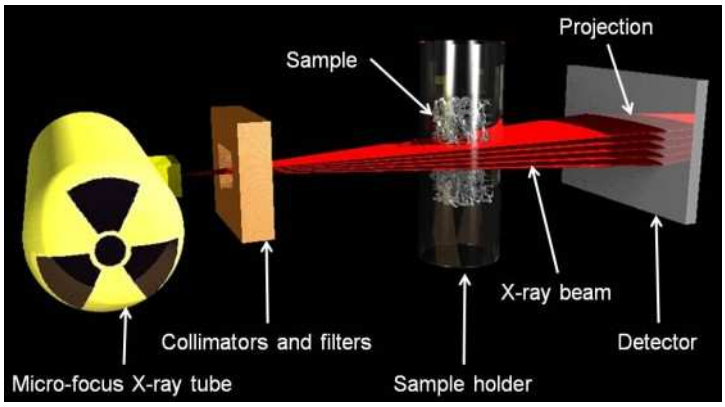

Fig: 3.16 Main components and working principle of a microCT scanner. A micro-focus X-ray tube emits X-ray, which is collimated and filtered to narrow the energy spectrum. The X-ray passes then the object and is recorded by a two-dimensional CCD array. A full scan involves a set of projections under different rotations of the object.

The micro-CT analysis on our specimens of 3D composites has been performed in collaboration with the Materials Science department of the University of Manchester. Two specimens were analyzed and both of them have been tested until the damage was about to cause catastrophic failure.

In order to obtain an optimal magnification and resolution it was decided to scan an area of dimension 8 mm x 8 mm x 2,2 mm which corresponds approximately to the size of a single unit cell of the fabric (a unit cell contains two warp tows, three orthogonal weft tows and a z-tow. In some cases, a combination of X-ray micro computed tomography and optical microscopy has been used, as will be described later.

4. Mechanical test result

4.1 Introduction

In this chapter will be presented the results of the mechanical testing performed on the specimens manufactured with VARTM and mild-vacuum assisted techniques. Quasi static tests and fatigue tests have been performed using the Instron servo-hydraulic machine described in the previous chapter. All the specimens have been tested in the warp direction.

4.2 Static tests

Figures 4.1 and 4.2 show two stress-strain curves of the 3D specimens tested in warp direction. The calculated values of the Young's modulus (E), ultimate tensile strength (UTS) and the measured strain to failure (ϵ) are given in Table 4.1. Young's modulus values were calculated in the strain region of 0.1% to 0.2% where the stress-strain curve is linear.

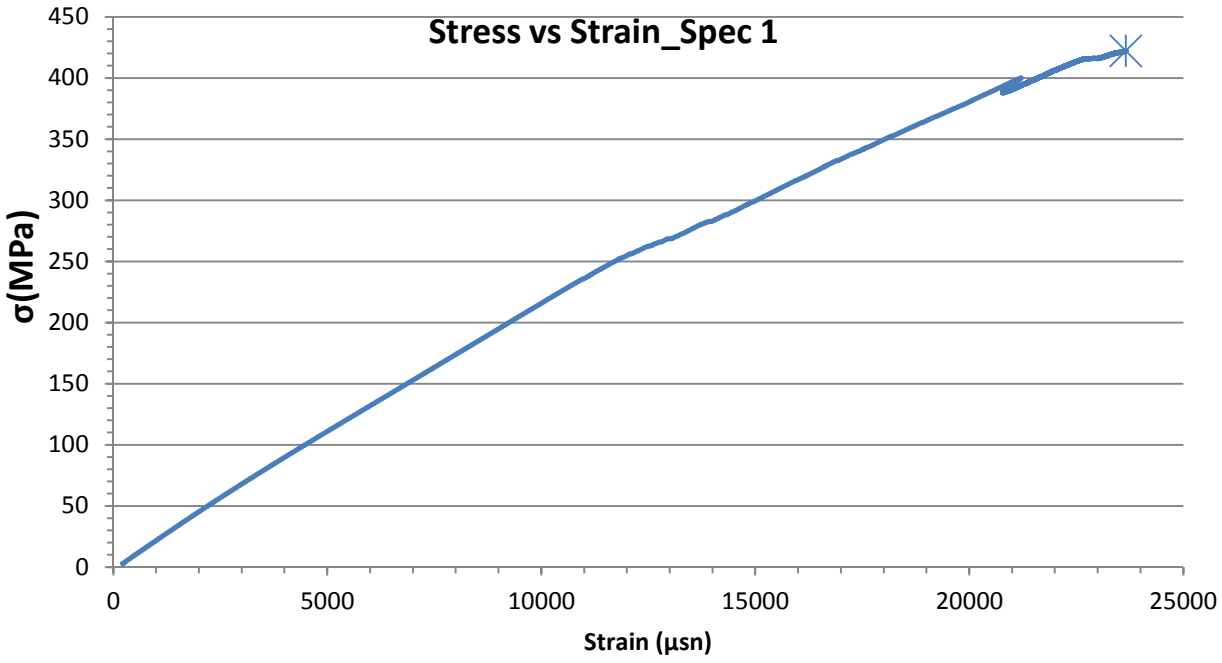

Fig 4.1 Stress-strain curve for a 3D specimens loaded in warp direction

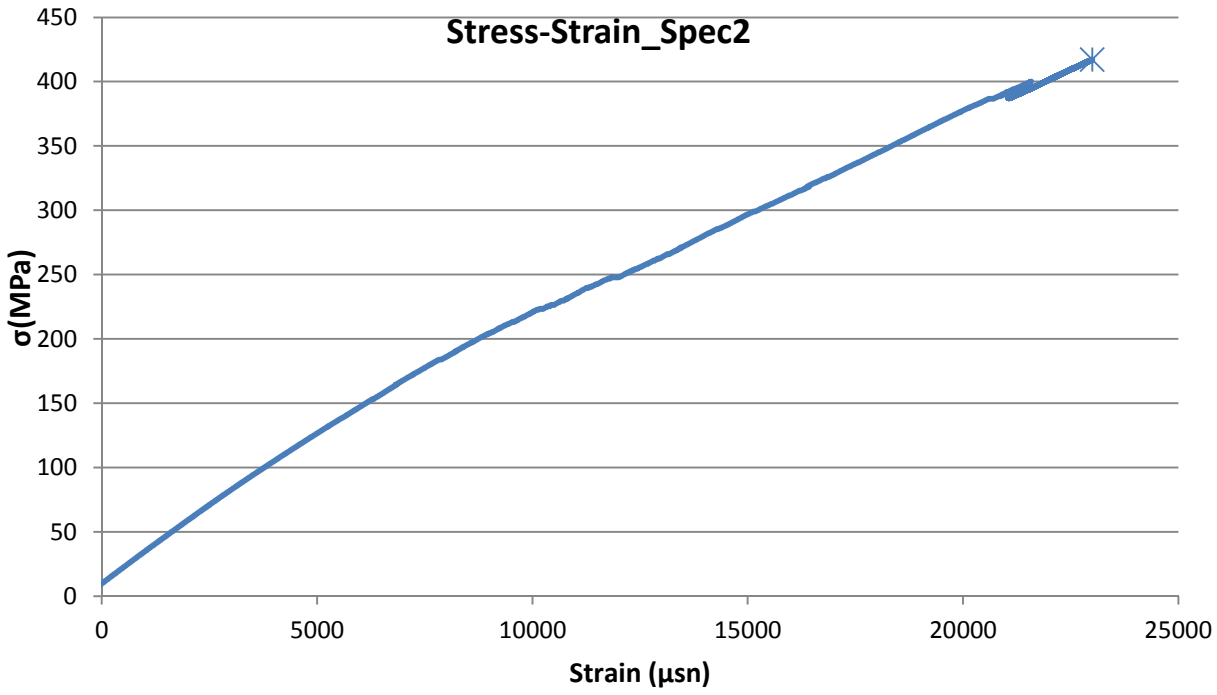

Fig 4.2 Stress-strain curve for a 3D specimens loaded in warp direction

Table 3.1 Dimensions and mechanical properties in warp direction

Specimen	Width(mm)	Thickness(mm)	E (GPa)	UTS(MPa)	Єmax (%)
1	8.18	2.21	23.5	422	2.36
2	8.20	2.17	24.2	417	2.30

Kakaratsios (2010) have conducted tensile tests on the same 3D E-glass woven composite with same weaving pattern and same amount of fiber as this experimental work. Also, Kakaratsios measured the fiber volume fraction to be 0.46 that is the same fiber volume fraction measured for this experimental work. The mechanical properties he measured are shown in Table 4.2.

Table 4.2 Mechanical properties in warp direction from literature [16]

Specimen	E (GPa)	UTS (MPa)	Єmax (%)
3D-78 Warp direction	23.7 ± 0.9	420 ± 20	2.4 ± 0.1

Lomov et al. (2009) have also conducted tensile tests on composites manufactured with the same 3D cloth, with a similar fiber volume fraction of 0,47. The results of the mechanical properties they found are reported in table 4.3.

Table 3.3 Mechanical properties in warp and weft direction from literature

Direction	E (GPa)	UTS (MPa)	εmax (%)
Weft	23 ±2,5	427 ± 8	3,1 ± 0,4
Warp	23± 2,5	429 ± 9	2,9 ± 0,5

Results obtained for this experimental work agree well with with the results of Lomov et al and Kakaratsios.

4.3. Fatigue test results

4.3.1. S-N curves

The following S-N curves shown in this paragraph are S-N curves of the 3D specimens. The two curves represent maximum stress in the fatigue cycle plotted against the number of cycle to failure for each specimen. Three different types of specimen were tested: wide specimens (25 mm wide) manufactured using a VARTM technique, wide specimens

manufacture using the light vacuum assisted (LVA) technique, and narrow specimens manufactured using the LVA technique.

The S-N curve in fig 4.3 was obtained by testing specimens manufactured with VARTM technique and mild vacuum assisted impregnation which were cut into specimens of dimension 150 mm x 25mm x 2,2 mm. Table 4.4 shows the dimensions , fiber volume fraction (where measured), peak stress and number of cycles to failure for every specimen tested. Tests have been performed with a peak stress of 350, 300, 200, 175, 150 MPa. The frequency was set to 5 Hz and kept constant for all tested specimens. For each laminate manufactured with VARTM technique, it was been possible to obtain three specimens.

Table 4.4: Dimension, cycles to failure and fiber volume fraction on specimens manufactured with VARTM technique

Laminate	Peak Stress (MPa)	Width (mm)	Thickness (mm)	Cycles to failure	Fiber volume fraction
1	150	25,1	2,2	75635	-
	200	24,8	2,22	12424	
	300	25,2	2,19	1718	
2	150	25,1	2,38	92447	44,82%
	200	24,9	2,36	5503	
	300	25,2	2,37	717	
3	150	26,2	2,38	35985	43,51%
	200	26,2	2,32	8245	
	300	25,9	2,39	966	
4	150	26,2	2,2	49613	49,21
	200	26,1	2,21	7539	
	300	26,1	2,22	993	
	350	25,5	2,2	498	
5 (LVA)	175	25	2,2	29413	46,82%
	175	25	2,2	44208	
	150	25	2,2	310000	

It has to be noticed that laminates 2 and 3 presented a lower volume fraction due to some air leaks during the impregnation process which brought to the presence of an excess of resin on the top surface of the laminate. Laminate 4 presented a higher fiber volume

fraction because the impregnation process has been conducted without the distribution media in order to obtain a better top surface finishing. The lack of the distribution media caused the peel ply to follow the profile of the surface under vacuum pressure. Interestingly, the variation in fibre volume fraction for these laminates does not appear to have significantly affected the fatigue S-N curves. Laminate 5 was manufactured using the LVA technique. The fatigue response is similar to the specimens manufactured using the VARTM technique.

Sample number	Thickness (mm)	Width (mm)	Peak stress (Mpa)	Cycles to failure
1	2,15	7,95	350	603
2	2,15	7,97	350	534
3	2,15	7,86	300	1240
4	2,15	7,85	300	1050
5	2,15	7,93	250	4212
6	2,15	8,2	250	9010
7	2,15	7,95	200	14598
8	2,15	7,9	200	26047
9	2,18	8,19	175	46523
10	2,2	8,21	175	92280
11	2,2	8,16	175	90750
12	2,19	8,2	175	46646

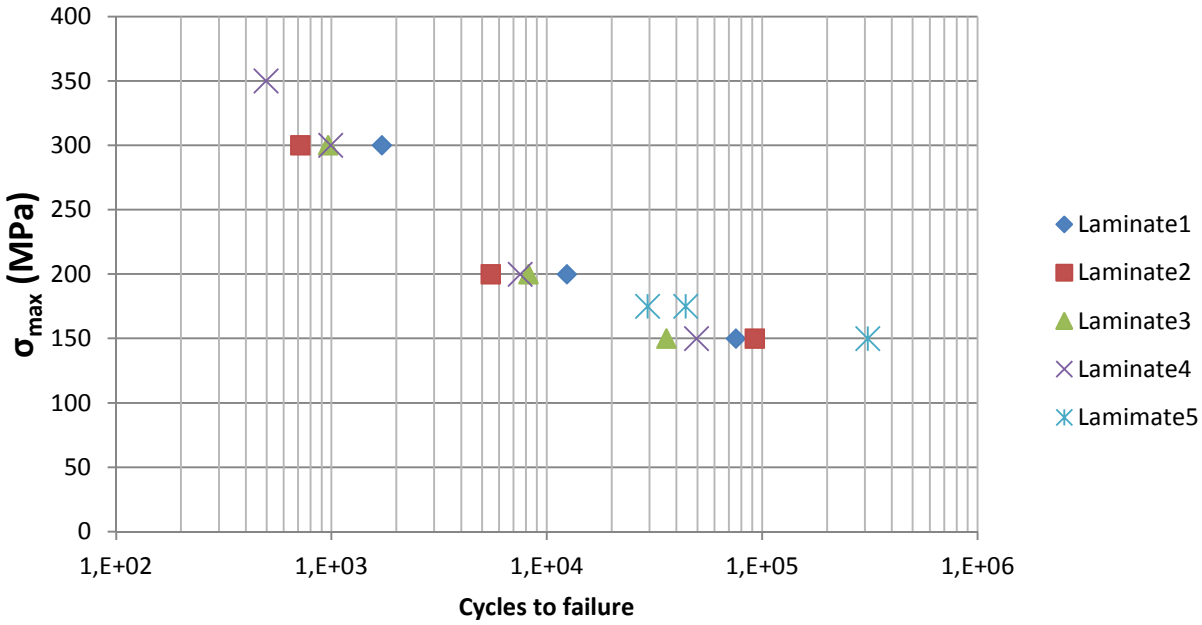

Fig. 4.3: S-N curve for specimens manufactured with VARTM technique

The S-N curve shown in fig 4.4 was obtained by testing specimens of dimension 200 mm x 8 mm x 2,2 mm which were manufactured with mild vacuum assisted resin impregnation. Table 3.5 illustrates samples dimensions, peak stress levels and number of cycles to failure. The LVA technique produced a fiber volume fraction of the specimens has been measured of 0.468 which is comparable with the volume fraction of the specimens manufactured with the VARTM technique. One interesting question, is whether the use of the narrower specimens has affected the fatigue S-N curve. A comparison of the wide and narrow specimens, showing the VARTM and LVA specimens is shown in Figure 4.5. his suggests that there is no significant difference in the results for the wide and narrow specimens.

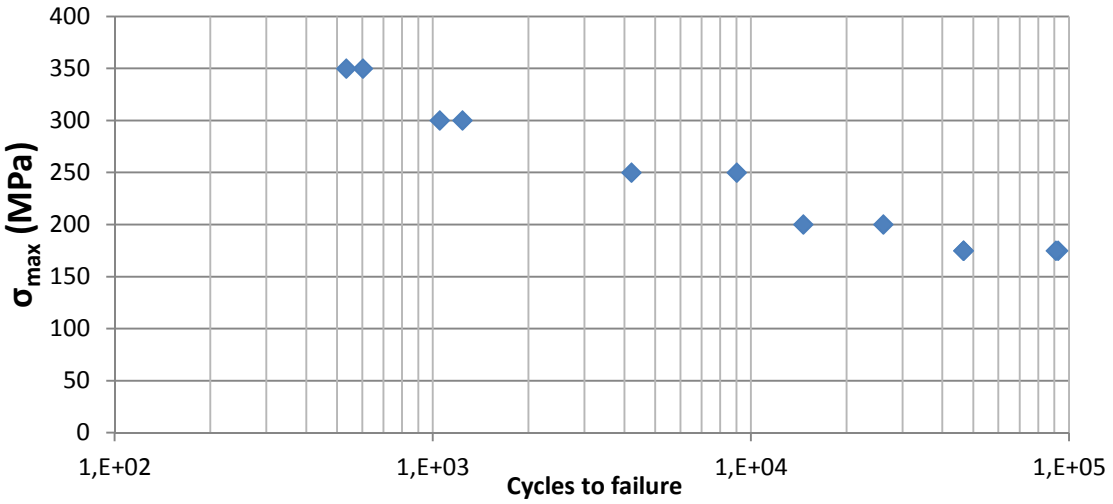

Fig. 4.4 S-N curve for specimens manufactured with mild-vacuum assisted resin impregnation

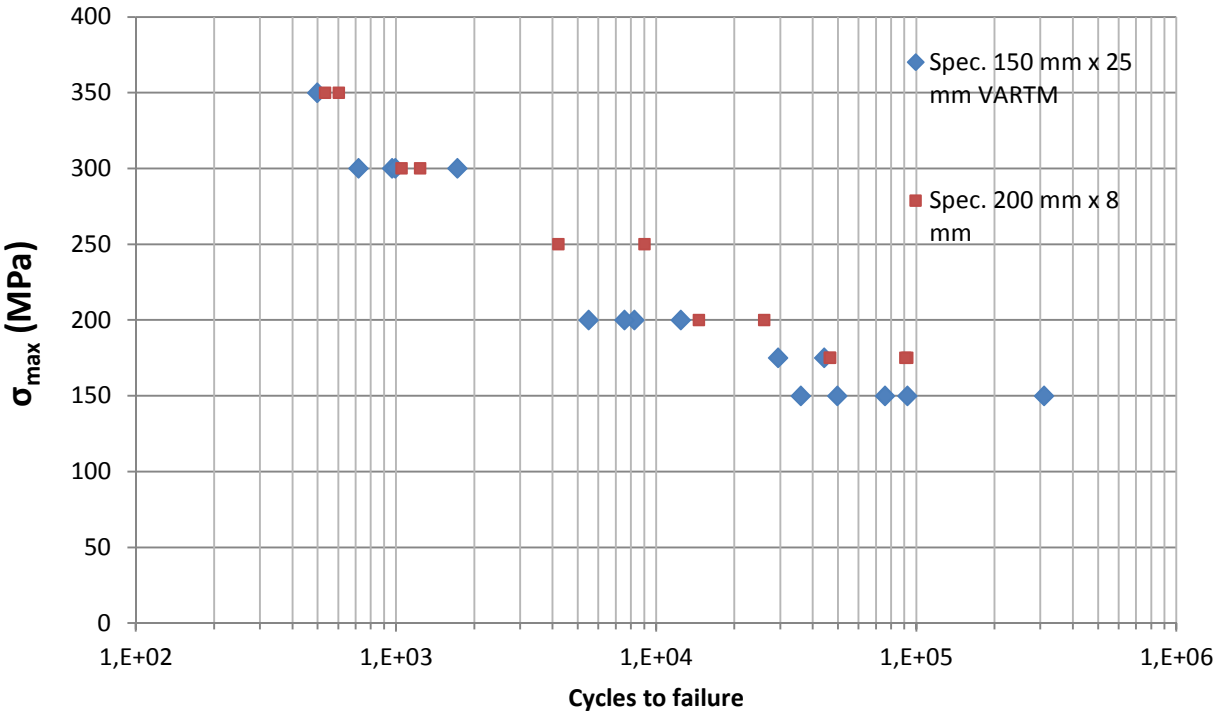

Fig 4.5 Comparison of S-N curves of soecimens of different size

In fig 4.5 the results of the two S-N curves, obtained with two different widths of specimens, are reported together in the same graph. Looking at the curves trend is possible to assert that there are no relevant differences between the two sizes of specimens and between the two manufacturing techniques that were used.

Carvelli et al. studied the fatigue behavior of a similar 3D woven E-glass composite material "3WEAVE" provided by 3Tex. The 3D composite they studied was labeled as "3D-96", which fiber architecture has three warp tows and four weft tows with an areal density of 96oz*yd-2 . Carvelli et al. fabricated panels using Dow Derakane 8084 Epoxy-Vinyl Ester resin in a vacuum bag using Vacuum Assisted Resin Transfer Molding (VARTM). The frequency was not been kept constant in the fatigue tests since it has been moved from 1 Hz for the 350 MPa test to 10 Hz for low-stress test. They studied the fatigue performances in both warp and weft direction and the S-N curve for the warp loading direction are shown in fig 4.6.

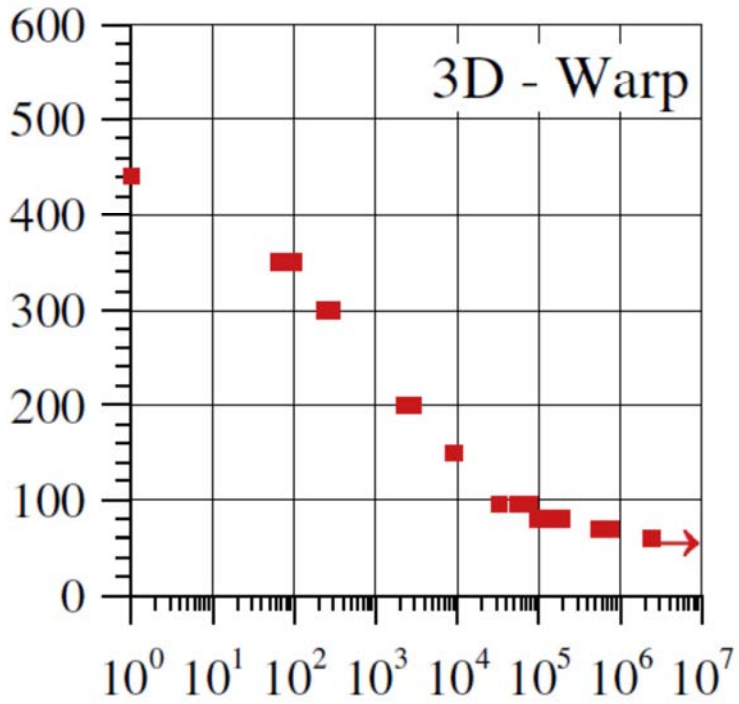

***Fig 4**.6 S-N curve from literature of "3D-96" loaded in warp direction*

A comparison between the result shown in fig 4.6 and the result achieved in this experimental work is shown in fig 4.7.

A comparison between the result shown in fig 4.6 and the result achieved in this experimental work is shown in fig 4.7.

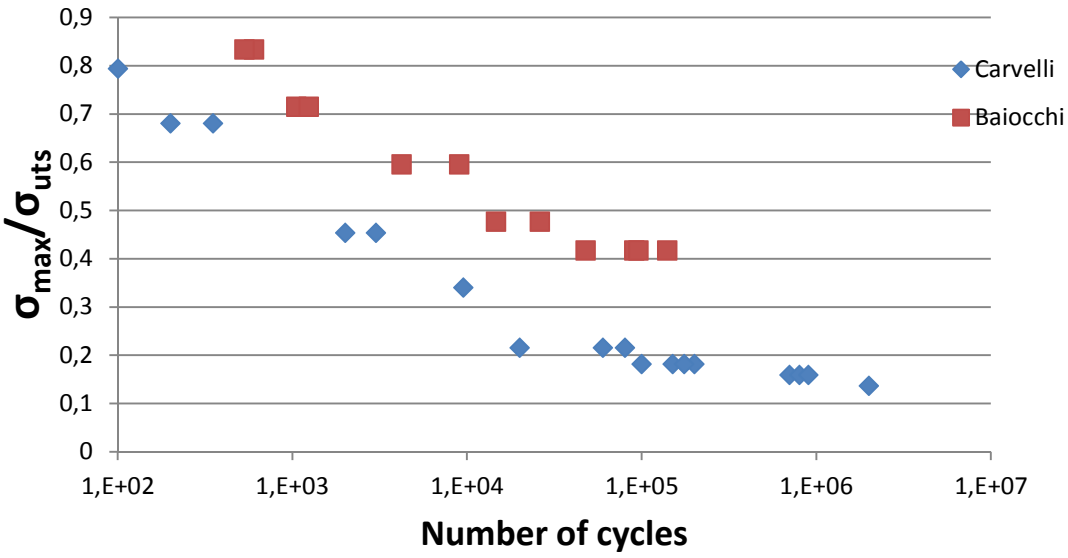

Fig 4.7 Comparison with literature results

It is possible to observe from fig. 4.7 that the S-N curve achieved in this experimental project is shifted to higher fatigue lifetimes for the same stress level by about a factor of 10. This is probably due to the different type of resin used for the impregnation, and the different fabric. Carvelli et al. used an epoxy-vinyl ester resin which has less performance than the epoxy resin used in this work.

4.4 Stiffness reduction and hysteresis loops.

In this paragraph will be shown the results for the stiffness and the hysteresis loops with the number of cycles. Specimens tested have shown a reduction in the Young's modulus (stiffness) with cycling and also changes in the hysteresis loop area. The area within the hysteresis loops is a measure of the enegy dissipated every cycle, which is related to the damage occurring inside the sample. The following sections describe the results for five

specimens; some of them have been brought to catastrophic failure while the test of other specimens has been stopped to a pre-set number of cycles.

4.4.1 Tests interrupted before failure (specimens n.1 and n.2)

This specimen was been tested to 10000 cycles at a peak stress of 175 MPa. In the test, an extensometer with a gauge length of 96 mm was used. The acquisition rate for every cycle was set to record 80 points (a point every 0,002 seconds) for each fatigue cycle . The normalized stiffness reduction (i.e. the current Young's modulus divided by the initial Young's modulus) stiffness is shown in figure 4.8. It can be seen that over the 10,000 cycles before the test was stopped, the Young's modulus reduced rapidly over about the first 2000 cycles, followed by a more gradual reduction. The hysteresis loop energy dissipation is plotted in figure 4.19 for the same specimen. It can be seen that the area of the hysteresis loops is relatively large initially, for about the first 2000 cycles, after which the area is much smaller.

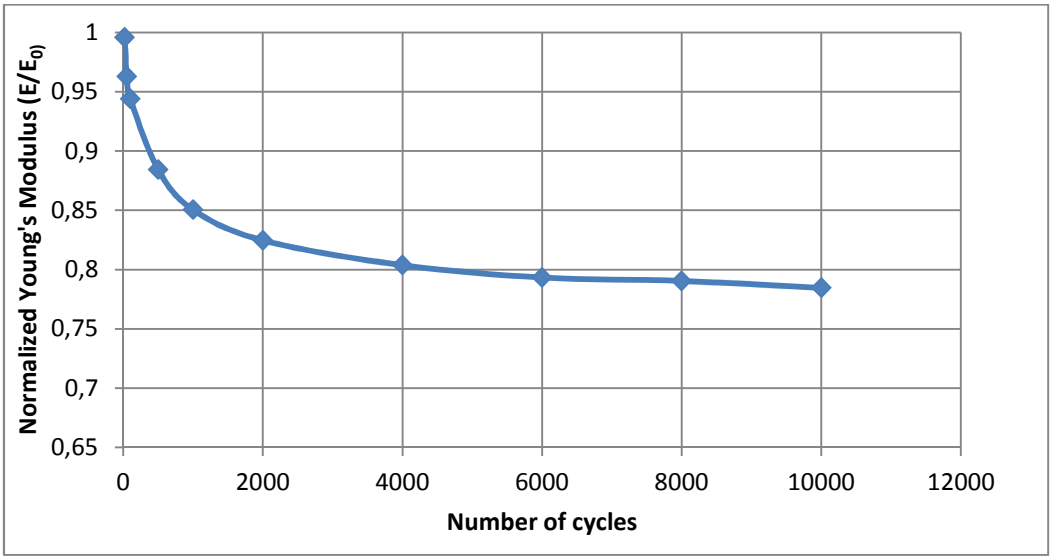

Fig 4.8 Normalized Young's modulus vs cycles. Frequency 5Hz, Spec.1

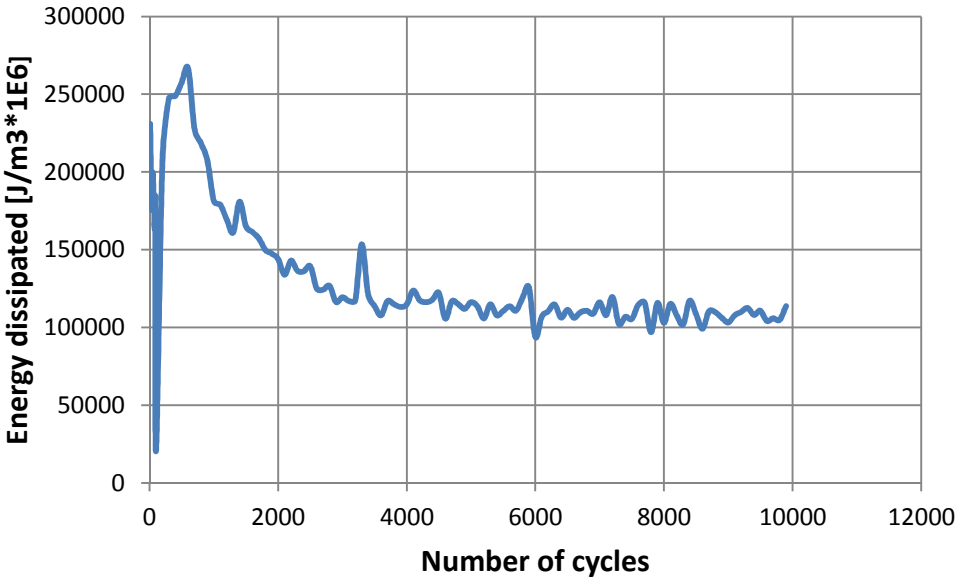

Fig.4.9 Hysteresis loop vs cycles- test stopped at 1000 cycles- Frequency 5 Hz

Sample n.2 was been tested for 40000 cycles at a peak stress of 175 MPa and then the test was stopped. The test was been performed at a frequency of 5Hz and the gauge length of the extensometer was again 96 mm. The stiffness reduction and the hysteresis loops with the number of cycles are illustrated in fig 4.10 and 4.11.

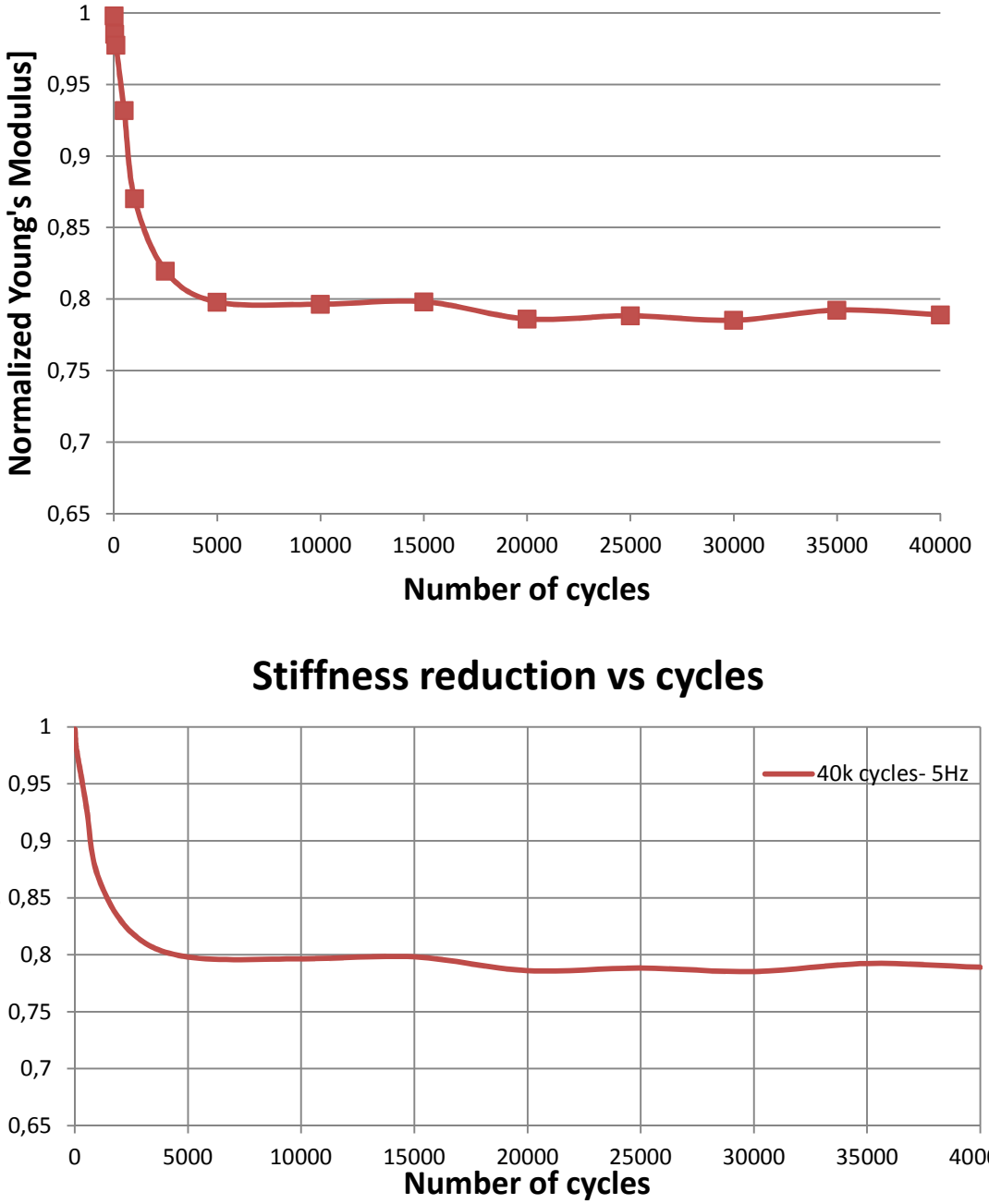

Fig 4.10 Normalized Young's modulus vs cycles- test stopped at 40000 cycles. Frequency 5Hz

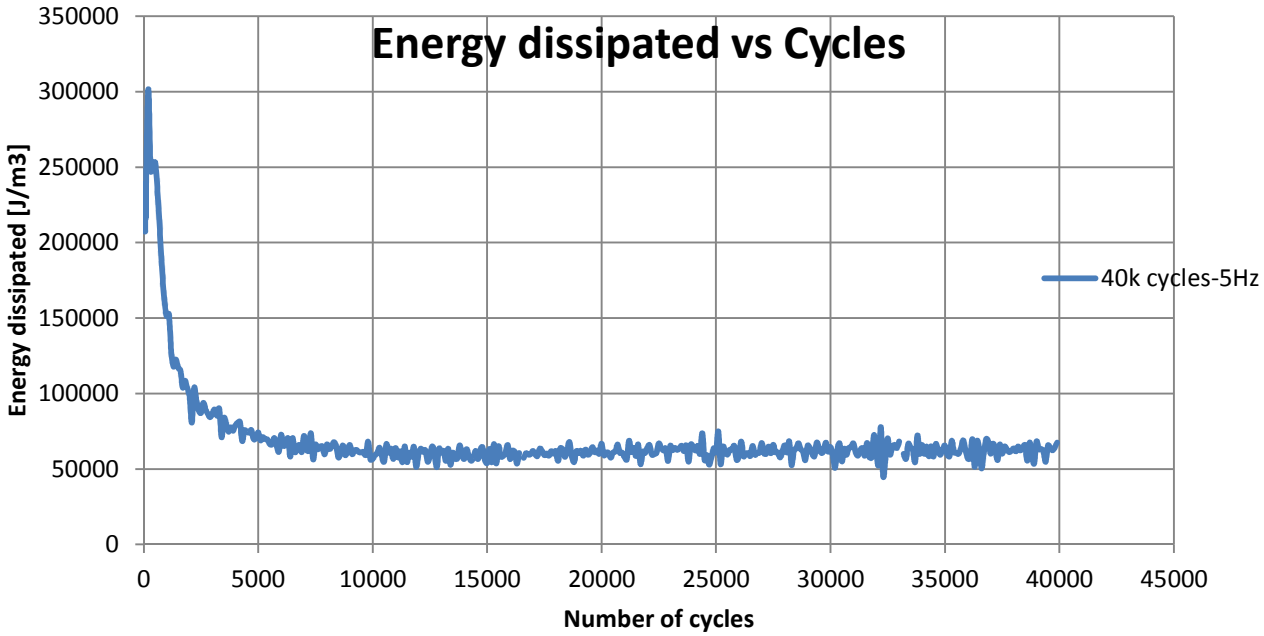

Fig 4.11 Hysteresis loop area vs cycles- Test stopped at 40000 cycle. Frequency 5Hz

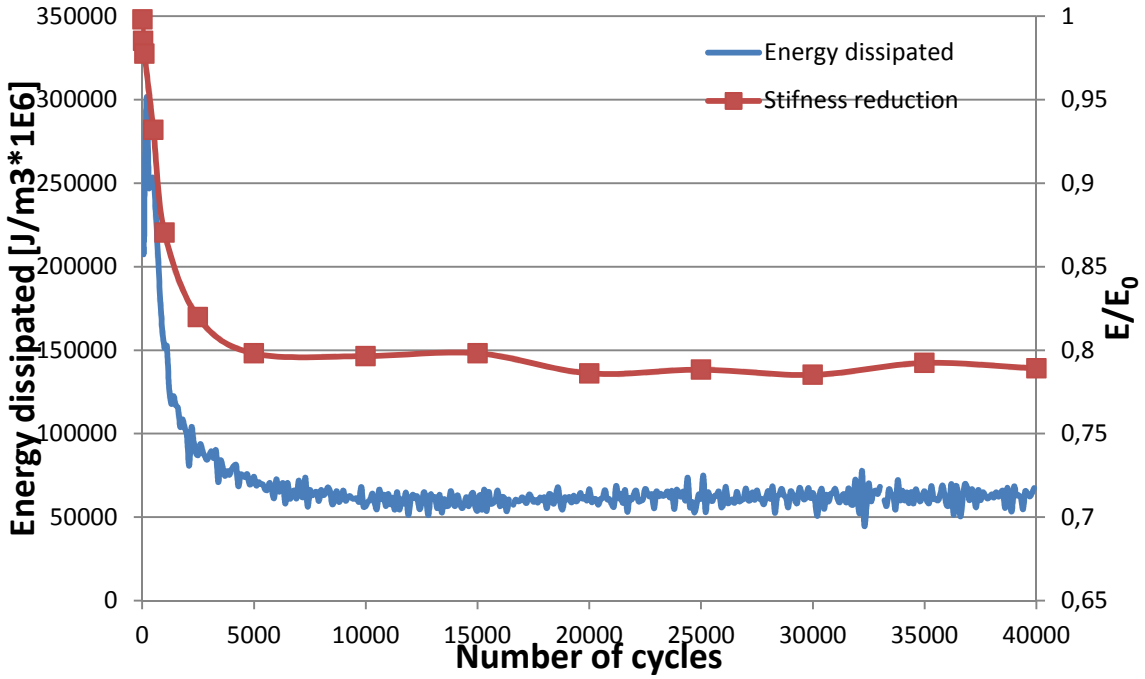

Fig 4.12 Direct comparison between stiffness reduction and hysteresis loops

The graph presented in fig 4.12 shows the relationship between the stiffness reduction and the trend of the area within the hysteresis loop representing the lost energy for every cycle; a similar trend can be seen as for specimen n.1.

At the same time, the energy dissipated has a peak around cycle 200 before decreasing quickly by 5000 cycles before remaining constant until the end of the test at 40000 cycle.

The stiffness decreased to a ratio E/E_0=0,78 within the first 5000 cycles. After this value it began to decrease very slowly with the number of cycles. Similarly the area of the hysteresis loop reached a constant value after 5000÷6000 cycles after reaching a peak after a few hundreds of cycles in early fatigue life.

4.4.2 Tests taken to failure

A further three specimens (n.3, n.4 and n.5) were tested at 175 MPa and all of them were brought to catastrophic failure. It should be noted that in this cases the extensometer has not been taken off before the failure, and the long gauge length (96mm) of the extensometer allowed changes in stiffness and hysteresis loops to be recorded up to failure. The two following graphs (fig 4.13 and 4.14) show the stiffness reduction and the hysteresis loops separately of specimen n.3 that failed at 46464 cycles. A direct comparison of the two properties is shown in fig 4.15

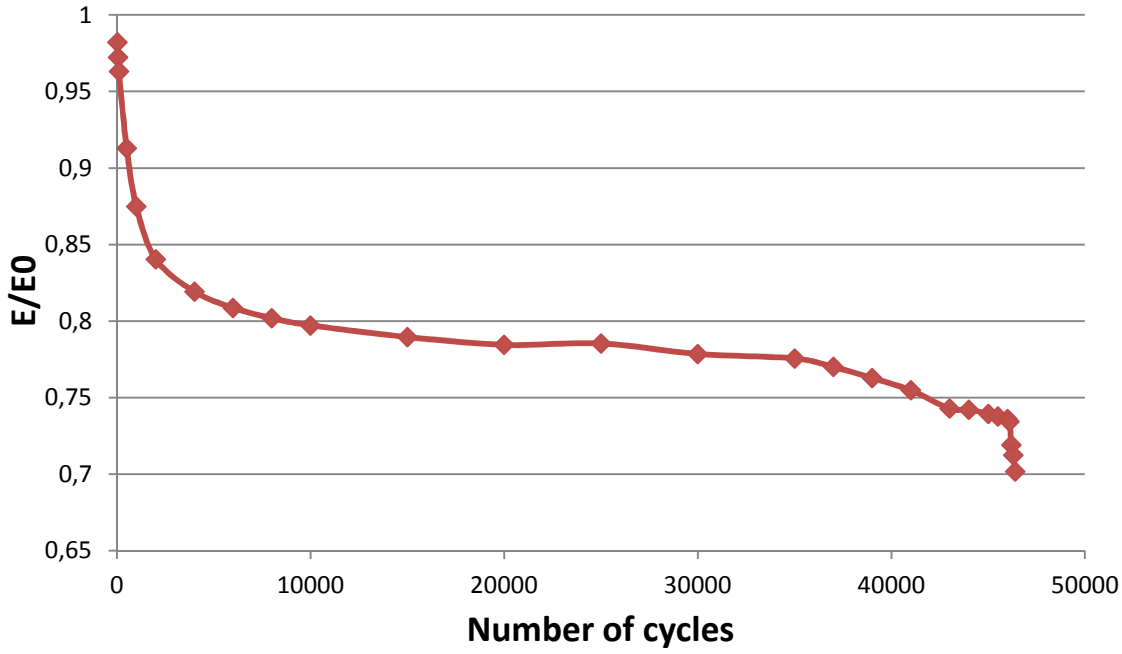

Fig 4.14 Normalized Young's modulus vs cycles. Frequency 5Hz, specimen n.3

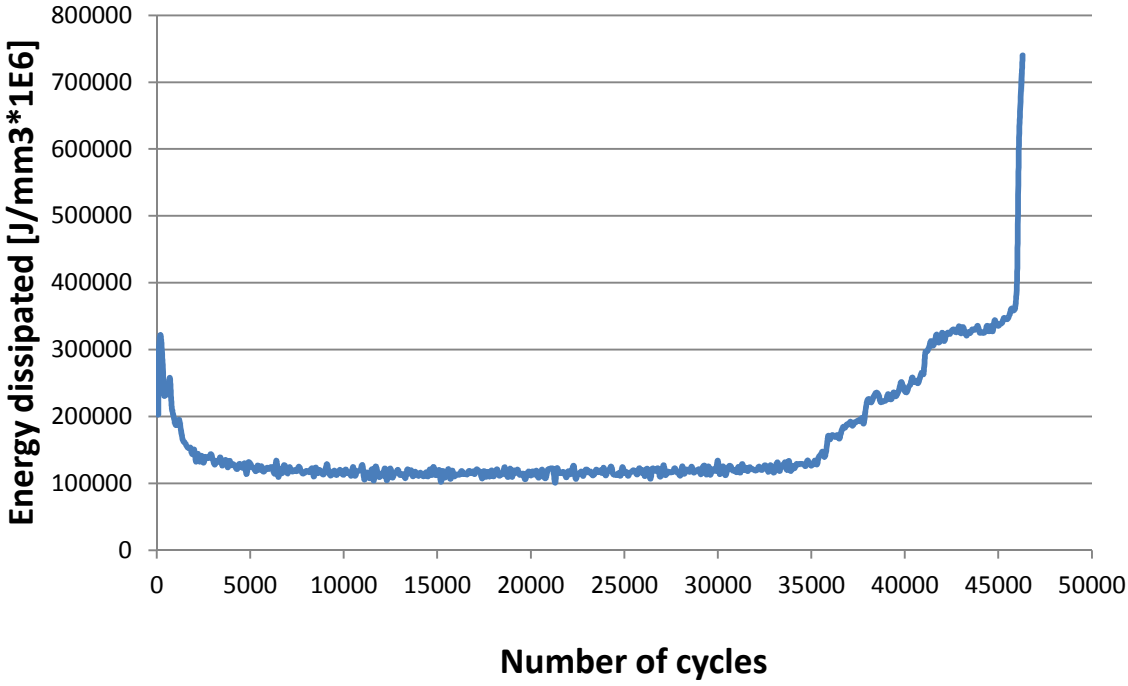

4.13 Hysteresis loop vs cycles. Frequency 5Hz, specimen n.3

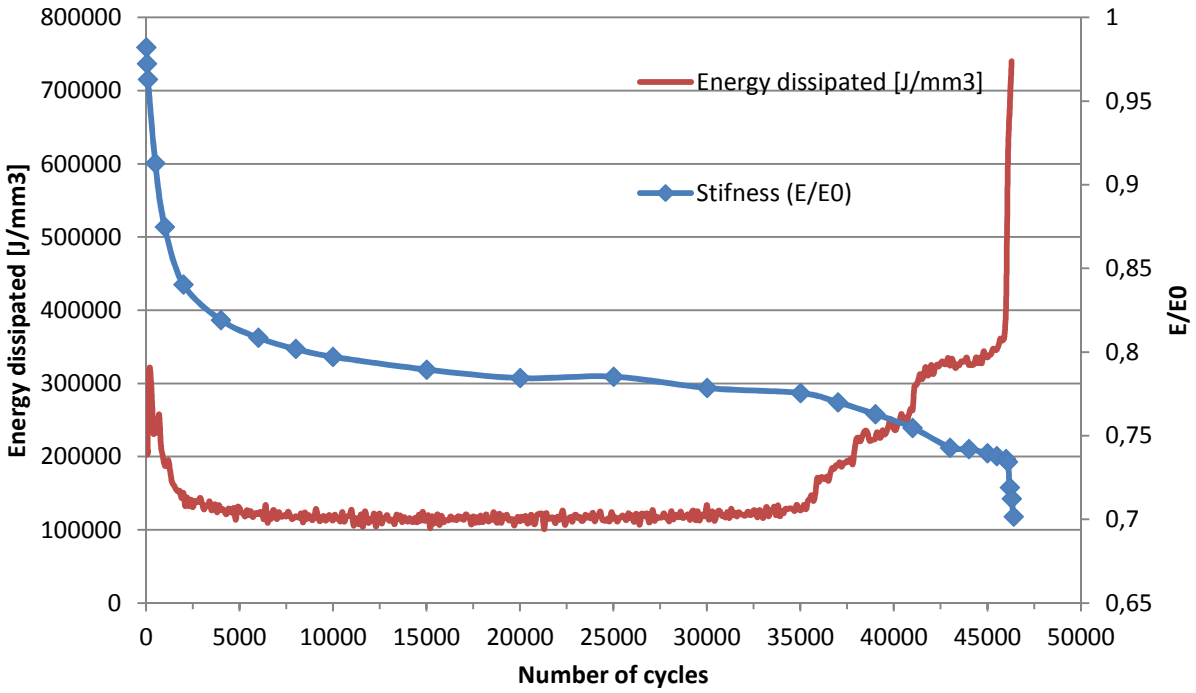

Fig 4.15 Direct comparison of hysteresis loop and stiffness reduction

From figure 3.15 it is possible to compare the trends for specimen n.3 for both the stiffness reduction and hysteresis loop changes with the number of cycles. The area within the hysteresis loop reached the plateau at approximately 7000 to 10000 cycles, while the Young's modulus followed a rapid decrease until the same number of cycle (7000 to 10000 cycles). After 1000 cycles there was a plateau for the hysteresis loop area which is associated with a slow decrease of the stiffness. Both hysteresis loop and stiffness followed this trend until about 35000 cycles where suddenly the area within the hysteresis loop increased rapidly. From that point the stiffness reduction is more severe with the increasing number of cycles. This trend persisted until about 400 cycles before the catastrophic failure, where the hysteresis loop area rises very rapidly, associated with a dramatic reduction of the stiffness.

Specimen n.4 has been tested with the same parameter a fatigue stress level of 175 MPa until final failure. The failure occurred at 90750 cycles and also for this specimen stiffness reduction and hysteresis loop were recorded analyzed (figures 3.16 and 3.17)

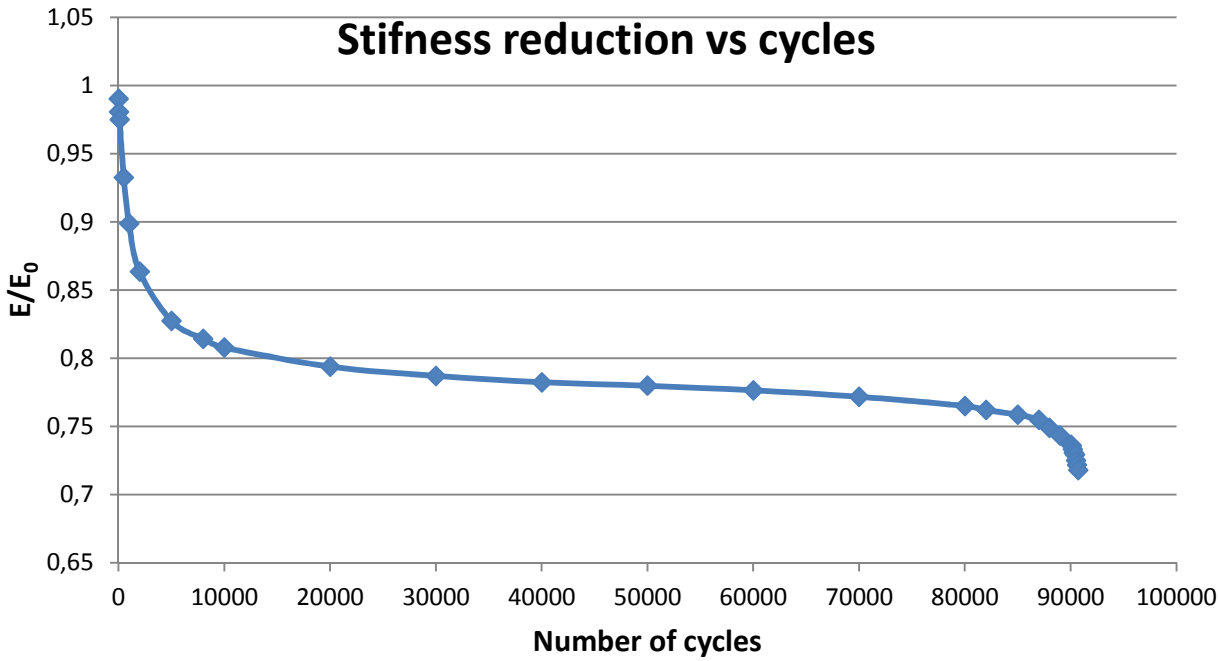

Fig 4.16 Normalized Young's modulus vs cycles. Frequency 5Hz, specimen n.4

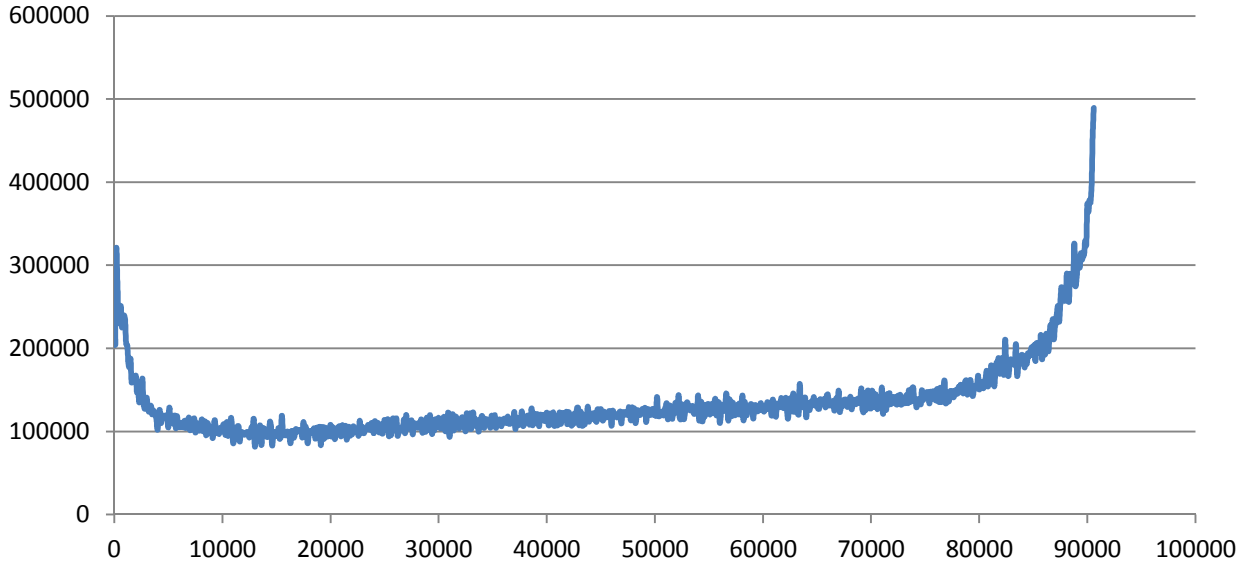

Fig 4.17 Hysteresis loop vs cycles. Frequency 5Hz, specimen n.4

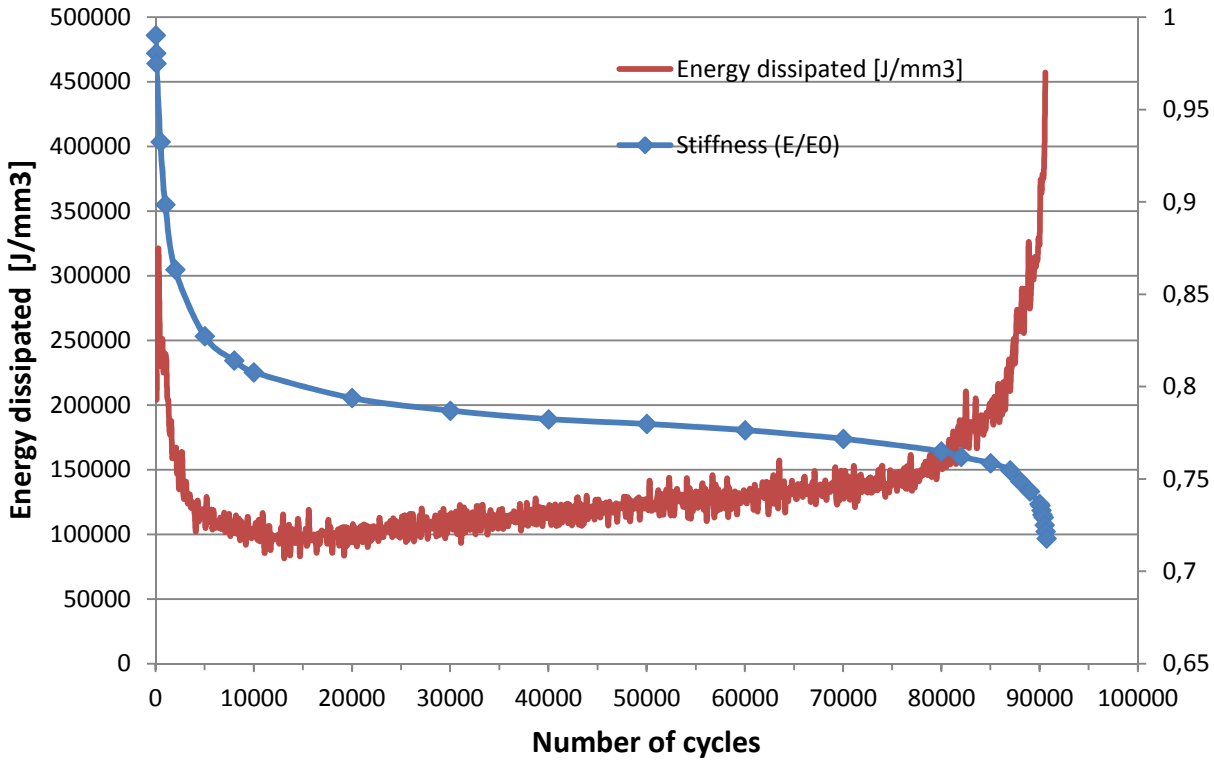

Fig 4.18 Direct comparison of hysteresis loop and stiffness reduction, specimen n.4

Fig 4.18 shows the stiffness reduction and the hysteresis loop area reported on the same graph. The profile of the two curve at early number of cycles (0 to 10000) is consistent with the profiles observe for specimens n.1, n.2 and n.3 for the stiffness reduction. However, in this case, the hysteresis loop area reached a minimum value at about 10000 and then started to increase slowly with cycling, instead of developing a stable plateau as found in specimen n.3 (fig 4.13). From about 80000 cycles, it is possible to observe a clear change in the trend of the hysteresis loop because it started to increase very quickly at the same time as the stiffness decreased rapidly until the failure occurred.

4.4.3 Tests interrupted close to failure

The two following specimens, labeled as A and B, were tested with the purpose of introducing large-scale fatigue damage, but interrupting the tests before fatigue failure., and the tests were stopped just before failure, it is believed. To determine the moment where the specimen was close to failure, two methods were used. The first was to use acoustic evidence of the specimen during the test, which was used for specimen A, while the second method, adopted in this work for the first time, was the analysis in real time of the area included within the hysteresis loop, noting that this area increases rapidly just prior to failure; this method has been used for specimen B.

The stiffness reduction and the hysteresis loop area with the number of cycles for specimen A are shown in fig 4.19 and 4.20. It is important to note that in this case a shorter gauge length of the extensometer (12,5 mm) was used, so that the gauge length did not cover the entire gauge length of the specimen and the critical damage of the final stages does not appear to have been captured, meaning that this occurred outside the extensometer gauge length. For this reason the graph of the hysteresis loop-cycles doesn't show the profile seen on specimens 3 and 4 for the late stage of the fatigue life. Anyway it has been possible to understand the crucial moment when the specimen was about to fail thanks to the noise of fiber breaks.

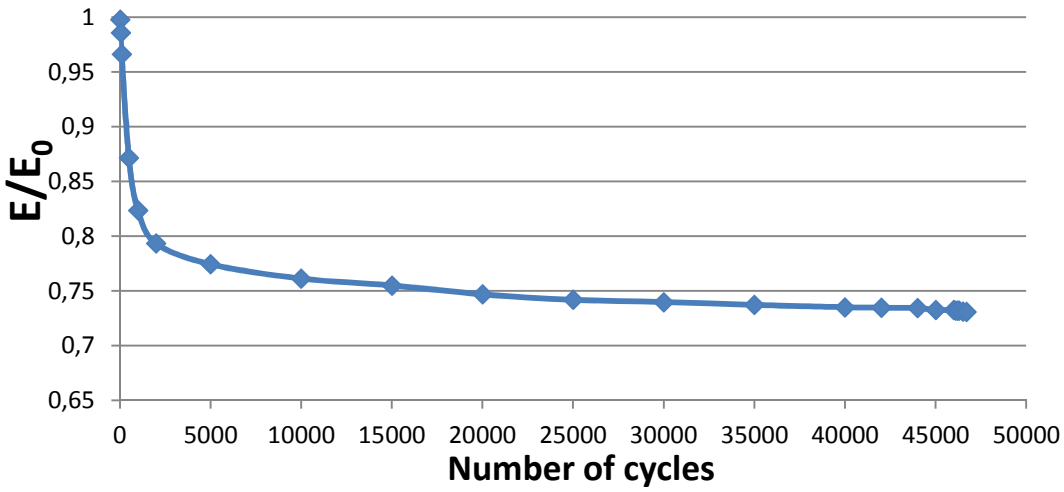

Fig 4.19 Normalized Young's modulus vs cycles. Frequency 5Hz, specimen A

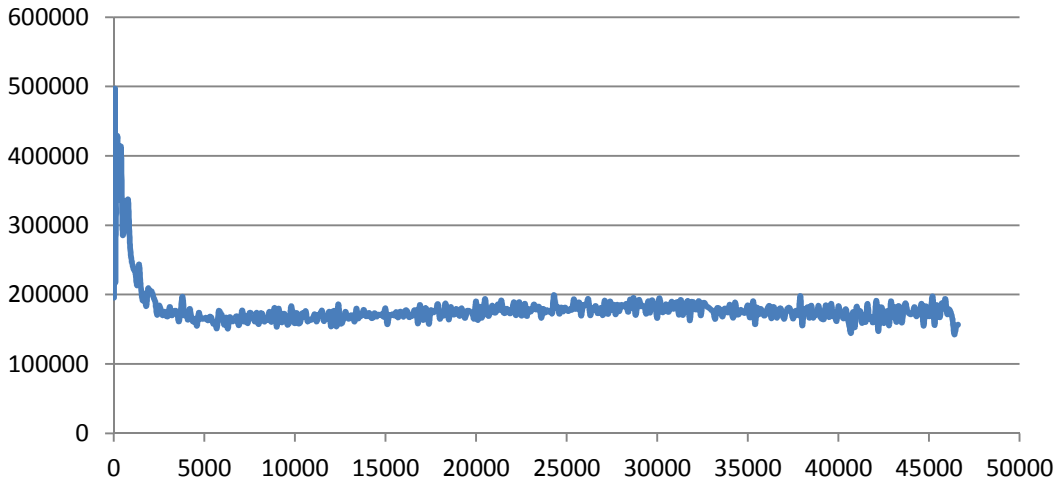

Fig 4.21 shows the trend of the hysteresis loop for specimen B. This was stopped at 94500 cycles using the value of the area included within the hysteresis loop for evaluating the level of damage introduced inside the specimen; it appears from the graph that this is beginning to rise rapidly. Taking sample 3 and 4 as a reference, it was observed that a level of 300000 J/mm-3 of energy dissipated in the hysteresis loop was a reasonable assessment that failure would occur within the next two-three hundred cycles so it was decided to stop the test at that value.

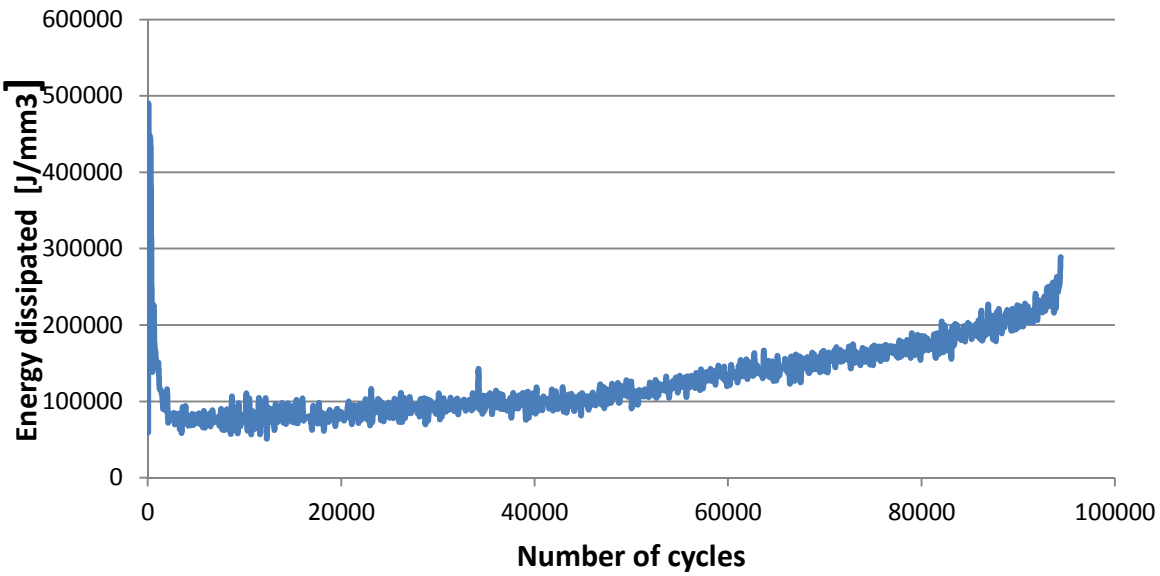

Fig 4.21 Hysteresis loop vs cycles. Frequency 5Hz specimen B

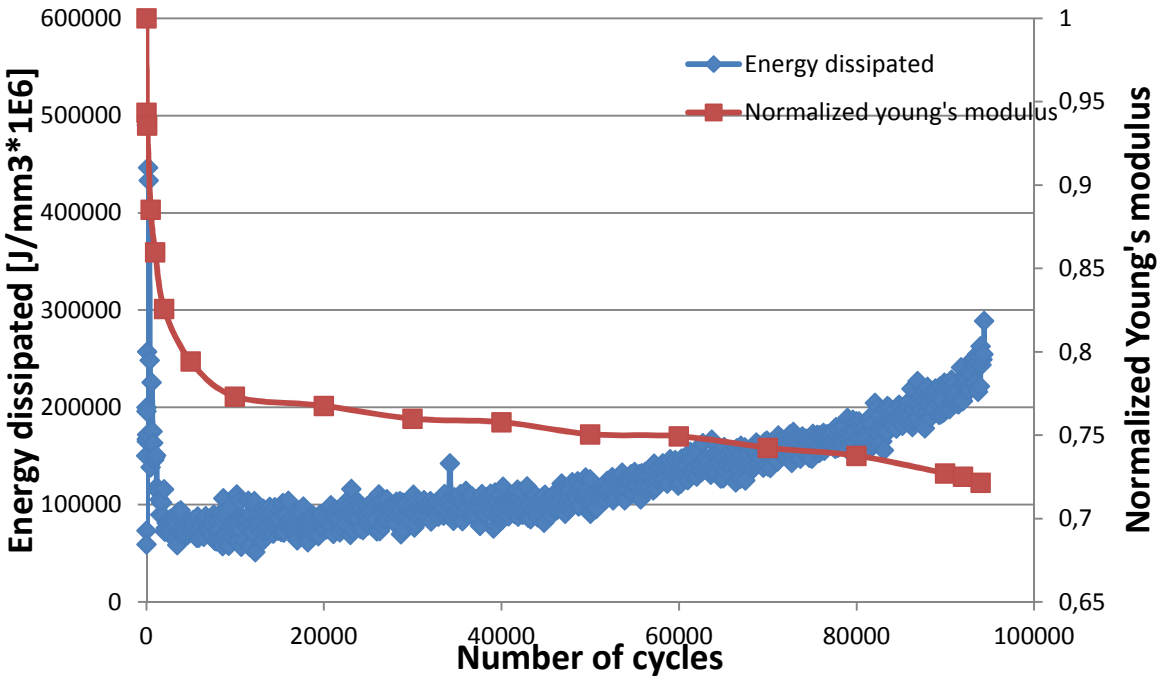

Fig 4.22 Comparison between hysteresis loop and stiffness reduction

4.5 Conclusions.

In this chapter have been shown the mechanical properties for the material object of this project and the following conclusions can be made.

1. The mechanical properties found here for the composites based on the fabric 3D-78 are the same as found in previous work. Specimens manufactured with epoxy matrix Epikote 828 fabricated using VARTM or light vacuum assisted technique appear to have very similar S-N curves, although the number of specimens tested was small.
2. Specimens 8mm wide and 25 mm wide, manufactured respectively with mild vacuum assisted impregnation and VARTM, have approximately the same fatigue S-N curve.
3. Furthermore, there is a significant difference in S-N curve for the 3D-78 (Baiocchi) and the 3D-96 (Carvelli), which also used different matrices; in general, the lifetimes were a factor of 10 smaller in the Carvelli et al work.
4. In this chapter was analyzed the change in stiffness and hysteresis loop area with the number of cycles. Four different stages were found:

a) First stage: rapid stiffness reduction and a corresponding large hysteresis loss.
b) Second stage: a low rate of stiffness reduction and a small hysteresis loss.
c) Third stage: an increase in stiffness reduction and a rapid increase of the hysteresis loss.
d) Failure stage: a very rapid increase in stiffness reduction and in hysteresis loss.

5. Damage investigation

5.1. Introduction

As explained in the previous chapters, micro computed tomography and optical microscopy have been used to characterize the damage development for the material studied in this project. The aim of the work was to understand the development of fatigue failure and the relationship between the fabric architecture and the damage that developed leading to failure for one stress level.

Optical microscopy and micro-CT combined together have shown important results which are going to be explained in this chapter. The investigation of the damage development in fatigue has been achieved by testing specimens and interrupting the tests before catastrophic failure because a failure could introduce a shock wave that creates additional damage which is not the real damage caused by the cyclic loading. For this reason, tests were performed until the specimens showed evidence of an impending failure.

The determination of the impending failure was achieved with two methods: the first and easier way to notice an increase in audible acoustic emission made by the specimen which was about to fail; the second method was to use the hysteresis loop to provide an indication of the approach to fatigue failure.

Two specimens, A and B, were analyzed in this way, with extensive use of micro-CT analysis and optical microscopy to investigate the damage.

5.2 Damage accumulation observations in specimen A

Specimen A, which was 8 mm in width and manufactured using the low vacuum assisted method, was cycled with a peak stress of 175 MPa, R=0,1, for 46740 cycles. As the S-N curve for the specimens shows, the expected number of cycles to failure at this stress level is between 50,000 and 100,000.

Microstructural observations of damage were performed on the area where was clear evidence of extensive damage. For this specimen, a short gauge length extensometer had been used (12,5mm) and the damaged area investigated was outside the gauge length. The damaged area which has been investigated scanned is shown in figures 5.1a and 5.1b

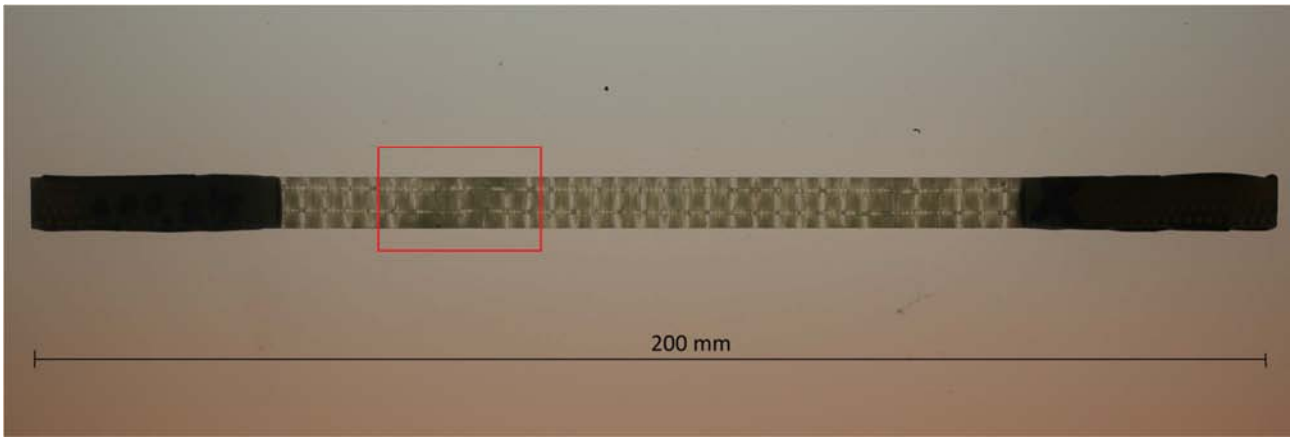

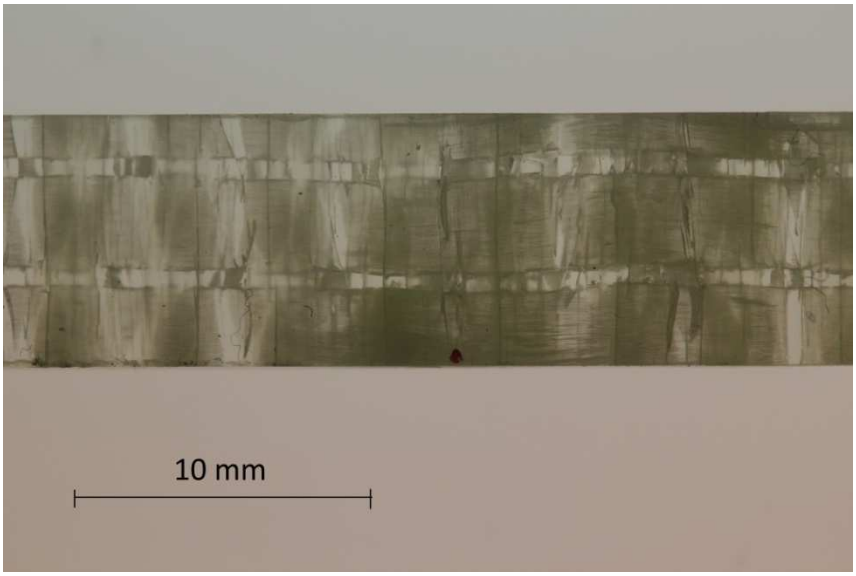

Figure 5.1 (a) Low magnification image of specimen A; (b) higher magnification image of the area investigated in detail.

In the schematic of the 3D architecture shown in Figure 5.2, the z-tows are shown as orthogonal sections of yarns, which is not correct, as they are sinusoidal in reality. Nonetheless, the schematic provides a good indication of the structure. Every cross-section investigated was either in the "XZ" or "YZ" planes. The unit cell contains two warp

tows in the “X” direction, three weft tows running in the “Y” direction in three different “XY” planes, and two Z-tows in the z-direction.

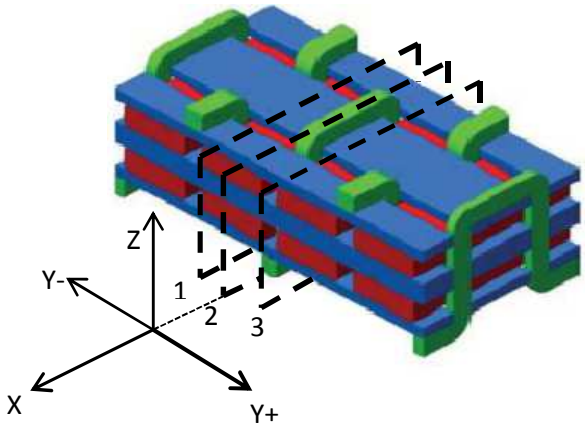

Figure 5.2 Schematic of the 3D architecture

A micro-CT image of the section labeled as “1” in figure 5.2 is shown in Figure 5.3. If the plane of the z-tow is taken as Y = 0, then this plane is Y-negative. It is possible to observe the presence of fiber fractures in the warp tow: these fractures are located towards the edge of the warp tow which is close to the Z-tow. In addition, the fiber fractures are located approximately at the maximum thickness of the surface weft tow The proximity of the z-tow is underlined by the gap between the surface weft tow and the specimen surface. The fiber fractures extend across almost all the complete thickness of the warp tow. Interestingly, no fiber fractures were found within the parallel section of the second warp tow.

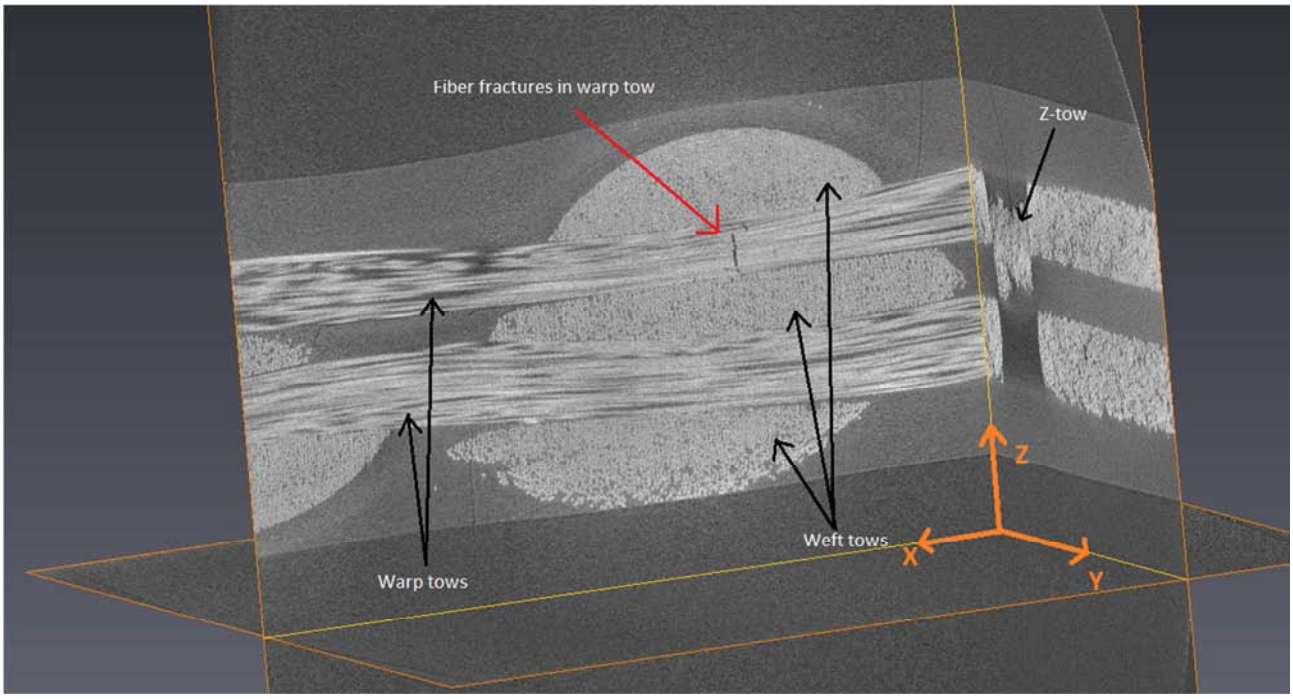

Figure 4.3 Observation of tow fractures in plane “1”, which is Y-negative with respect to the plane of the z-tow (Y = 0).

Figure 5.4 shows another section located in the same plane at almost the same location, but 0,5 mm closer to the z-tow. In this picture it is possible to see again fiber fractures, although now the fractures are a little more dispersed.

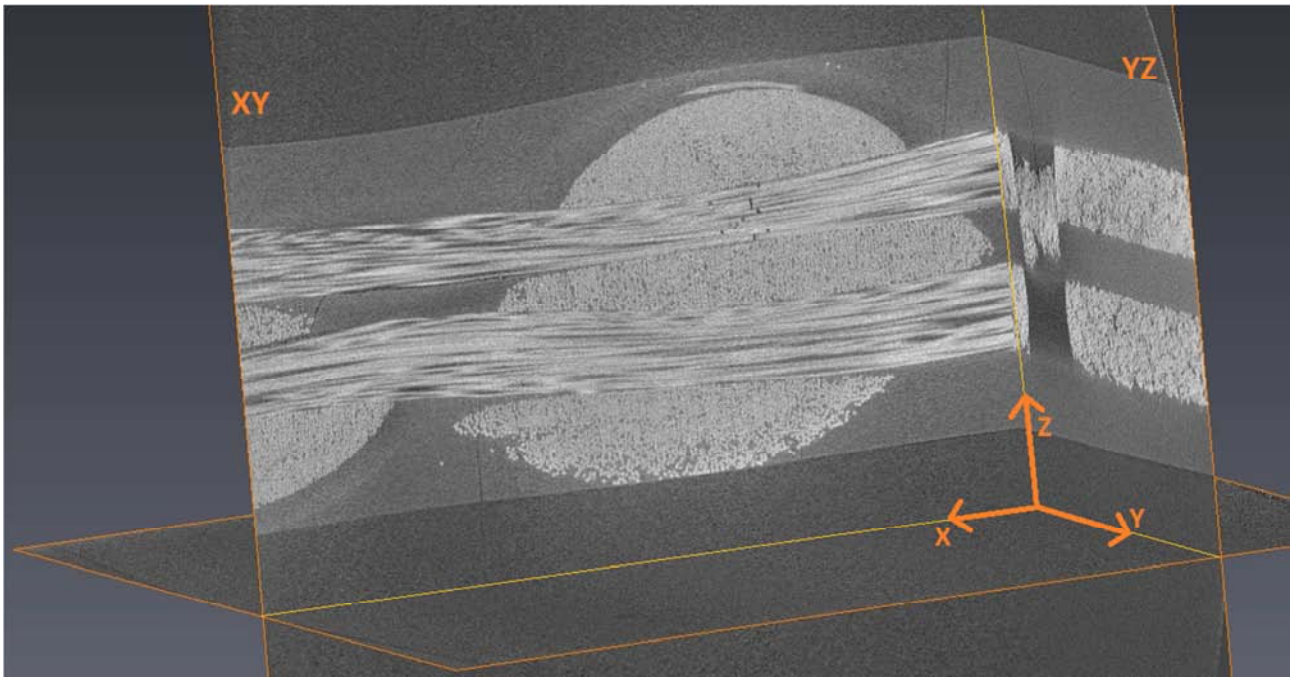

Figure 5.4. An image taken very close to the plane of Figure 5.3, but 0,5 mm closer the plane of the z-tow.

In figure 5.5 a view of the “XY” plane at the same location where it is possible to see fiber fractures extended on both warp tows running each side of a z-tow. It can be seen that the fractures in each tow are approximately aligned on the same plane. At a higher magnification, (Figure 5.6) the presence of two matrix cracks within the resin pocket region can be seen, with each crack located on the same plane as the fiber fractures in an adjacent tow. At this magnification, the microCT image of the matrix cracks is not completely clear, however.

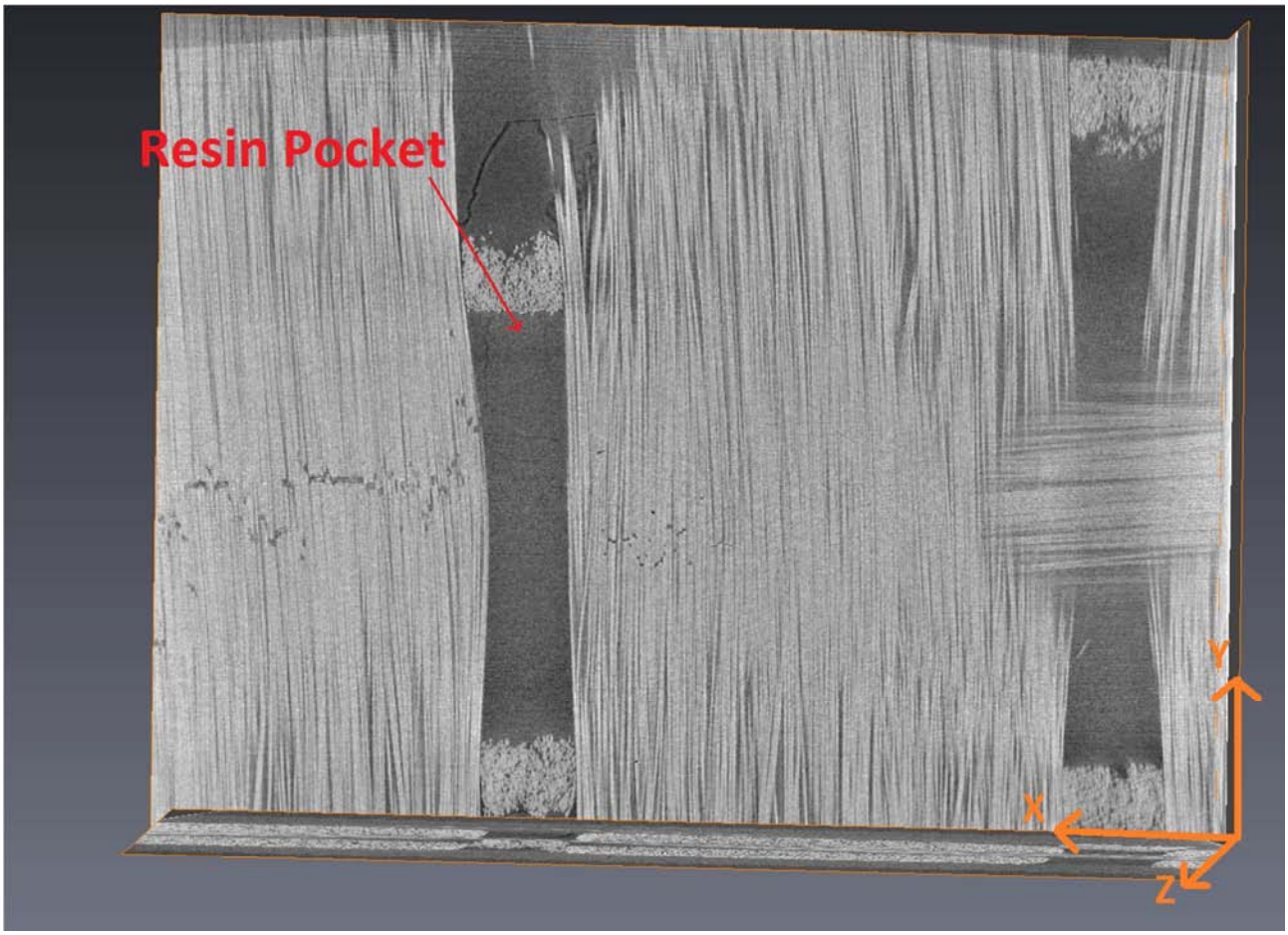

Figure 5.5 An image taken in the “XY” plane at the same location, showing fiber fractures within the two warp tows either side of a z-tow.

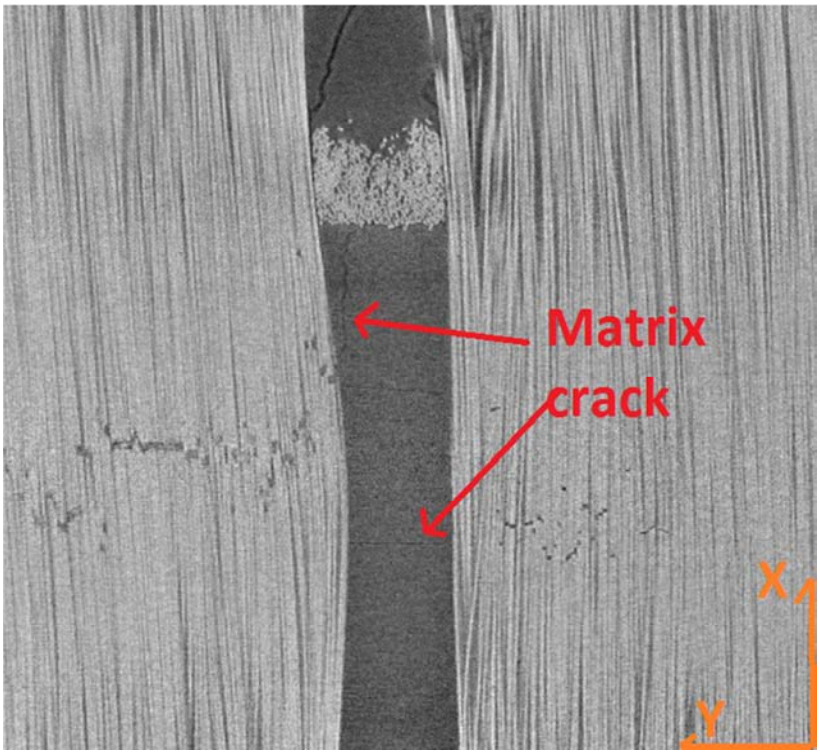

Figure 5.6 Matrix cracks adjacent to warp tow fiber fractures in the resin pocket region

Optical microscopy is useful in understanding the general features of the planes being investigated. Figure 5.7 (a) and (b) show the aspect of the material in the section labeled as "1'" analyzed with the optical microscope. It is possible to observe the distribution of the warp and the weft tows. This picture shows the overall damage included in the specimen, which in this plane clearly shows matrix cracks in the weft tows within each layer and matrix cracks in the resin pockets between the weft tows. Figure 5.8 shows a further magnification of the optical image, showing the tow fracture seen in Figures 5.3 and 5.4.

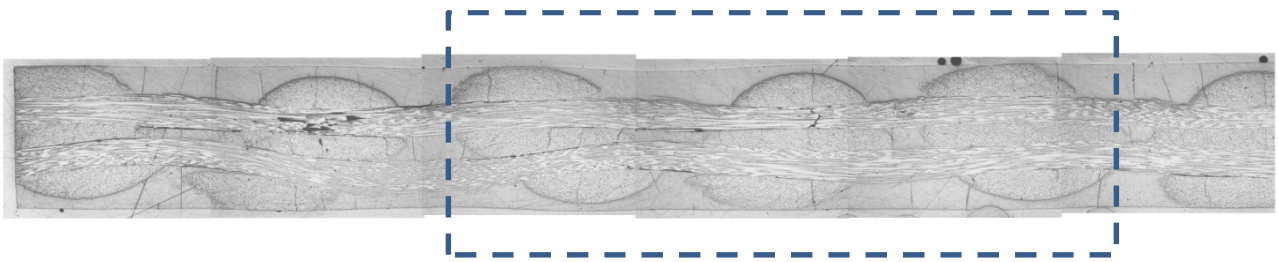

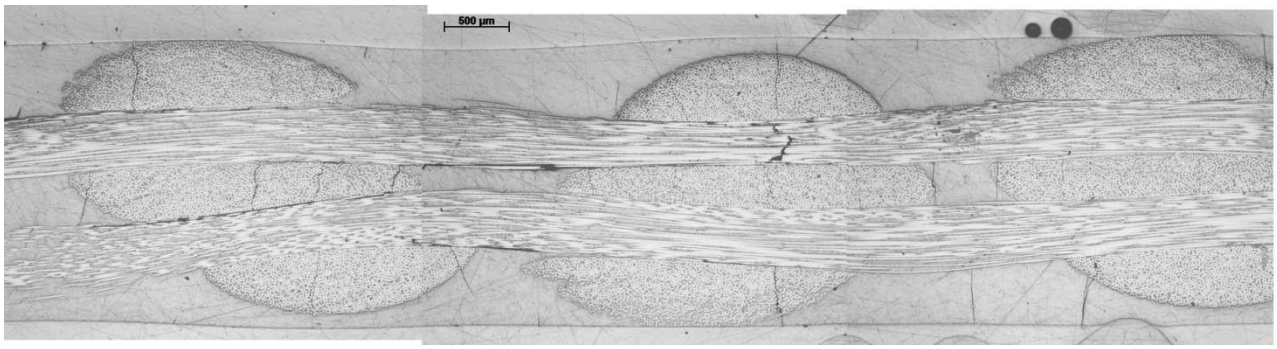

(b)

Figure 5.7 An optical microscopy image of the "1" plane at (a) low) and (b) higher magnification. The tow fractures seen in image (b) are at the same location as in the microCT images of Figure 5.3 to 5.6.

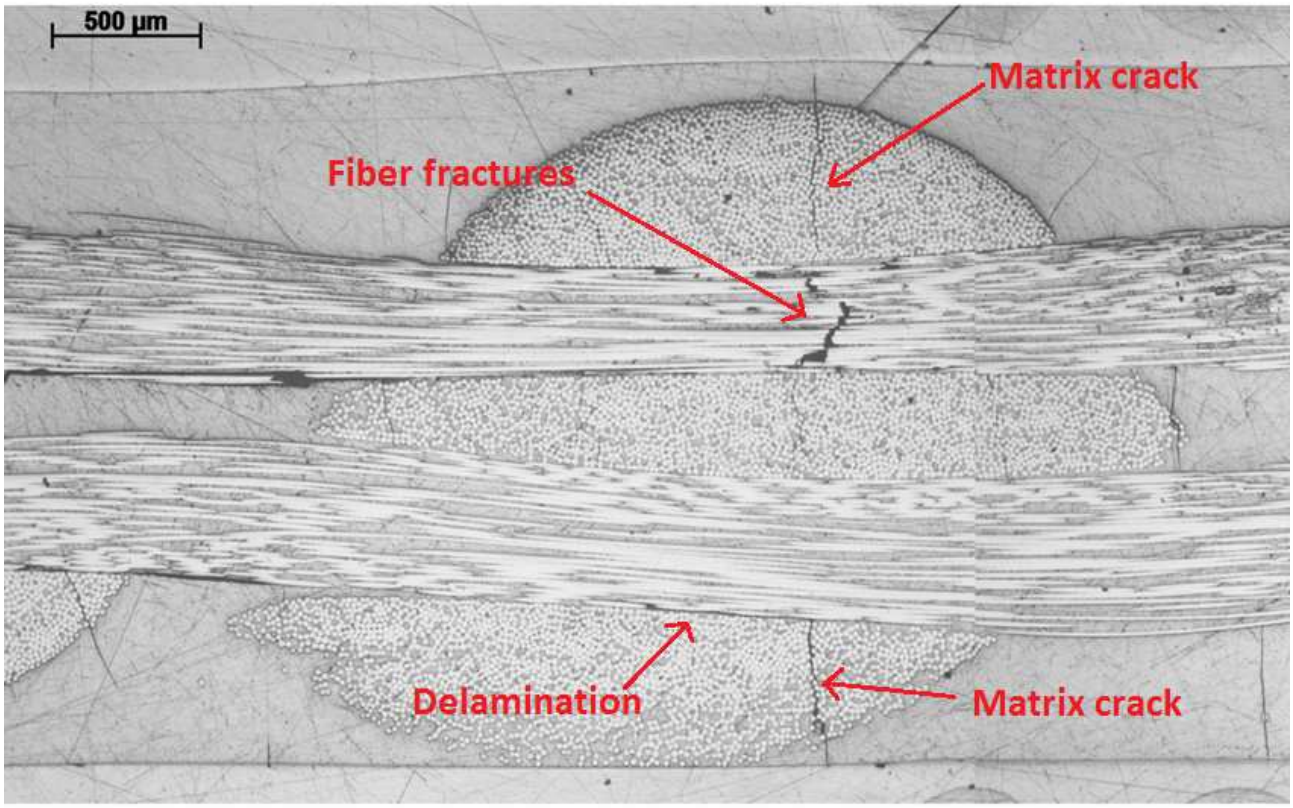

Figure 5.8 Optical micrograph of the tow fracture seen in Figures 4.3 and 4.4.

Figure 5.8 shows particularly important features of the damage seen in this plane. These consist of matrix cracks in the weft tows, an accumulation of fiber fractures in the warp

tow, and a delamination associated with a weft tow matrix crack. The most important feature is, again, the fiber fractures in the warp tow, but in addition to this it is possible to observe a matrix crack adjacent to the fiber fracture in the upper weft tow. It appears that the matrix crack is immediately adjacent to the warp tow fiber fractures. Figure 5.9 shows higher magnification images of the same tow

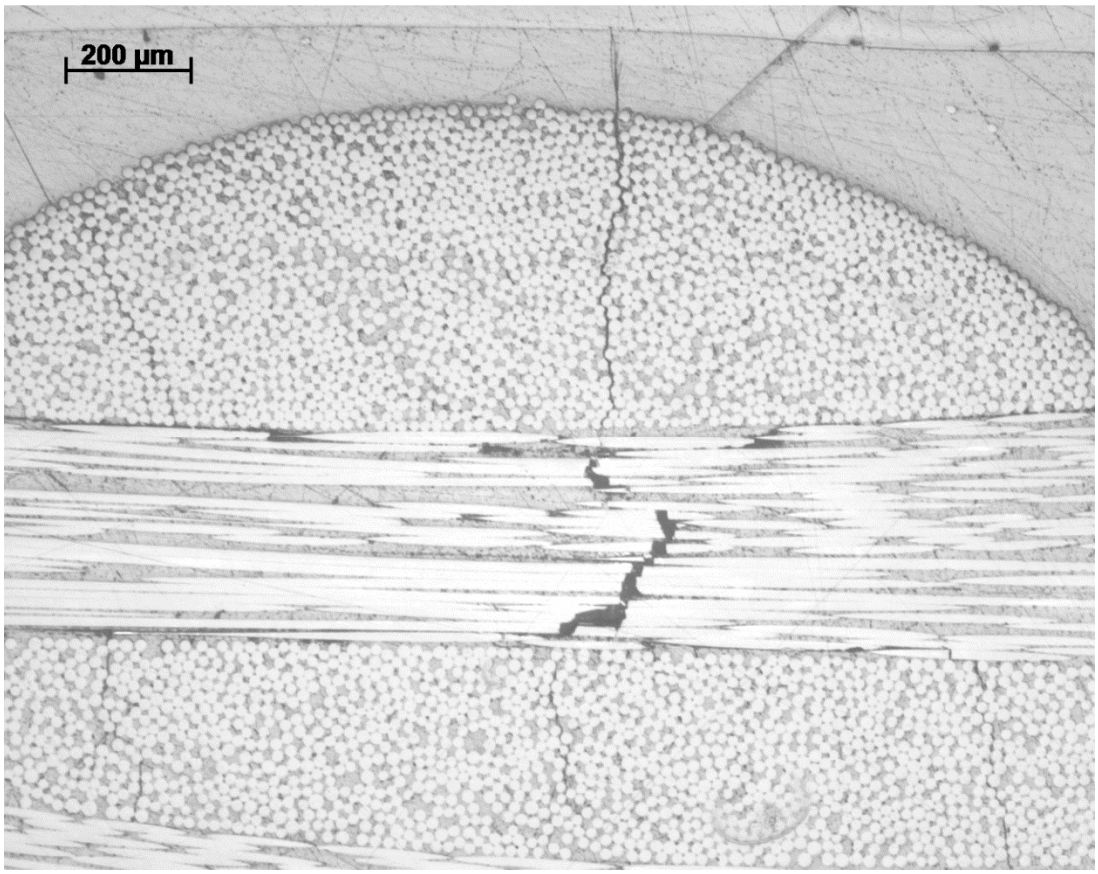

5.9(a)

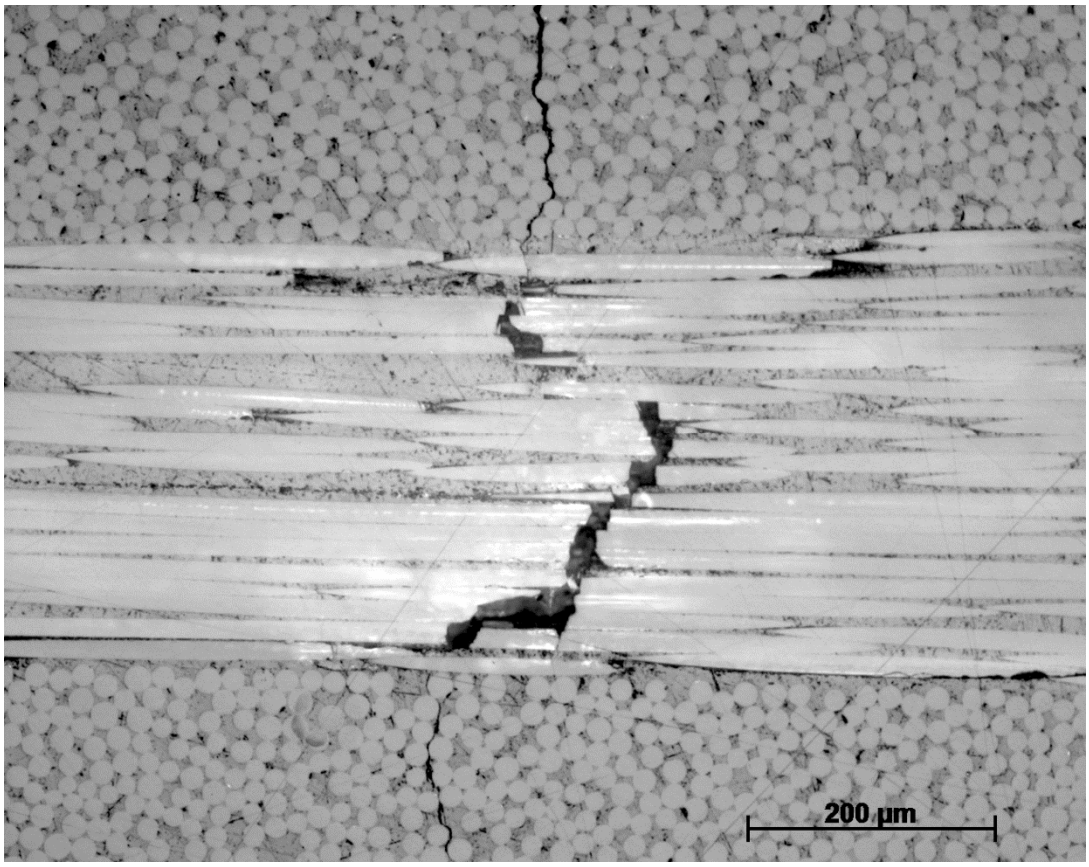

5.9(b)

Figure 5.9 Higher magnification images of the tow fracture

An optical microscopy image of the plane of the z-tow (i.e plane “2”, or where Y = 0) is shown in Figure 5.10. This section shows the sinusoidal shape of the z-tow and the weft tows. In this plane, the warp tows cannot be seen, so evidence of the warp tows towards the left of this image shows that either the warp tows were not straight or that the plane of the image is not exactly at Y = 0. This image has been formed by stitching together seven individual images.

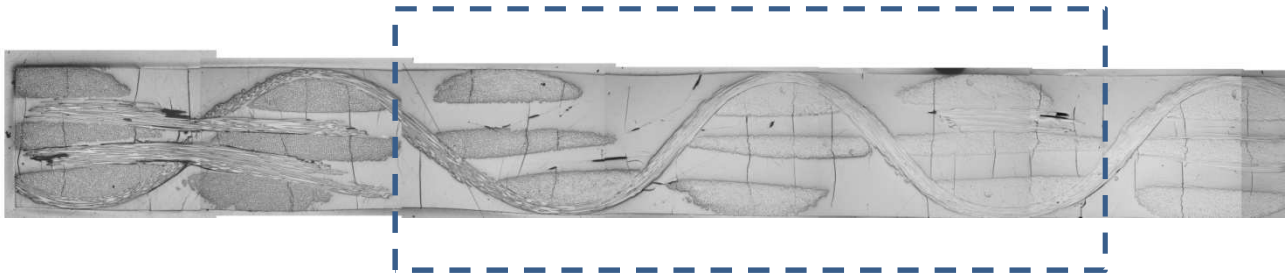

Figure 5.10 Optrical micrograph in the plane of the z-tow (i.e. plane “2”, or where Y = 0)

Figures 5.11 and 5.12 show magnified images of the dashed rectangular marking of figure 5.10

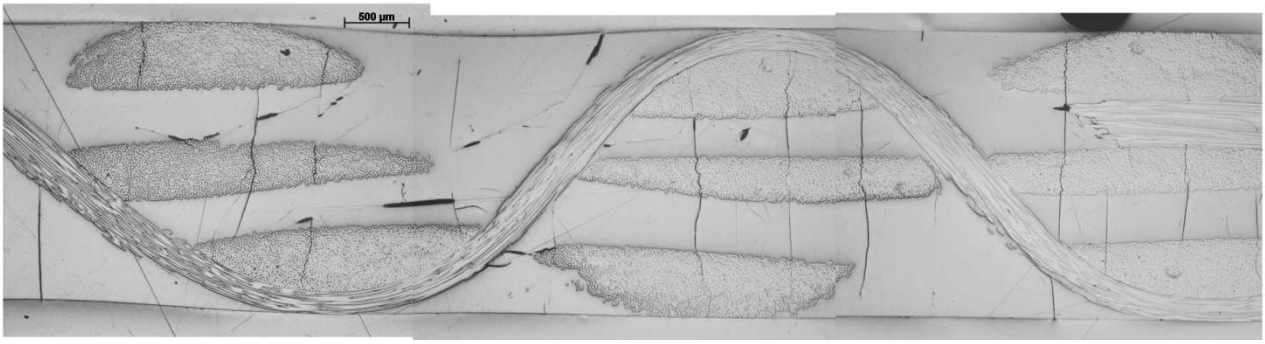

Figure 5.11 Higher magnification image of the plane of the z-tow.

It would appear that there are matrix cracks which extend significant distances across the thickness of the specimen. Of particular interest are the matrix cracks in the weft tows which continue across the resin pocket, across the next weft tow and resin pocket, and into the third and final weft tow. Figure 5.12 shows the extension of a weft tow matrix crack into the adjacent resin pocket. These resin pockets, which are formed in the gap caused by the position of the z-tow, run either side of the warp tows. Hence, the fibers within a warp tow are subjected at the surface of the warp tow to the influence of two types of matrix cracks, with both types of matrix cracks in the YZ plane: weft-tow matrix

cracks terminate at the on the XY plane of the warp tow; resin pocket matrix cracks terminate on the XZ plane of the warp tow. Figure 5.13 shows the correspondence in the physical location of these three types of damage.

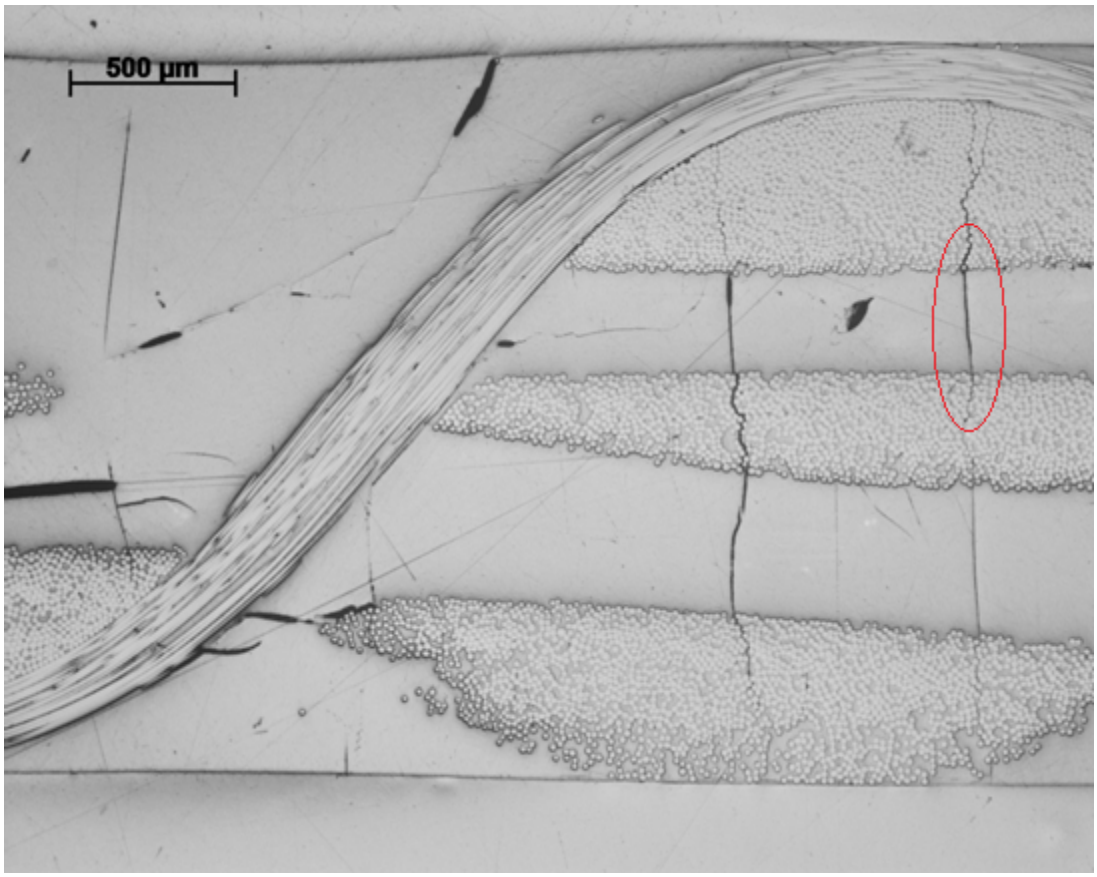

Figure 5.12 Higher magnification image of z-tow plane, with weft tow and an associated resin pocket matrix crack, shown with a highlighted ellipse.

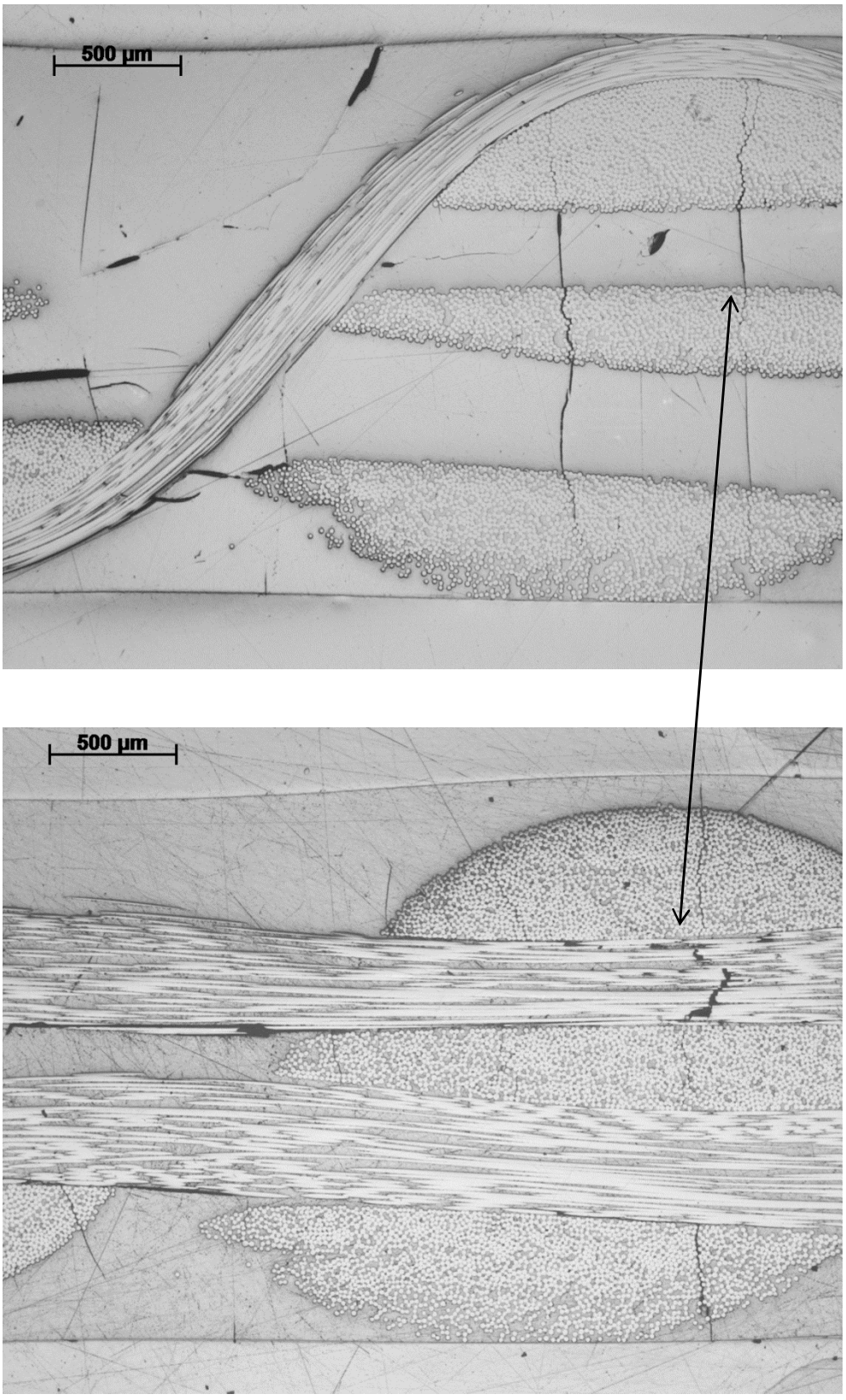

Figure 5.13 Correspondence between weft tow matrix cracks, resin pocket matrix cracks and fiber fractures in the warp tow

The width of the region of matrix (i.e. the resin pocket) which separates two warp tows is about 0,5 mm and as shown in the previous figures it is a zone where matrix crack can easily develop. Since fiber fractures and matrix crack are located in the same plane it is possible to assume that fiber fractures are related to the presence of these matrix cracks. The micro-CT analysis evidenced the presence of fiber fracture especially in the region of the warp tow closer to the z-tow, which is also closer to the resin pocket (see Figure 5.5).

5.3 Damage accumulation observations in specimen B

Specimen B was cycled at a peak stress of 175 MPa and the cycling was stopped after 95560 cycles. The test was stopped close to its final catastrophic failure by monitoring in real time the change in the area of the hysteresis loops. The monitoring control of the damage has been possible by using a gauge length of the extensometer of 96 mm instead of a shorter one. The specimens and the damaged area which has been investigated in detail scanned are shown in Figure 5.14.

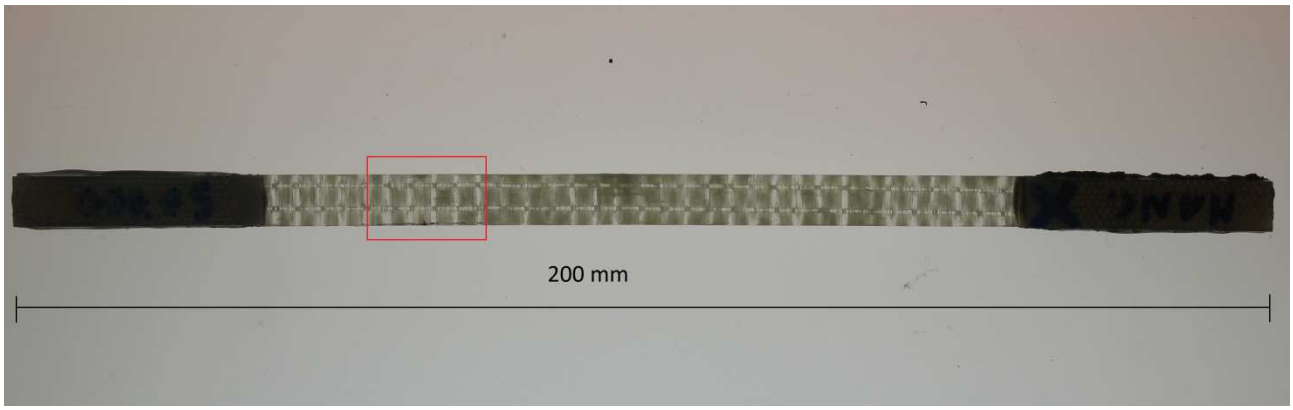

5.14(a)

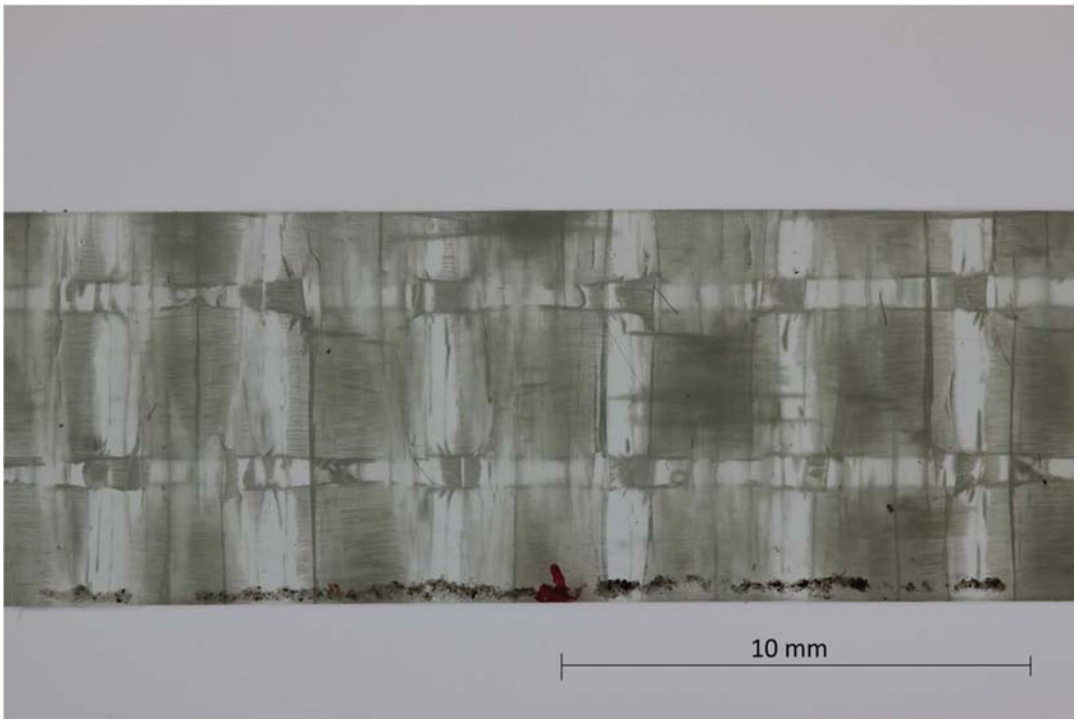

5.14(b)

Figure 5.14 Low magnification images of Specimen B; the test was stopped after 95560 cycles

The same approach conducted with the specimen A has been followed with the second specimen labeled “Specimen B”. The direction reference explained in Figure 5.2 is also used in this analysis. The plane labeled as “1’” corresponds to an XZ plane which is behind the plane of the Z-tow (i.e. it is Y-negative, where Y = 0 is the plane of the Z-tow). Figure 5.15 shows the intersection of this plane with the YZ plane. Again, fiber fractures were found located in the warp tow close to the Z-crown (i.e. where the Z-tow loops over an outer weft tow). As found in sample A, the fiber fractures are positioned just in the middle of the length, adjacent to the location of the maximum thickness of the outer weft tow.

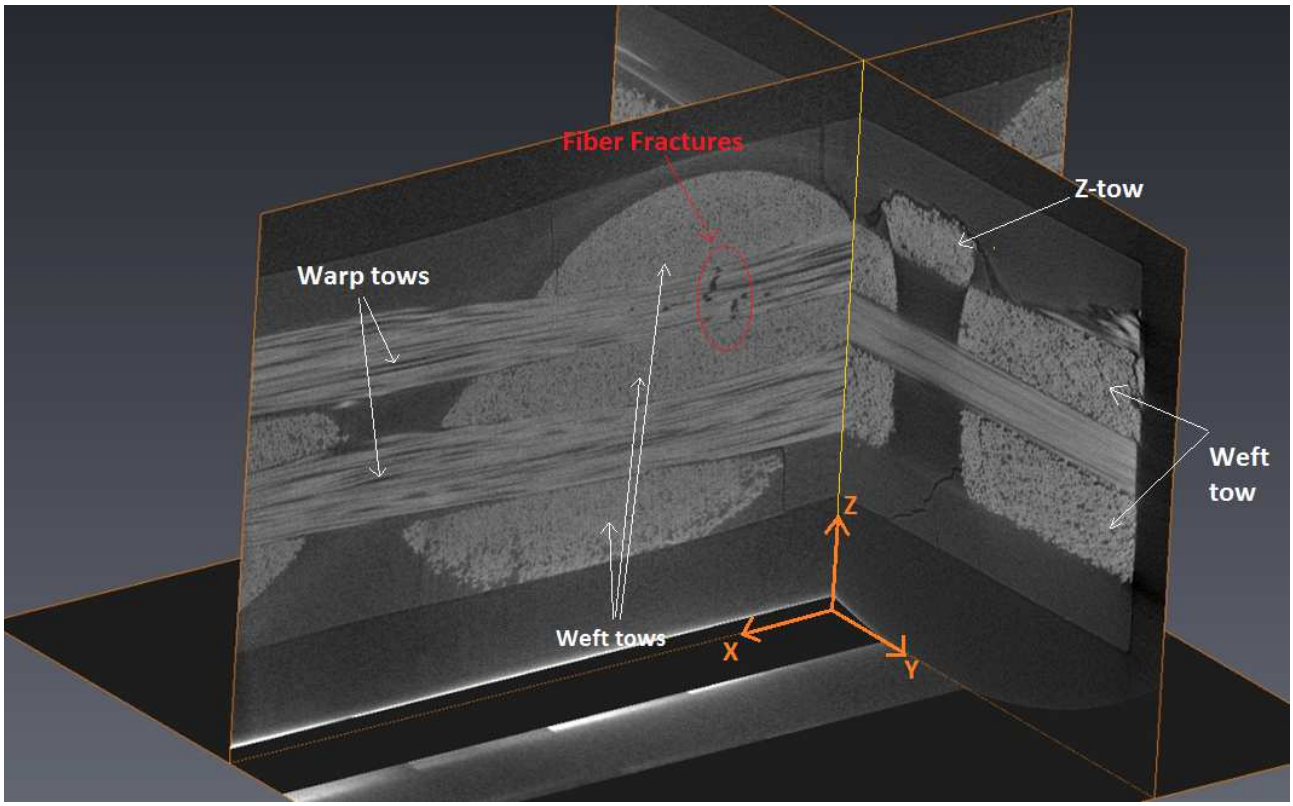

Figure 5.15 Intersection of the XZ and YZ planes at a location just behind the z-tow (i.e. Y-negative, where Y = 0 is the plane of the Z-tow).

Figure 5.16 shows another section located in position “1’”(plane XZ) but moved 0,2 mm closer to the z-tow. In this picture it is possible to see again fiber fractures which have migrated a little along the warp tow. In this image, the edge of the z-tow can just be seen looping over the outer weft tow.

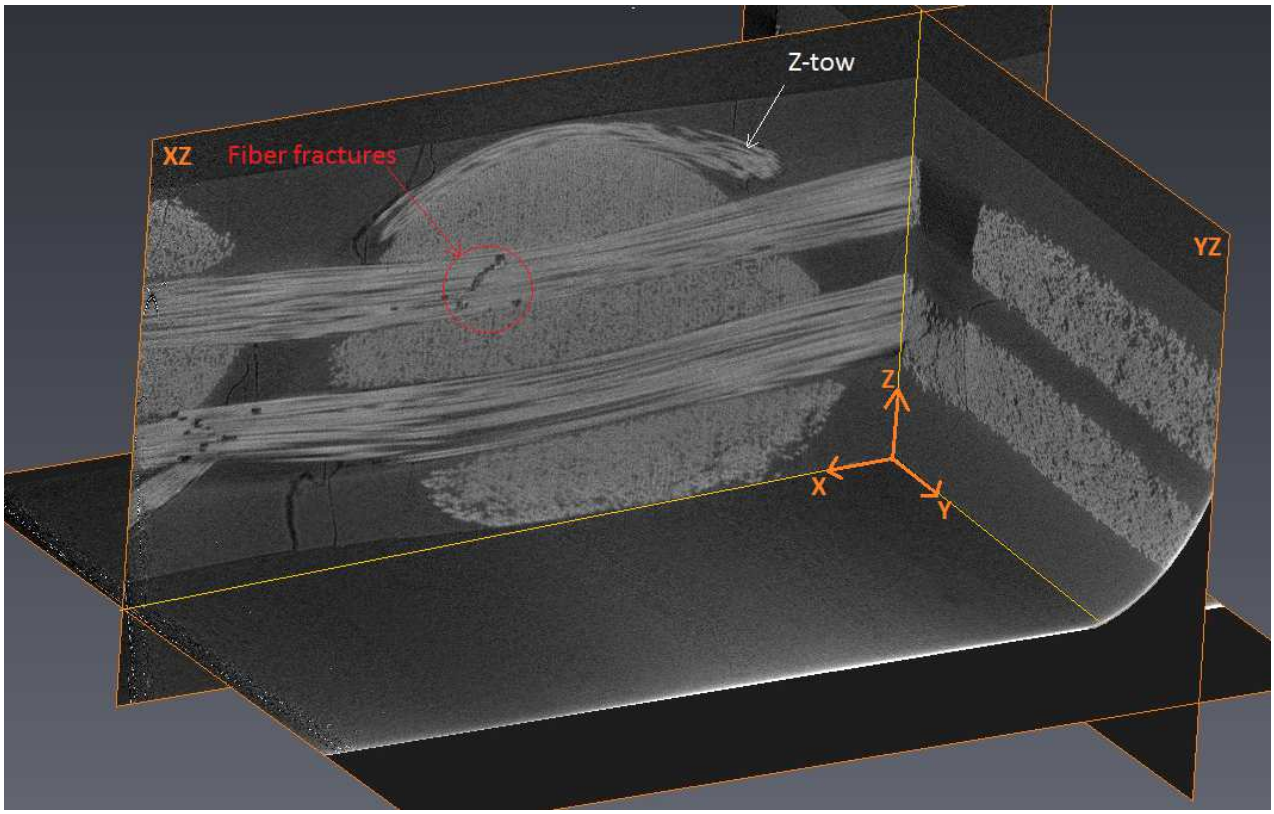

Figure 5.16. Intersection of the XZ and YZ planes at a location almost at the edge of the warp tows, immediately adjacent to the z-tow.

In Figure 5.17 three orthogonal plane are connected together to show the presence of fiber fractures within the warp tow, located near the resin pocket and extending across the warp tow.

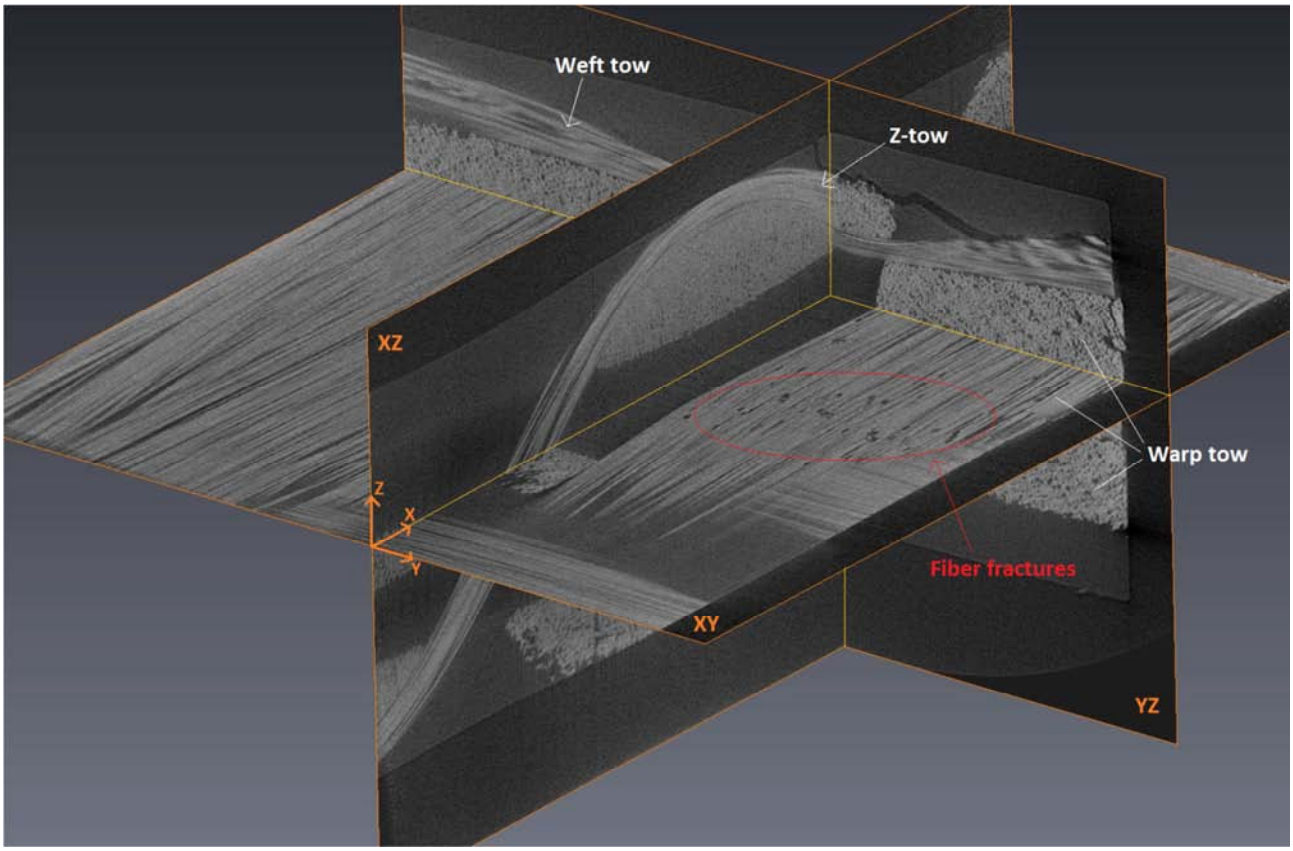

Figure 5.17 Warp tow fractures in a tow adjacent to a resin pocket

In specimens A and B, the location of the warp tow fractures have been within the section of warp tows closest to the Z-crowns (which is the location where the z-tow loops over an outer weft tow). On the other hand, warp tow fractures in the section of warp tow in the other half of the specimen have been almost never observed. Evidence for the difference in damage accumulation for these two locations is shown in Figures 5.18 and 5.19. The evidence is clearly visible in Figure 5.18 and Figure 5.19. There are numerous fiber fractures in the warp tows close to the z-crowns (Figure 5.18), but no fiber fractures in the tows further from the z-crowns (Figure 5.19).

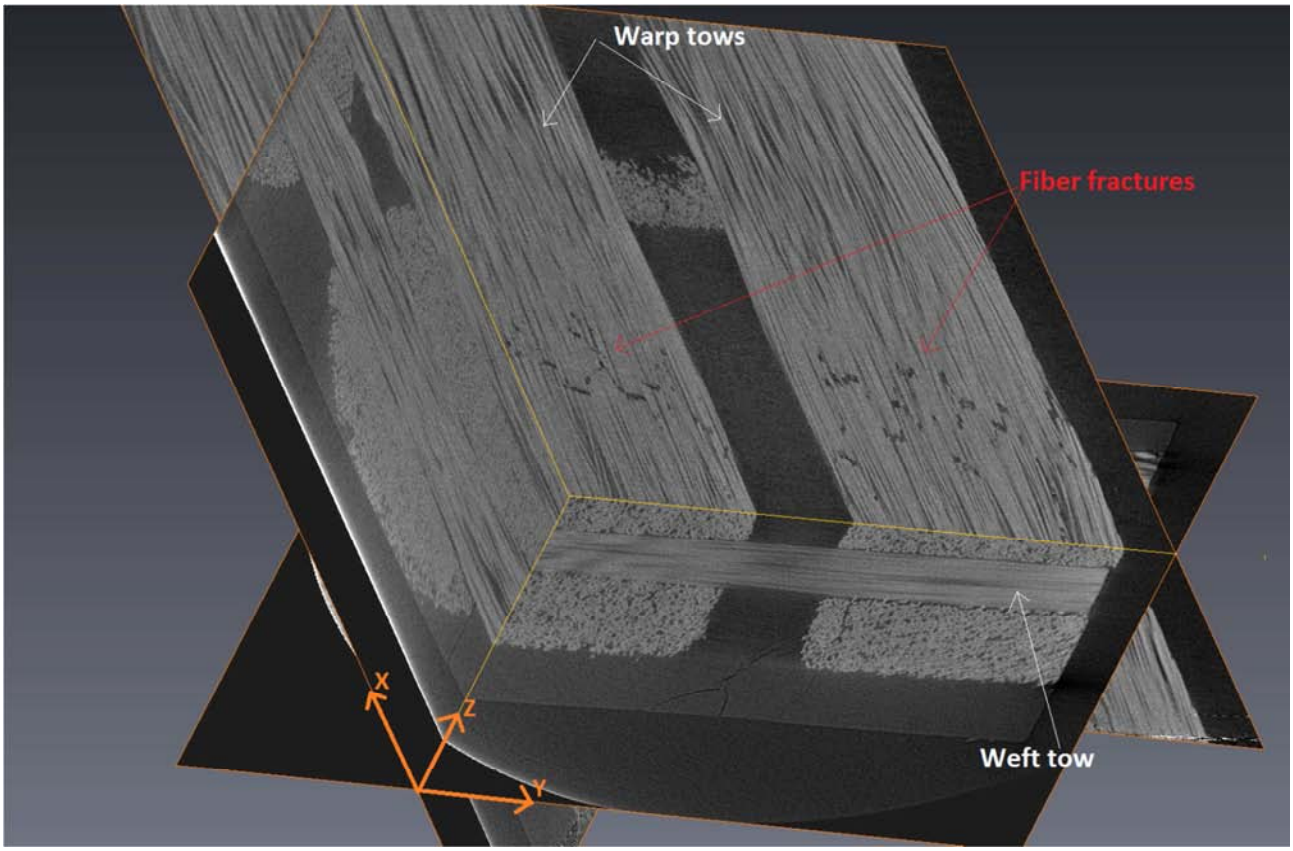

Figure 5.18 Warp tow fractures in two warp twos adjacent to a resin pocket: the warp tows here are close to the Z-crown, where the z-tow loops over an outer weft tow.

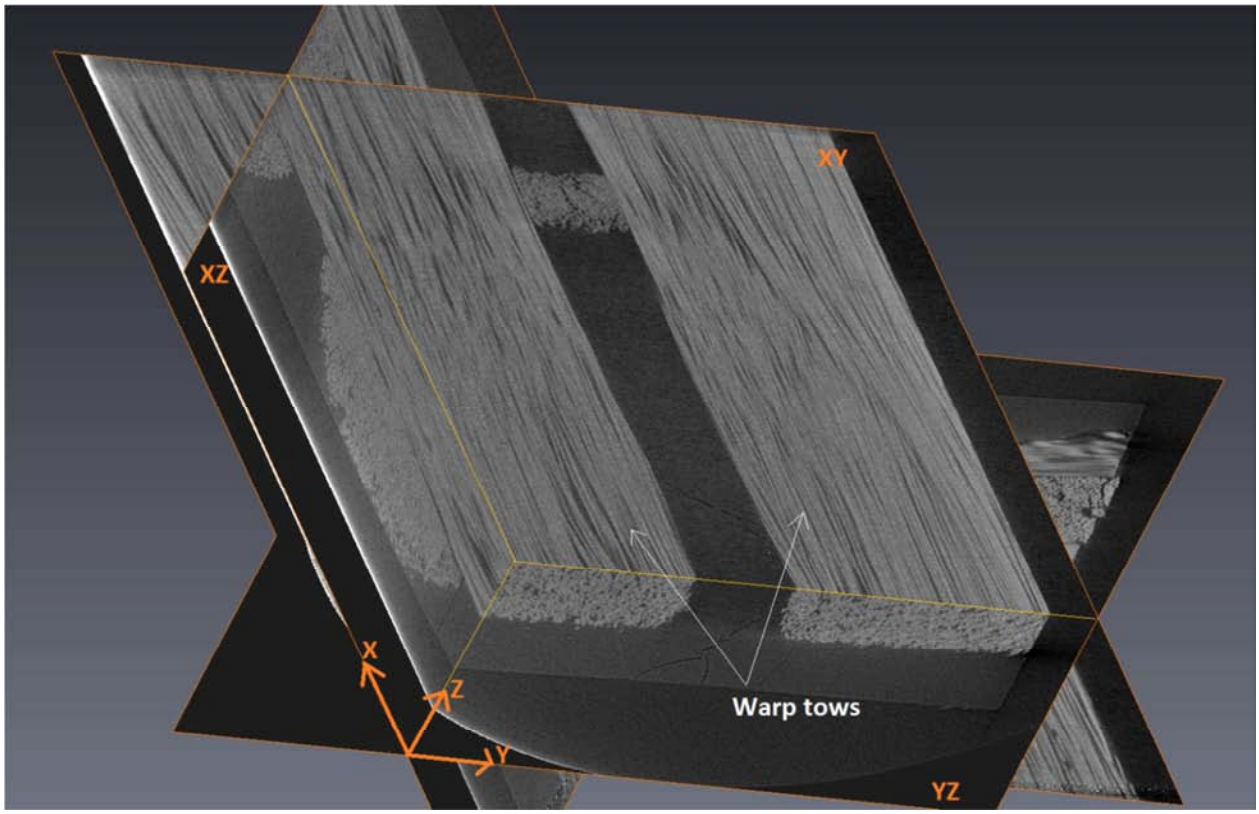

Figure 5.19 Absence of warp tow fractures in two warp tows adjacent to a resin pocket: here, the warp tows here are on the opposite side of the specimen to the Z-crown.

Further investigations of Specimen B have been carried out with the optical microscope as done with specimen A. Figure 5.20 shows a section of the material cross-section labeled "1". This presents the "XZ" plane where it's possible to view the the shape and the distribution of the warp and the weft tow. As for specimen A, this section is going to be used as comparison in order to understand a possible relationship between matrix cracks and fiber fractures

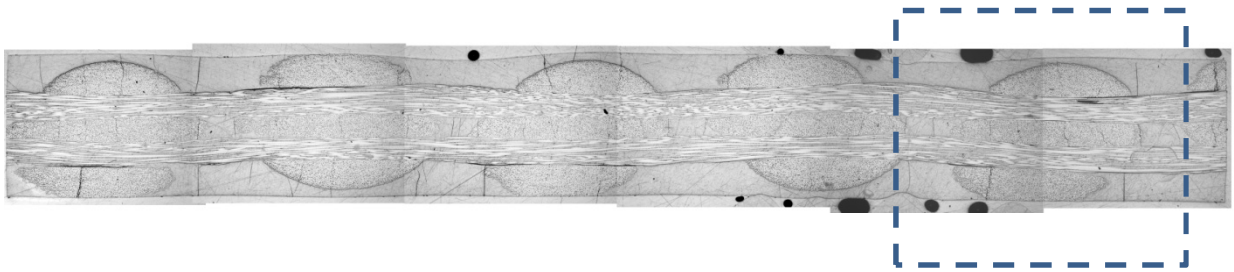

Figure 5.20 Specimen B: optical micrograph of cross-section "1"

A magnification of the blue dashed rectangular marking is shown in Figure 5.21, where it is possible to see fiber fractures of the warp tow which is just under the weft tow closest to the z-crown. The position of the fractures is the same that was observed in the analysis of the specimen A: fractures in the fiber forming the warp tow are approximately in the middle of the width of the weft tows. Fiber fractures are highlighted within the red ellipse.

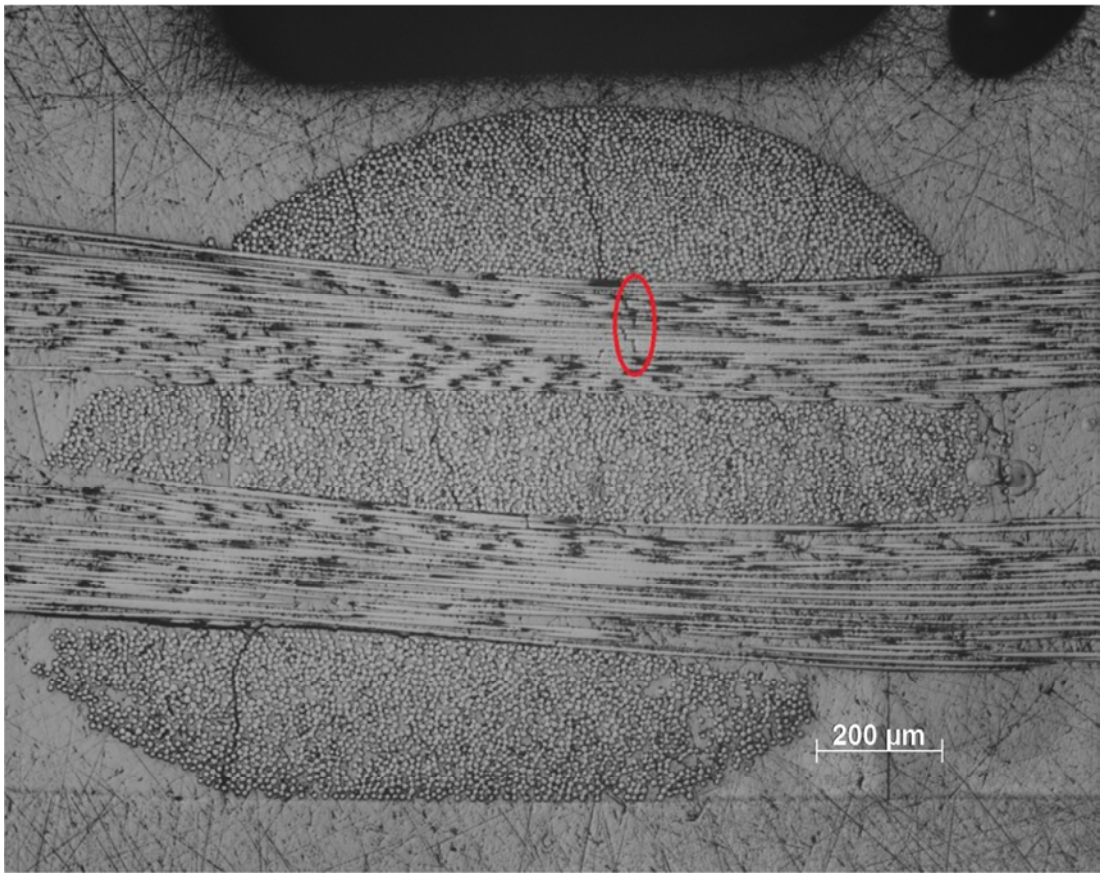

Figure 5.21 Fiber fracture in the warp tow

In figure 5.22 is shown a section of the material labeled “2”, which is the plane of the z-tow; consequently, the warp tows cannot be seen. Again, this section presents the sinusoidal shape and the distribution of the z-tow, the location of the weft tows, and the extensive matrix cracking, as noted previously.

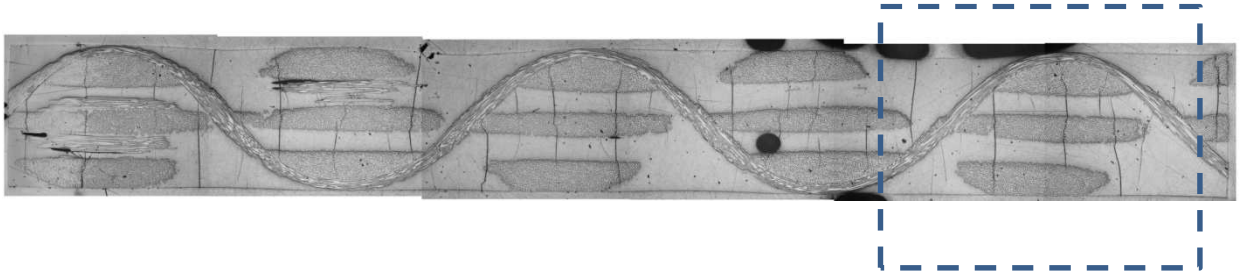

Figure 5.22

It has to be noticed again the presence of cracks running from the surface to the inside of the specimen along the through thickness direction. These cracks go across the weft tows and the matrix pocket; for every unit cell, there are 3 to 4 cracks, roughly evenly distributed along the length of the unit cell. A magnification of the blue dashed rectangular area is shown in Figure 5.23. The distribution of damage is very similar to thatfound in Specimen A and described earlier.

One additional observation worth noting in figure 5.23 is the development of "microdelaminations". These occur when a matrix crack, located away from the z-crown, intersects the internal surface of the z-tow. These microdelaminations are discussed in more detail below.

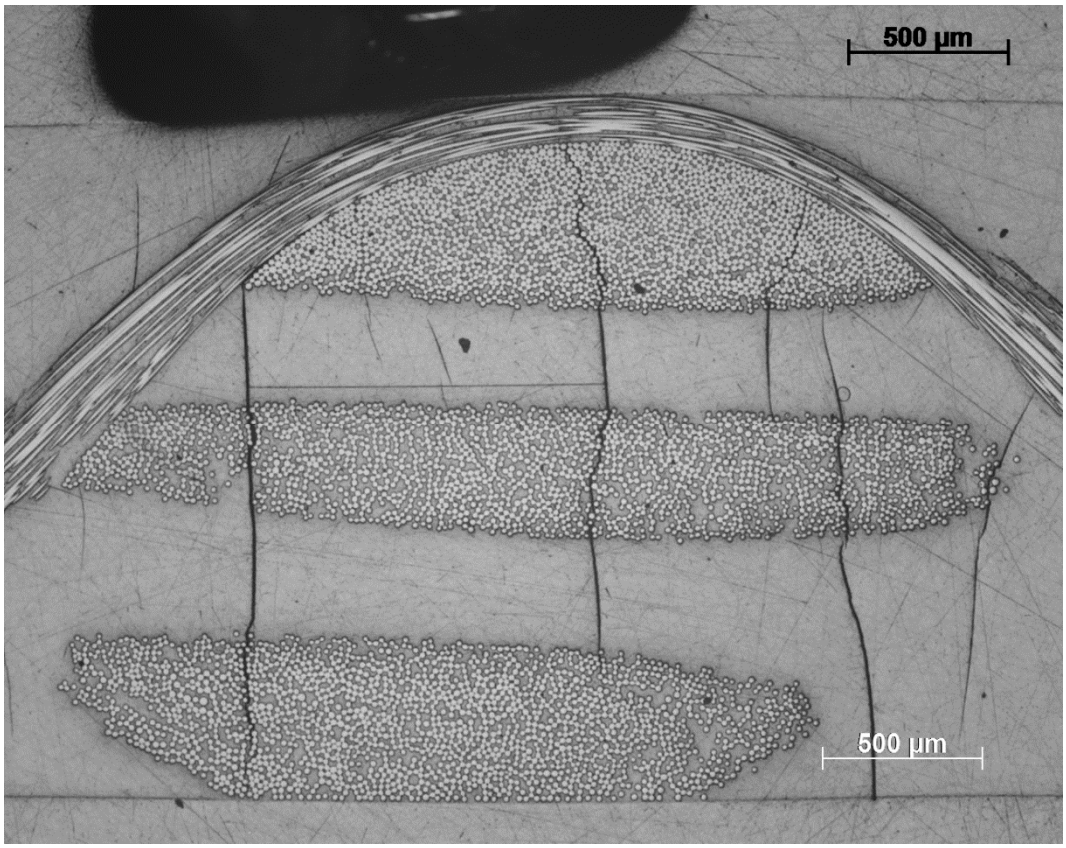

Figure 5.23 Matrix cracks inside the resin pocket

Figure 5.24 shows the weft matrix cracks in the plane of the z-tow (in the resin pocket) and just behind this plane, and the corresponding fiber fractures in the warp tow close to the z-crown, as seen previously for specimen A .

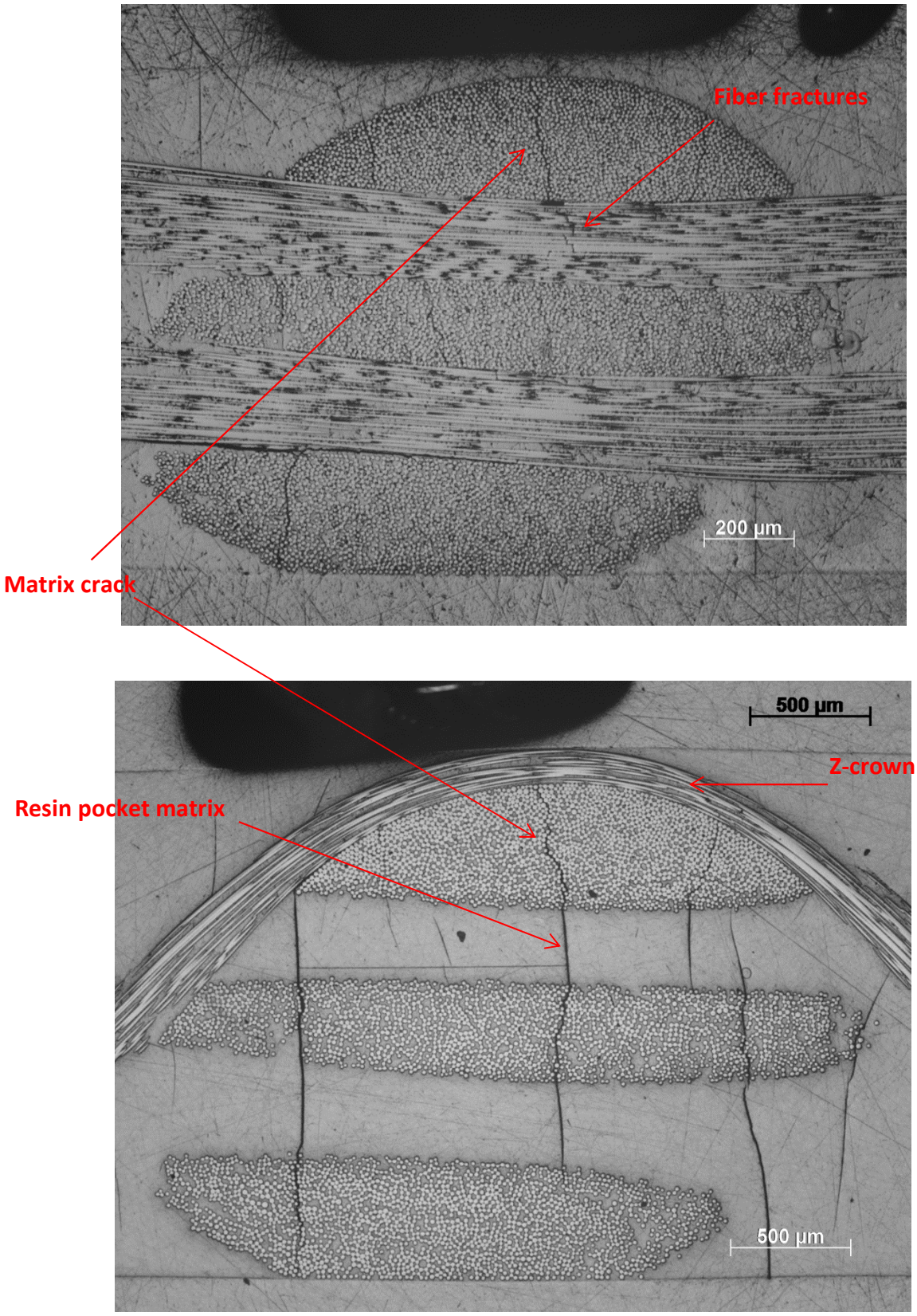
Fiber fractures
200 µm
Matrix crack
500 µm
Z-crown
Resin pocket matrix
500 µm

Figure 5.24

5.4. Observations on Microdelaminations

In the section above, it has been observed the presence of “microdelaminations” was indicated. In the section above, it has been observed the presence of “microdelaminations”. Microdelaminations, i.e. small delaminations, occurred when a matrix crack ran across the resin pocket and met the z-tow at an angle. This phenomenon is typical of this particular class 3D woven composite. Figures 5.25 (a) to (c) show microdelaminations developed in specimens A and B. These microdelaminations can be disctinguished from the extensive delaminations described in the next section.

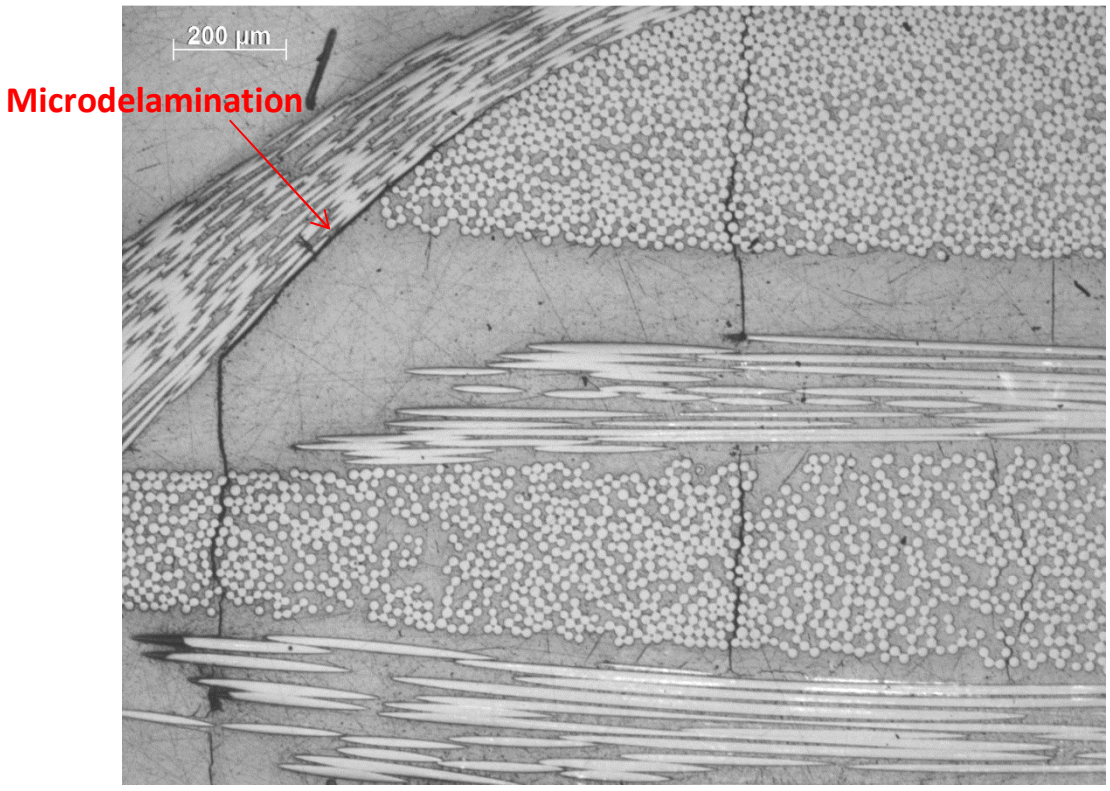

Figure 5.25 (a)

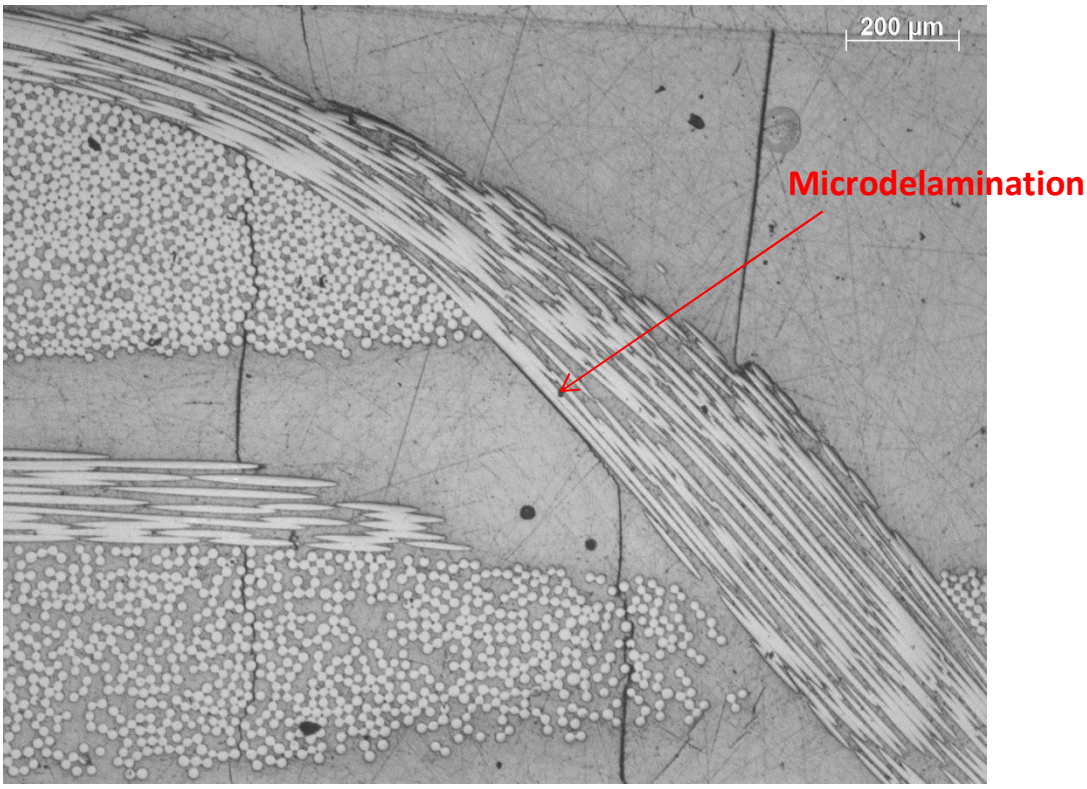

Figure 5.25 (b)

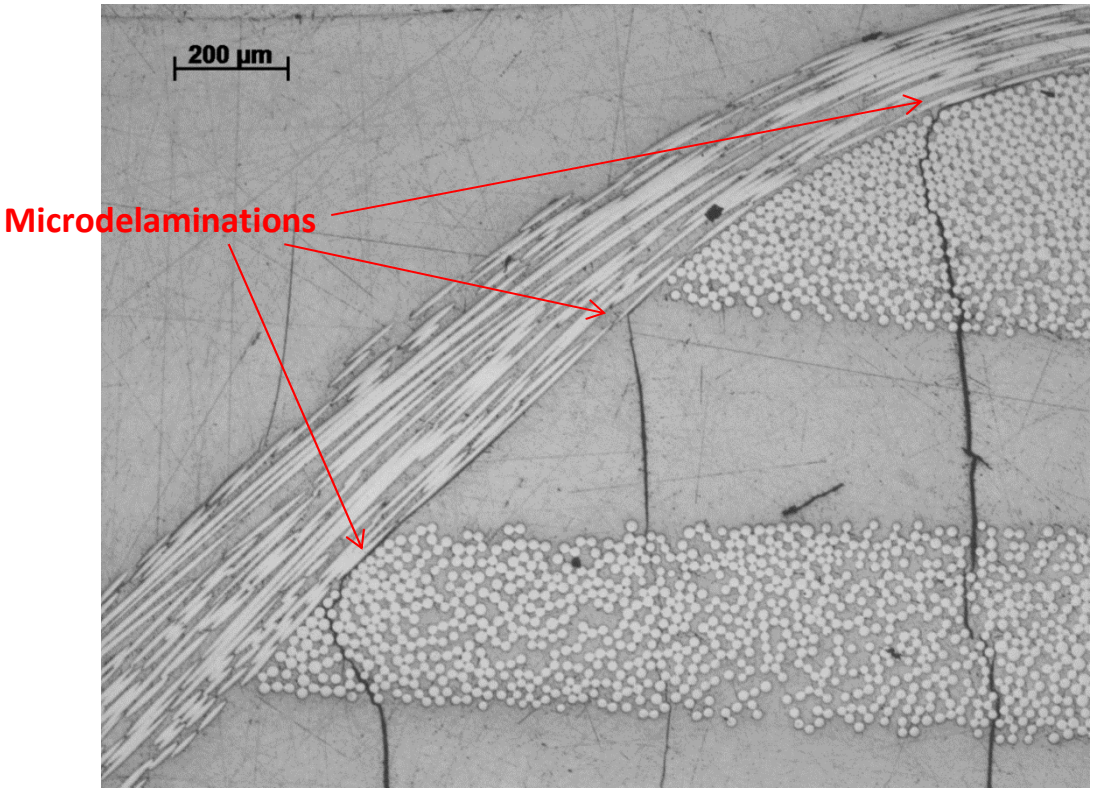

Figure 5.25 (c)

5.5. Observations on extensive delaminations

Delamination, considered as the separation of two interfaces, occurred not just on a microscopic scale but also on an extensive scale. Figure 5.26 shows some observations on a specime that was taken to fatigue failure, although these observations were taken 50 mm away from the fracture surfaces. . Close observation of sections on the "XY" showed extensive delamination developing on the interface between warp and weft tows. Figure 5.26(a) shows just over two unit cells of the specimen, while Figure 5.26(b) shows one unit cell.

5.26(a)

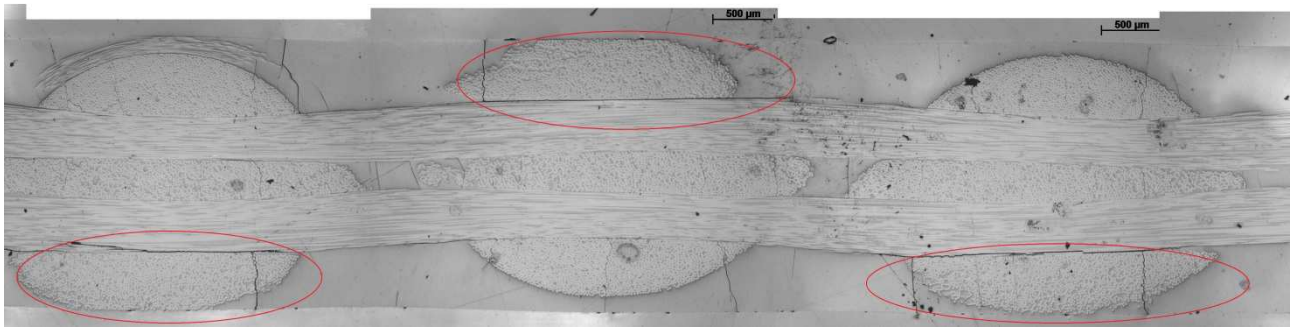

5.26(b)

Figure 5.26. Extensive delaminations at the interface between the outer weft and tow and the adjacent warp tow at locations opposite to the z-crowns. (a) Two unit cells shown. (b) One unit cell shown.

Figure 5.26 suggests that each delamination was associated with a matrix crack which extended to the surface of the specimen. The matrix crack extends across the surface weft tow, before reaching the interface between weft and warp tow and becoming a delamination which extends across the interface between the surface weft tow and the adjacent warp tow.

An important aspect of this phenomenon is the position of these delamination cracks in relationship with the architecture of the fabric. As can be seen from Figure 5.26, this type of delamination occurred at the interface between the outer weft tow and adjacent warp tow which is at the opposite side of the specimen to the z-crown. This interface suffers from extensive delamination at this location. Figure 5.27 shows the interrelationship between this damage in more detail.

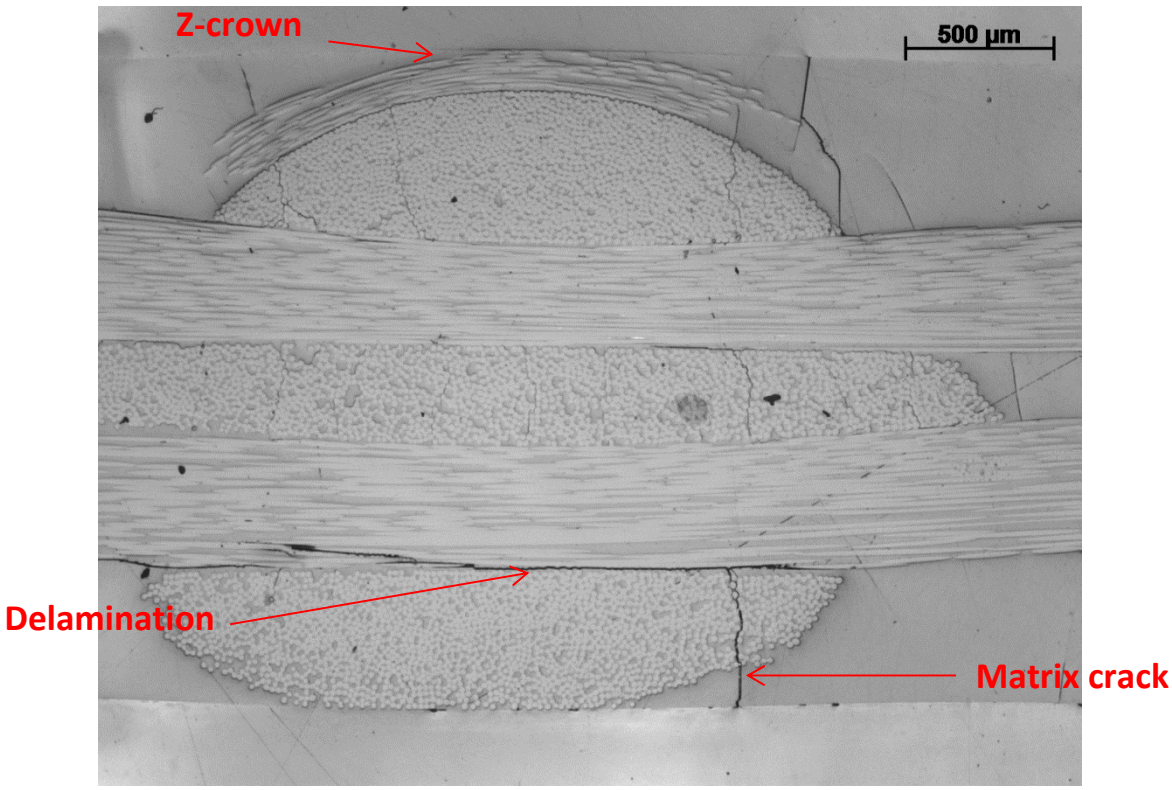

Figure 5.27 Detail of matrix crack and associated delamination

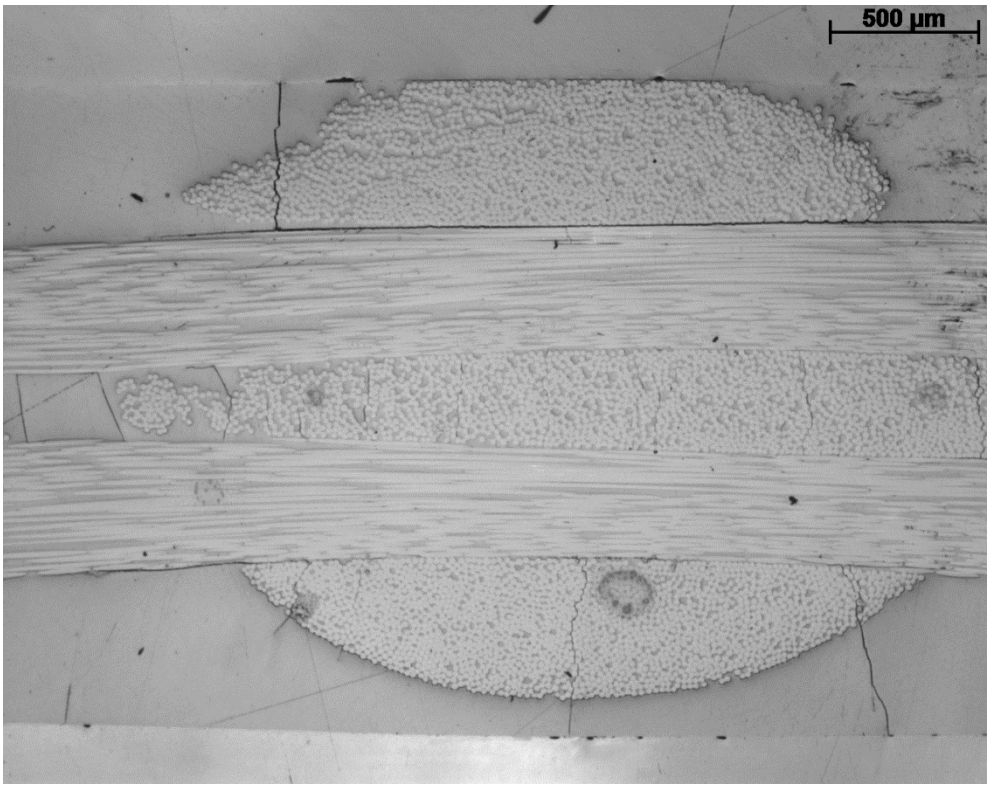
500 µm

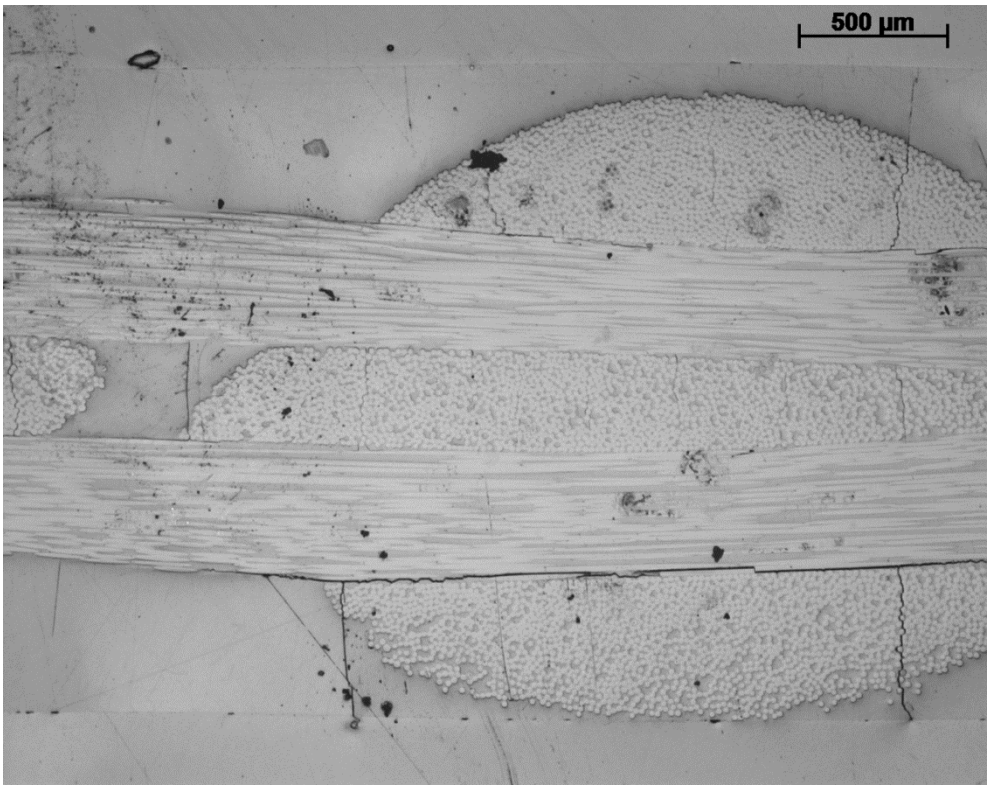
500 µm

5.6 Concluding remarks

In this chapter the evidence of damage have been discussed. The combination of the optical microscopy has been connected to the result obtained with the micro-computed tomography. In general microscopy observation indicates that fiber fractures developed in the warp tow closest to the z-tow. Fiber fractures appear to be associated with matrix cracks in the weft tow. Furthermore, fiber fractures in the warp tow also appear to be located toward the resin pocket between the warp tows caused by the location of the z-tows. There are evidence that the matrix crack in the resin pocket also contributes to the fiber fractures.

In addition to fiber fractures, delamination has been observed in two different aspects: extensive delaminations were observed between the weft tows and the warp tows located on the opposite side of the z-crown. No fractures were observed adjacent to this location.

"Microdelaminations" were observed on the interface between the either the matrix and the z-tow or the z-tow and tow.

Finally, no z-tow fractures were observed.

6. Discussion and Conclusions

6.1 Introduction

In this chapter the mechanical test results and damage observations will be discussed, before some conclusions are drawn from the work as a whole

6.2 Relationship between damage observations and stiffness/hysteresis loop changes

In chapter 3 the stiffness reduction and the hysteresis loop changes was shown. After the investigation achieved with the optical microscope and the micro-CT technique it's possible to suggest a damage development mechanism for this 3D composite material for a relatively low stress level (peak stress of 150 MPa) and fatigue lifetimes of 50,000 to 100,000 cycles.. The trend of the area within the hysteresis loop with the number of cycles can be divided into three main parts: the first part is up to about cycle 10000 where the hysteresis loops reaches a constant value. In this first stage it possible that the damage occurring inside the material is composed of cracks developing at 90° to the loading direction inside the matrix and the weft tows, extensive delamination and microdelamination. The area within the hysteresis loop reached a peak in the first 100 to 500 cycles where probably matrix cracks are spreading in the orthogonal direction to the loading direction. After that peak, there's a decreasing trend until 10000 cycle where a plateau of constant values is about to begin. Inside this decreasing stage, it is possible that

the matrix cracks density reached the saturation, although further work would be required to prove this.

The second stage is characterized by a plateau where the area within the hysteresis loop is constant or slightly increasing with the number of cycles. In this stage it's possible to assume that the damage is no more caused by the creation of new matrix cracks, but is due to the development of delaminations (extensive and microdelamination) and the growth of existing matrix cracks. It is possible that fiber fractures are also occurring and growing in number. Again, it must be said that there is no evidence within this work to support these suggestions. In this stage there is not a sensitive change on the value of the Young's modulus because the stiffness reduction is not substantially affected by delaminations or by low densities of fiber fractures. . It has to be remembered that the hysteresis loop investigation was performed with an extensometer which covered the entire gauge length of the specimen, so it is possible to assume that in the second stage fiber are starting to fracture, but the fractures are distributed all over the length of the specimen. It is also possible to assume that delamination cracks are growing in this stage – though the extent is not known.

In the third stage and the very final stage, the main damage is attributed to fiber fractures that are not distributed but are concentrated in localized positions within the warp tows. So in the third stage the damage is no more distributed inside all the length of the specimen and the damage is concentrated in one, or maybe more, locations that will bring the material to the final and catastrophic failure. In the third stage, the increasing size of the hysteresis loops may be due to frictional losses at interfaces where extensive

delamination has occurred. The final stage is probably due to the propagation of a tow fracture that leads locally to extensive fracture, stiffness reduction and rapidly increasing frictional losses. However, insufficient evidence is available to support this hypothesis of the development of failure at present.

6.3 Speculation on the location of the warp tow fiber fractures

The particular location of the fiber fractures in both specimens analyzed conduced to several speculation about the combination of mechanisms that crated that kind of damage. Considering the position of the fiber fractures in the warp tow that is just below the top of the z-crown, it is possible to take in consideration the hypothesis of a "Microbending" mechanism. The effect of a load applied in the X-direction leads to the z – tow to align its sinusoidal profile with the loading direction. This z-tow loops over a weft tow, so when the z-tow is loaded it compress locally the weft tow. The compression carried by the weft tow is transferred to the tow warp tows running under the weft tow causing a local bending of the warp tows. This could explain the presence of the fractures in the same plane for both warp tows, and this plane could correspond to the plane where the bending stress is at its maximum since the fractures are just below the top of the z-crown. This "microbending" in combination with normal stress on the warp tow,the stress concentration caused by the matrix crack in the weft tow and all matrix crack developing inside the resin pocket (saw in this chapter), could cause the final catastrophic failure.

6.4 Conclusions.

In this project the evidence of damage have been discussed. The combination of different damage aspects reflect the complexity of the fabric architecture. The combination of the optical microscopy with the micro-computed tomography gave a better understanding of the damage development in fatigue loading and also gave the opportunity to produce hypothesis about the cause that brought fiber fractures to be located in that particular position: in general microscopy observation indicates that fiber fractures developed in the warp tow closest to the z-tow. Fiber fractures appear to be associated with matrix cracks in the weft tow. Furthermore, fiber fractures in the warp tow also appear to be located toward the resin pocket between the warp tows caused by the location of the z-tows. There are evidence that the matrix crack in the resin pocket also contributes to the fiber fractures. It has to be noticed that no z-tow fractures were observed.

In addition to fiber fractures, delamination has been observed in two different aspects: extensive delaminations were observed between the weft tows and the warp tows located on the opposite side of the z-crown. No fractures were observed adjacent to this location.

"Microdelaminations" were observed on the interface between the either the matrix and

7. Suggestions for future work.

In this dissertation only the late stage in fatigue damage development has been observed. Future work could be involved in the analysis of the very early stages of the damage development, in order to understand the nature of the matrix cracks in the resin pocket and their role in the initiation of the fiber fractures. Also, an FEM model could help to explain the stresses that are creating inside the material when it is loaded into tension. Furthermore, it has to be remembered that during this project the material was loaded only in warp direction so another possible work could be loading the same material in the weft direction.

References

[1] C. Long (2005), "*Design and Manufacture of Textile Composites*", Woodhead Publishing, Cambridge, UK

[2] T.- W. Chou and F. K. Ko (1989), "*Textile structural composites*", Elsevier science, Oxford, UK

[3] D. Hull (1981), "*An introduction to composite materials*", Cambridge University Press, Cambridge, UK.

[4] W. Hufenbach, M. Gude and C. Ebert (2009), "*Hybrid 3D-textile reinforced composites with tailored property profiles for crash and impact applications*", Composites Science and Technology, Vol. 69 **(9)**, pp. 1422-1426

[5] L. J. Broutman (1967), "*Modern composite materials*", Addison-Wesley Pub. Co, Reading, UK

[6] S. W. Case, K. L. Reifsnider, (2007), "*Fatigue of Composite Materials*", Comprehensive Structural Integrity, Chapter 4.16, pp. 405-441

[7] W. D. Calister, (2007), "*Materials science and engineering an introduction* (7th ed.)", John Wiley & Sons, Inc. US

[8] N. P. Cheremisinoff (1995), "*Fiberglass reinforced plastics*", Noyes Publications, Park Ridge, N.J., U.S.A

[9] A.E Bogdanovich and M.H. Mohamed (2009), "*Three-Dimensional Reinforcements for composites*", SAMPE journal, Vol. 45 **(6)**, pp. 1-20

[10] A P. Mouritz, M. K. Bannister, P. J. Falzon and K. H. Leong (1999), "*Review of applications for advanced three-dimensional fibre textile composites*", Composites Part A: Applied Science and Manufacturing, Vol. 30 **(12)**, pp. 1445-1461
115

[11] S. Chou, H. - C. Chen, H.- E. Chen, (1992), "*Effect of weave structure on mechanical fracture behavior of three-dimensional carbon fiber fabric reinforced epoxy resin*", Composites Science and Technology, Volume 45 **(1)**, pp. 23-35

[12] Y. Gowayed, J. Wu, L. Barowski and W. Westphall (1996), "*Mapping of preform architecture for textile reinforced composite products"*, Composites Part A: Applied Science and Manufacturing, Vol. 27 **(11)**, pp. 1023-1032

[13] A.P. Mouritz (2007), "*Review of z-pinned composite laminates Review Article*", Composites Part A: Applied Science and Manufacturing, Vol. 38 (12), pp. 2383-2397

[14] H. Huang and A. M. Waas (2009), "*Compressive response of Z-pinned woven glass fiber textile composite laminates: Modeling and computations*", Composites Science and Technology, Volume 69 **(14)**, pp. 2338-2344

[15] P. Tan, L. Tong, G. P. Steven and T. Ishikawa (2000), "*Behavior of 3D orthogonal woven CFRP composites. Part I. Experimental investigation*", Composites Part A: Applied Science and Manufacturing, Vol. 31 **(3)**, pp. 259-271

[16] Carvelli V, Gramellini G, Lomov SV, Bogdanovich AE, Mungalow DD and Verpoest I (2010) "Fatigue behaviour of non-crimp 3D orthogonal weave and multi-layer plain weave E-glass reinforced composites." Composites Science and Technology, vol 70, p2068;

[17] Lomov SV, Bogdanovich AE, Ivanov DS, Mungalov D, Karahan M and Verpoest I (2009) "A comparative study of tensile properties of non-crimp 3D orthogonal weave and multi-layer plain weave E-glass composites. Part 1: Materials, methods and principle results." Composites: Part A, vol 40, pp1134.

[18] Mouritz AP (2008) "Tensile fatigue of properties of 3D composites with through-thickness reinforcement." Composites Science and Technology, vol 68, p2503.

Appendix A. Macro for hysteresis Loop

```
Sub Macro1()
'
' Macro1 Macro
' Macro recorded 09/07/2013 by Tobias Capell
'
' Keyboard Shortcut: Ctrl+Shift+R
'
Dim counter As Long
Dim strain1 As Single
Dim strain2 As Single
Dim load1 As Single
Dim load2 As Single
Dim arealower As Single
Dim areaupper As Single
Dim cycle As Long
Dim cyclea As Long
Dim energy As Single
Dim counter1 As Integer
Dim width As Single
Dim height As Single
Dim area As Single



counter = 2
counter1 = 2
cycle = Cells(2, 6)
Cells(1, 12) = "Cycle"
```

```
Cells(1, 13) = "Energy lost"

Do Until cycle = 0

   areaupper = 0
   arealower = 0

   Do Until cyclea > cycle



   cyclea = Cells(counter, 6)
   strain1 = Cells(counter, 9)
   strain2 = Cells((counter + 1), 9)
   load1 = Cells(counter, 8)
   load2 = Cells((counter + 1), 8)

   If strain2 < strain1 Then

width = strain1 - strain2
height = (load1 + load2) / 2
area = width * height

arealower = arealower + area

   Else
    width = strain2 - strain1
height = (load1 + load2) / 2
area = width * height
```

```
areaupper = areaupper + area
  End If

 counter = counter + 1

  Loop

 energy = areaupper - arealower

Cells(counter1, 12) = cycle
Cells(counter1, 13) = energy

counter1 = counter1 + 1

cycle = Cells(counter, 6)

Loop

End Sub
```